Gigayear stability of cratonic edges controls global distribution of sediment-hosted metals

Mark J. Hoggard*[,1,2], Karol Czarnota*[,3,4], Fred D. Richards[1], David L. Huston,[3]
A. Lynton Jaques,[4] & Sia Ghelichkhan[4]

1. Department of Earth and Planetary Sciences, Harvard University, 20 Oxford Street, Cambridge, MA 02138, USA.
2. Lamont-Doherty Earth Observatory, Columbia University, 61 Rte 9W, Palisades, NY 10964, USA.
3. Geoscience Australia, GPO Box 378, Canberra, ACT 2601, Australia.
4. Research School of Earth Sciences, Australian National University, Canberra, ACT 0200, Australia

*mark_hoggard@fas.harvard.edu; karol.czarnota@ga.gov.au

Sustainable development and transition to a clean-energy economy is placing ever-increasing demand on global supplies of base metals (copper, lead, zinc and nickel). This demand is outstripping the present rate of discovery of new deposits, with significant shortfalls forecast in the coming decades. Thus, to maintain growth in global living standards, dramatic improvements in exploration success rate are an essential goal of the geoscience community. Significant quantities of base metals have been deposited by moderate-temperature hydrothermal circulation within sedimentary basins over the last 2 billion years. Despite over a century of research, relationships between these deposits and geological structures remain enigmatic. Here, for the first time, we show that 85% of sediment-hosted base metals, including all giant deposits (>10 megatonnes of metal), occur within 200 km of the edges of thick lithosphere. This observation implies long-term lithospheric edge stability and a genetic link between deep Earth processes and near-surface hydrothermal mineral systems. It has been recognised that continental rifting juxtaposes necessary mineral system components including evaporites, volcanic rocks and reductants. Uniquely, extension of cratonic lithosphere enhances syn-rift sediment thickness due to increased mantle buoyancy, and reduces basal heat flow due to its greater thickness. These factors combine to double the extent of the low-temperature hydrothermal operating window, providing the optimal setting for giant sediment-hosted deposits. This discovery provides an unprecedented global framework for identifying fertile regions for targeted mineral exploration, reducing the search-space for new deposits by two-thirds on this lithospheric thickness criterion alone.

Consumption of base metals over the next ~ 25 years is set to exceed the total produced in human history to date.[1,2] Moreover, trace metals (e.g. cobalt, indium and germanium) are often produced as by-products of base metal mining and are essential in many high-tech applications.[3] A growing concern is that the rate of exploitation of existing reserves is outstripping discovery of new deposits, despite exploration expenditure tripling during the 2005–2012 minerals boom.[1,2] To reverse this trend and supply the resources necessary to comply with policies such as the Paris Climate Agreement and United Nations' Sustainable Development Goals, improved techniques for locating new deposits are required, particularly those buried under shallow sedimentary cover or ice.

Narrowing the search-space for new deposits

In mineral exploration, initial area selection at continental scales is arguably the most important step, as successful identification of fertile regions can compensate for many subsequent errors.[4] Over the last two decades, the search for analogues of known deposits has progressed towards a more holistic determination of factors controlling deposit generation and preservation.[5,6,7,8,9] Mineral systems analysis has resulted in a growing acceptance that the spatial distribution of deposits associated with magmatic processes is controlled by lithospheric-scale structure.[4,10,11] For example, porphyry copper deposits are generated by wet melting in the mantle wedge above a subducting slab, emplacement of these melts into the shallow overlying crust, and subsequent concentration by high-temperature hydrothermal circulation.[11] Thus, by combining the plate tectonic setting with geological constraints on the location of key mineral system ingredients, the search-space for new magmatic deposits can be substantially reduced.[12,13,14]

In the case of sediment-hosted deposits, most assessments to date have focused on their genesis within the context of Earth's secular evolution, as well as past tectonic and geographic settings.[15] The majority are found in failed rift and passive margin settings, and it is generally agreed that basin-scale hydrothermal circulation is required to scavenge sufficient metals to form giant deposits (Figure 1a).[16,17,18] Metals are mobilised and transported by oxidised brines with moderate temperatures (80–250°C) and moderate-to-high salinity (10–30 wt.% NaCl), limiting their maximum age to the Great Oxidation Event at 2.4 Ga.[16,17] These fluids are sourced from evaporites at low latitudes and remain buffered as they pass through voluminous oxidised terrestrial sediments, allowing them to scavenge lead from arkosic sandstones and felsic volcanics, as well as copper and zinc from mafic rocks.[16,17] Transport along faults focuses these fluids into oxidation-reduction interfaces, such as distal-facies black shales, where metals precipitate (Figures 1b and 1c).[19]

Narrowing the search-space for new sediment-hosted deposits has been less successful than for magmatic mineral systems. Sedimentary basins cover $\sim 75\%$ of the continental surface, and the key ingredients of evaporites associated with brine formation, felsic and mafic volcanic rocks for sourcing metals, and organic rich shale precipitation sites, are widespread and do not substantially reduce this search-space. The first-order geological control that localises their spatial distribution throughout the continents remains unknown, severely limiting predictive power for identifying new targets. A classic example comes from the Carpentaria Zinc Belt in northern Australia, which contains several world class PbZn-CD deposits formed between 1.8–1.4 Ga (Figure 2a). These deposits lie along an arcuate trend that runs oblique to mapped geology and crustal geological boundaries, as demonstrated by gravity and magnetic datasets.[20]

Crucially, despite the absence of a clear crustal relationship, the linear distribution of sediment-hosted deposits in the Carpentaria Zinc Belt hints at an underlying regional-scale control. A significant advance in understanding the genesis of magmatic mineral systems has come from probing their relationship with major crustal and lithospheric structures.[11] Given that sedimentary basins are themselves the result of lithospheric scale processes, we therefore investigate both regional and global-scale links between sediment-hosted base-metal deposits and the most fundamental shallow mantle structure – the lithosphere-asthenosphere boundary (LAB).

Relationship with lithospheric structure

We begin by collating global inventories of six major base-metal mineral systems from published sources (Methods). Three are magmatic and three are sediment-hosted, which include sedimentary copper (Cu-sed), clastic-dominated lead-zinc (PbZn-CD, commonly also referred to as sedimentary exhalative), and Mississippi Valley-type lead-zinc (Pb-Zn-MVT). We next refine a method developed by Priestley and McKenzie (2013)[21] for mapping the thermal LAB from seismic tomography, taking into consideration recent laboratory experiments[22] concerning the effect of anelasticity on shear-wave velocities (Methods). This benchmarking procedure is necessary in order to increase consistency between LAB maps obtained for different tomography models, which can image surprisingly variable seismic velocities. A high resolution regional LAB map over Australia is obtained from the FR12 model[23] and is calibrated using nine local paleogeotherms derived from thermobarometry of mantle peridotite xenoliths and xenocrysts. To expand our analysis to other continents, a global LAB is also produced using the SL2013sv model[24] and calibrated using multiple constraints, including the latest thermal structure of cooling oceanic lithosphere.[25] This global LAB exhibits a bi-modal thickness distribution, with peaks at 80 km and 190 km, separated by a minimum at 150 km (Supplementary Information).

Inspection of the Australian model reveals a striking correlation between major sediment-hosted mineral deposits and the edge of thick lithosphere, defined here by the 170 km thickness contour (Figure 2b). Major PbZn-CD and sedimentary copper deposits in the Carpentaria Zinc Belt overlie this contour, which runs obliquely to geological boundaries, such that intersections between these two features consistently coincide with deposit locations. This behaviour is particularly useful for highlighting new prospective regions for exploration. Other observables that correlate with this lithospheric thickness change include variations in lead isotopes from Proterozoic galena and pyrite minerals,[26] long-wavelength gravity anomaly gradients,[27] a topographic ridge, and the western extent of Cretaceous marine sediments (Figure 2a). These latter two associations demonstrate the post-Proterozoic stability of this edge and its influence on local geology and topography. There is also a strong relationship with iron-oxide-copper-gold deposits, including the Olympic Dam mine in South Australia (84 Mt of copper, largest known uranium resource).[28,29,30] However, a lack of consensus over global classification schemes means that we have limited analysis of this deposit type to Australia.

Extending our analysis globally further confirms the strength of this relationship (Figure 2c). The link between the 170 km lithospheric thickness contour and location of all large sediment-hosted deposits holds regardless of deposit age, which spans at least the last 2 billion years. Given the 180–220 km cluster of LAB thicknesses is likely to represent standard cratonic lithosphere, the 170 km contour demarks the outer boundaries, where the lithosphere begins to thin. Within the PbZn-CD deposit class, those more strongly associated with abundant mafic rocks systematically occur on the thinner lithosphere side of the contour compared to their carbonate-rich counterparts (e.g. Carpenteria Zinc Belt and northwest North America). These observations are consistent with an extensional origin of the host basins. Surprisingly, given results of previous studies,[11] deposits associated with magmatic systems generally do not seem to follow this simple pattern (Supplementary Information).

To quantify these visual relationships, the shortest distance is calculated between each deposit and the 170 km LAB thickness contour and results are plotted in a cumulative distribution function (CDF). Weighting deposits by the mass of contained metal and substituting the Australian LAB from the global model with our regionally enhanced version substantially improves the correlation for PbZn-CD (Figure 3a). Globally, we observe that $\sim 90\%$ of sedimentary copper, $\sim 90\%$ of clastic-dominated lead-zinc and $\sim 70\%$ of Mississippi Valley-type lead-zinc resources are located within a 200 km-wide corridor either side of the 170 km LAB thickness contour (Figure 3b). This region corresponds to only $\sim 35\%$ of continental surface area. Given that this swath width is similar to the ~ 280 km node spacing in SL2013sv, tighter constraints are only possible with higher resolution tomography models. The significance of this result is examined using the *two-sample Kolmogorov-Smirnov test*[31] which estimates that the probability of these sediment-hosted deposits representing random continental locations is less than 1 in 10^{12} (Methods).

All > 10 mega-tonne sediment-hosted deposits are located along this boundary, but amongst the smaller deposits, there are some notable exceptions. Minor PbZn-CD outliers occur in Europe, the Caribbean, Indonesia and east China. Anomalous PbZn-MVT deposits are found in Ireland, east China and along the Tethys subduction zone across Europe, whilst small sedimentary copper deposits occur in southwestern North America and southern South America. This observation indicates that minor sediment-hosted mineral systems can develop in a variety of extensional basins, whilst giant deposits form only at the edges of cratonic lithosphere. However, not all outliers were necessarily anomalies at the time of ore formation. The majority now occur in accretionary terranes, whereby plate tectonic processes may have rifted segments off thick lithosphere and transported them into subduction zone settings. Other areas, such as east China, are known to have undergone lithospheric thinning some time after deposit formation, based on thermobarometric constraints.[32]

Regardless of age, sediment-hosted base-metal deposits predominantly cluster on the edges of present-day thick lithosphere. Therefore, many of these lithospheric steps appear to be remarkably robust on billion-year timescales, despite the assembly and disaggregation of several supercontinents, impacts of large igneous provinces and the possible erosional effect of edge-driven convection.[33] Deposits in northwestern North America span ages ~ 1.5–0.5 Ga, pointing to the stability and importance of this boundary in localising multiple deformation and ore-forming processes.

Mineral System Implications

Our results indicate that the edges of thick lithosphere place first-order controls on the genesis of extensional basins and their associated mineral systems (Figure 1). Rifting causes localised thinning and produces a lateral transition from oxidising terrestrial environments into marine settings that provides the optimal juxtaposition of the ingredients necessary for deposit formation. The adjacent unstretched cratons provide a bountiful source of oxidised sediments and extensive low-elevation platforms, which enhances evaporite formation. Proximal land masses also provide restricted marine settings that promote euxinic water conditions and are favourable for deposition of reducing shales high in organic carbon. Thinning of the lithosphere in the centre of the basin causes decompression melting, providing mafic and felsic volcanic rocks from which metals are scavenged. Intercalation of proximal and distal facies components is further modulated by transient vertical motions, generally thought to be associated with edge driven convection across lithospheric steps.[34] Nevertheless, these mineral system components are common to both rifts in thick lithosphere and regular passive margins, and the question remains — what is favourable about rifting cratonic lithosphere for formation of the shallow hydrothermal systems necessary to produce giant deposits?

From a geodynamic perspective, these lithospheric edges represent rheological contrasts that focus strain and localise repeated cycles of extensional deformation and basin contraction, thereby controlling both the spatial distribution of required lithologies and the focusing of mineralising fluids.[35,36,14] Thick cratonic lithosphere is colder than standard continental lithosphere and has a larger seismogenic thickness, resulting in the development of deeper, longer, more widely spaced normal faults during rifting.[37] This architecture increases the horizontal aspect ratio of hydrothermal cells, providing greater volumes for fluid–rock interaction. These faults are active for longer periods of time, and the entire syn-rift phase of basin formation can last 50–100 Myr, in contrast to standard continental rifts that typically last ~ 25 Myr, yielding a more extensive time window for mineralisation.[38]

A key observation is that metal precipitation in sediment-hosted base metal deposits is generally driven by oxidation-reduction reactions, which become ineffective when brine temperatures exceed ~ 200°C (Figures 1b and 1c).[19] As hydrothermal fluid temperatures are buffered by conditions towards the base of the sediment pile (often where the mafic metal source rocks are located), this places a requirement that the basal temperature of the sedimentary pile must not significantly exceed this threshold value. Total extension in a basin can be estimated using a stretching factor, β, which is the ratio of original to final crustal thickness. Failed rifts on standard continental lithosphere such as the North Sea typically have $\beta \approx 2$, and simple thermal modelling assuming pure-shear rifting indicates that this produces 3–4 km of syn-rift sediment with basal temperatures cooler than ~ 200°C (Figure 4a; Methods). Given that all the necessary ingredients occur within basins, the likelihood of developing a successful mineral system is higher for a larger sediment pile, which can be achieved by increasing the stretching factor. However, more extreme rifting causes the asthenosphere to upwell to substantially shallower depths, producing elevated basal heat flow that heats the sediment pile above this threshold and so inhibits metal precipitation (Figure 4b).

Two important differences occur during rifting of cratonic lithosphere. First, the larger initial thickness results in a lower geothermal gradient, such that the basal heat flow spike during rifting is substantially lower than for standard continental rifts (Supplementary Information). Secondly, the density of cratonic lithosphere is reduced up to ~ 60 kg m^{-3} by chemical depletion compared to standard.[39] This increased buoyancy reduces the dampening effect during syn-rift subsidence that is associated with replacing cold continental lithosphere with lower density asthenosphere, resulting in substantially larger thicknesses of syn-rift sedimentation for any given stretching factor. When $\beta \approx 2$, 7–8 km of syn-rift sediments are deposited, the base of which stays cooler than the threshold ~ 200°C (Figure 4c). Thus, rifting cratonic lithosphere produces more than twice the volume of mineral system ingredients without exceeding the thermal conditions necessary for successful precipitation, over a duration of time that can be up to a factor of four more extensive (Figure 4d and 4e). This mechanism explains why smaller deposits can occur in any extensional setting (e.g. Irish PbZn-MVT deposits), but giant deposits requiring the largest volumes of fluid-rock interaction are restricted to rift basins at margins of the thickest lithosphere.

A final consideration is that a setting on the edge of thick lithosphere enhances the preservation potential of deposits through subsequent orogenic events and supercontinent cycles. For example, the 3 Ma Boleo Copper District in Baja California sits in shallow crust on thin lithosphere and so has poor long-term preservation potential. In contrast, the 1.7 Ga Broken Hill deposit in Australia (world's largest lead deposit) has been metamorphosed to amphibolite–granulite facies, yet survives on the edge of the Curnamona part of the South Australian Craton.

Magmatic base metal deposits exhibit a weaker association with the edge of cratonic lithosphere in comparison to the sediment-hosted systems (Supplementary Material). Porphyry copper deposits are predominantly Cenozoic in age and are generally positioned on thin lithosphere ($\leq$ 100 km). Their formation in subduction zone settings at shallow crustal depths leads to poor preservation potential within the geological record, making this association unsurprising. Volcanogenic massive sulphides have a pulsed age distribution from 3.5 Ga to present. Their generation is thought to require moderate-degree partial melting of hydrated mantle in back-arc settings.[40] We observe that they spatially occur randomly on thick and thin lithosphere, but exhibit systematic temporal ordering, with the oldest positioned over thick lithosphere rimmed by progressively younger deposits, consistent with growth of cratons by accretion. Finally, magmatic nickel deposits are mostly Archean and Proterozoic in age and commonly occur on thick lithosphere ($\geq$ 150 km). Unlike other base metal deposits, their distribution is associated with edges of even thicker lithosphere ($\sim$ 200 km), broadly consistent with previous studies showing major lithospheric structural controls on these deposit locations.[10,41,42] Their generation requires large fraction partial melting of peridotite, indicative of high mantle temperatures (more prevalent in a early, hotter Earth) and decompression melting at shallow depths.[43] Therefore, their present distribution suggests lithospheric thickness must have locally increased since formation, simultaneously enhancing preservation potential.

In summary, this work illustrates a new and robust link between giant sediment-hosted base metal mineral systems and the edges of thick lithosphere. Approximately 55% of the world's lead, 45% of its zinc and 20% of known copper is found within $\sim$ 200 km of this boundary. We have demonstrated the value of regional seismic arrays to better resolve this edge and enhance the mineral exploration efforts required to sustain ongoing global development. Significantly, deposit ages indicate that, following rifting, edges of thick-lithosphere are generally stable over billion-year timescales. The far-reaching geodynamic and societal implications of these observations highlight the need for extensive further research. To improve resolution of mapped lithospheric structure, higher fidelity seismic imaging needs to be coupled with enhanced mantle xenolith coverage and tighter constraints on seismic anelasticity from mineral physics experiments. More generally, these maps should be integrated with models of basin dynamics, surface processes and reactive transport modelling, and bench-marked against additional geological information, such as sedimentary facies variations, tectonic structures and alteration zones. These multiple research strands will yield fundamental new insights into sediment-hosted mineral systems and lead to substantial improvements in exploration success rates.

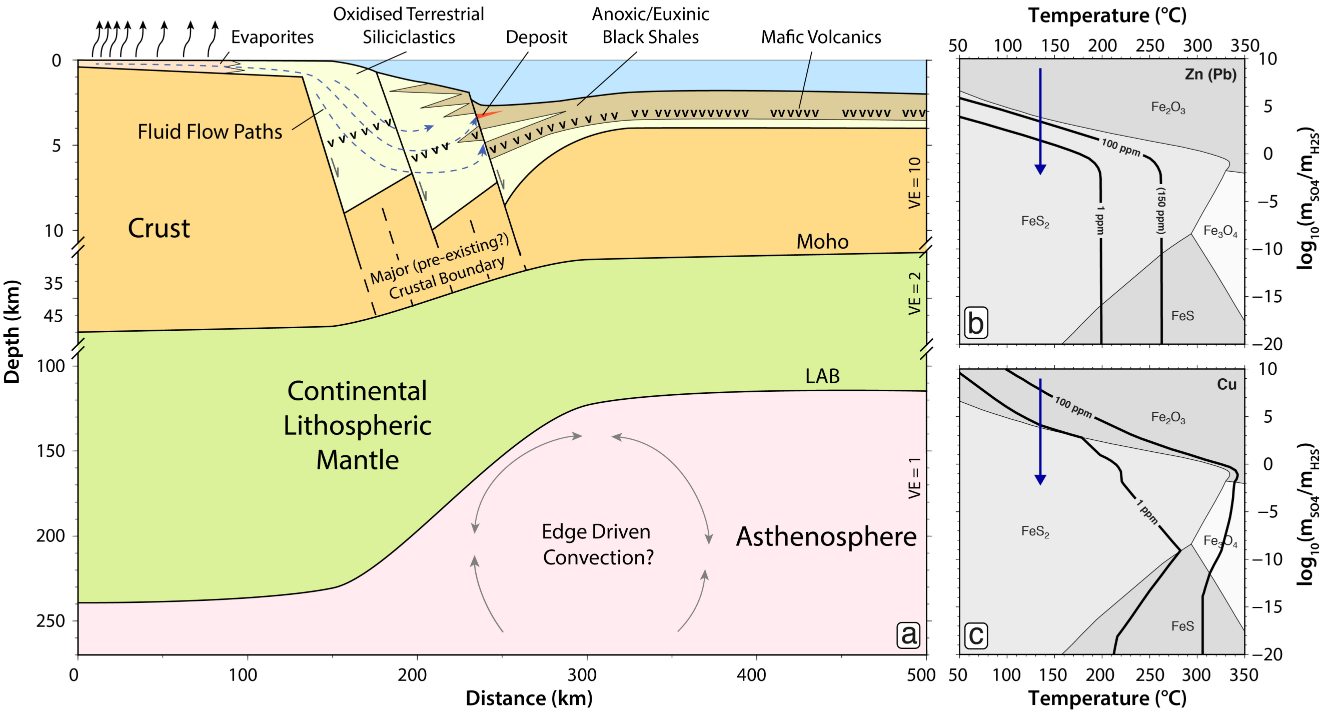

Figure 1: **Mineralisation system for genesis of sediment-hosted base metal deposits.** (a) Schematic illustration of deposit location in extensional rift settings. Basinal brines sourced from evaporites scavenge metals from oxidised terrestrial sediments and volcanics (v) on route to metal deposition sites in black shales.[18] Notice variable vertical exaggeration (VE) and prominence of the lithosphere-asthenosphere boundary edge illustrated at 1:1 scale. Schematic based on architectural constraints from the Australian Carpenteria Zinc Belt and Polish Fore-Sudetic Block. (b) Stability field of Fe–S–O minerals as a function of temperature and redox conditions; m_{SO_4} = molarity of sulphate; m_{H_2S} = molarity of sulphide; thick black lines = solubility of zinc (and lead) in brine,[19] calculated for fluid salinity = 10 wt.% NaCl, total concentration of sulphur species = $10^{2.5}$ M, and pH = 4.5; blue arrow = fluid path for metal precipitation by oxidation-reduction deposition mechanism. (c) Same for copper solubility.

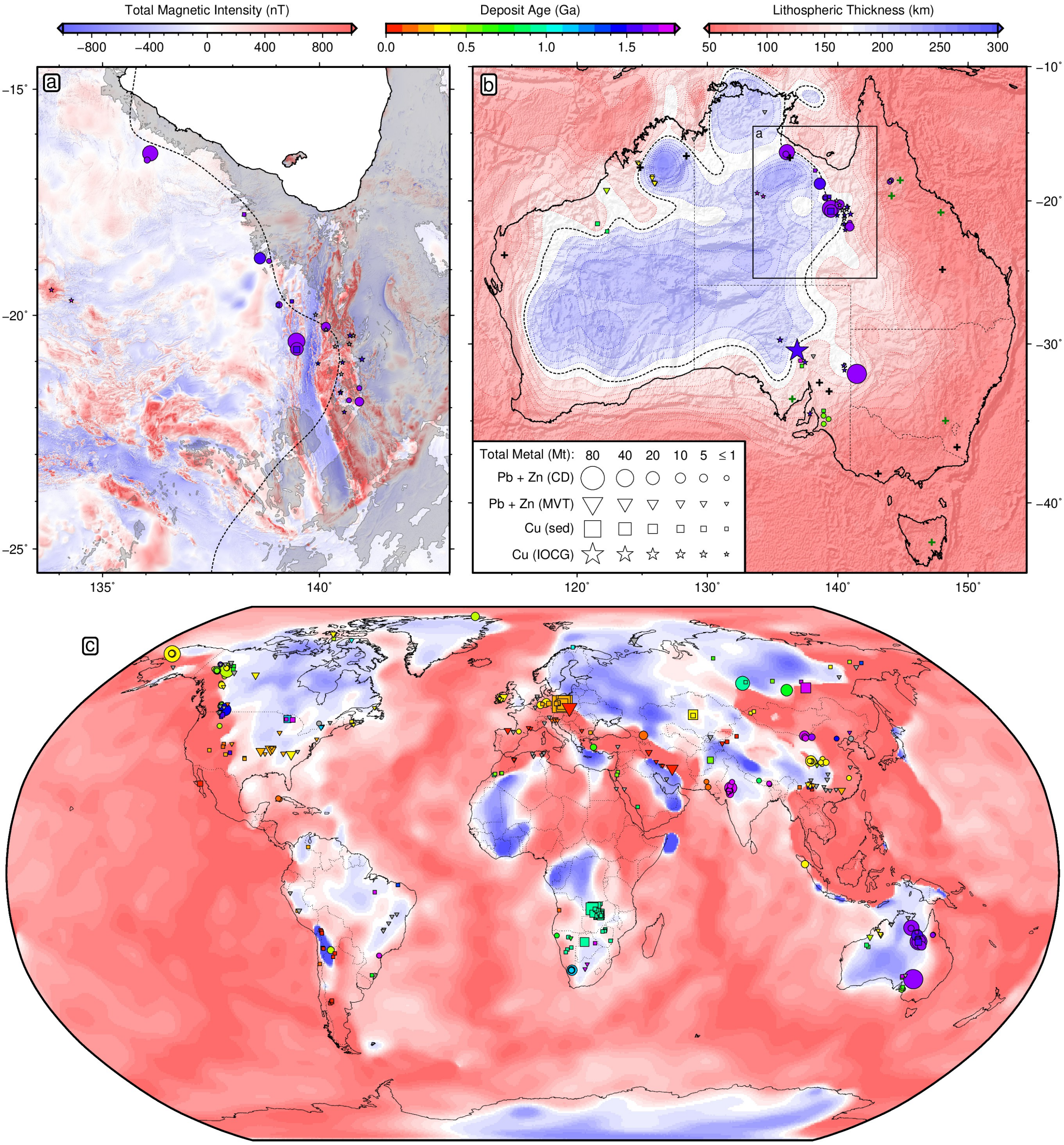

Figure 2: **Distribution of sediment-hosted and iron-oxide-copper-gold base metal deposits as a function of lithospheric thickness.** (a) Carpentaria Zinc Belt; red/blue = variably reduced to pole aeromagnetic intensity data[20]; grey polygons = generalised outcrop of Cretaceous marine sediments in Eromanga and Carpentaria Basins;[44] black dashed contour = 170 km LAB thickness; symbols = deposit locations; area proportional to estimate of total contained mass of metal (Mt = megatonnes); unknown deposit size given 2 Mt symbol; colour = ore body formation age (billion years); unknown age plotted in grey; circles = clastic-dominated lead-zinc (PbZn-CD); triangles = Mississippi Valley type lead-zinc (PbZn-MVT); squares = sedimentary copper (Cu-sed); stars = iron-oxide-copper-gold (IOCG). (b) Australian LAB mapped by converting FR12 tomography[23] to temperature using an anelasticity parameterisation[22] calibrated on local paleogeotherms (Supplementary Material) and illuminated by free-air gravity anomalies[20]; black/green crosses = geotherms used as constraints/tests in anelasticity calibration; box = location of panel (a). (c) Global LAB derived from SL2013sv tomography model[24] using a calibrated anelasticity parameterisation[22] (Methods); IOCG type not included.

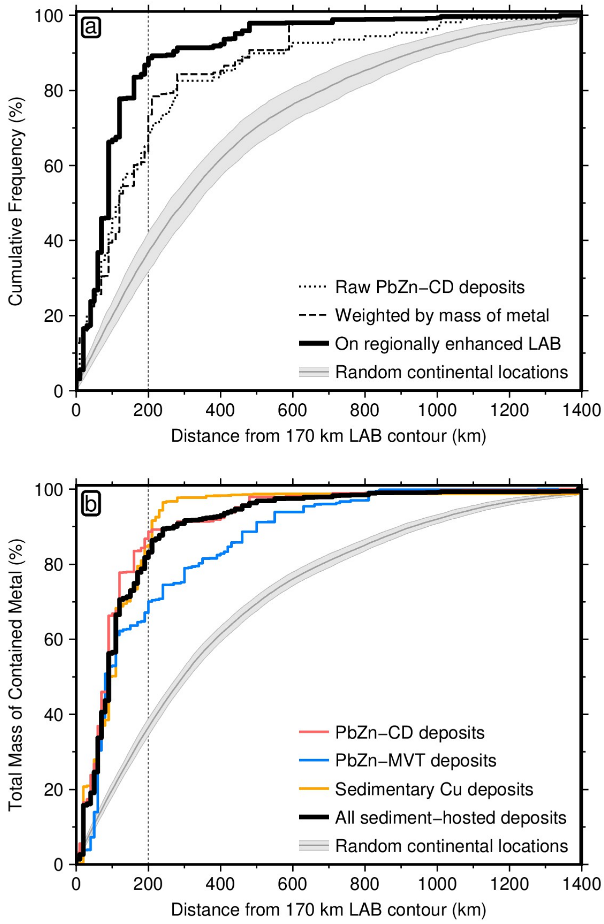

Figure 3: **Cumulative distribution functions for global sediment-hosted base metals.** (a) Different approaches for counting 109 clastic-dominated lead-zinc deposits (PbZn-CD). Dotted line = simple count of number of deposits with increasing distance from the 170 km contour in global LAB map (Figure 2c); dashed line = weighting by contained mass of lead and zinc; solid black line = mass-weighted deposits where the Australian LAB from the global model has been replaced with the regionally enhanced map (Figure 2b); grey line/bounds = mean and standard deviation of 100 sets of equivalent number (109) of randomly drawn continental locations, with respect to regionally enhanced LAB. (b) Mass-weighted, regionally enhanced CDFs for 109 PbZn-CD, 147 Mississippi Valley-type (PbZn-MVT), 139 sedimentary copper (Cu-sed) and combination of all three. Grey band as before for combined database.

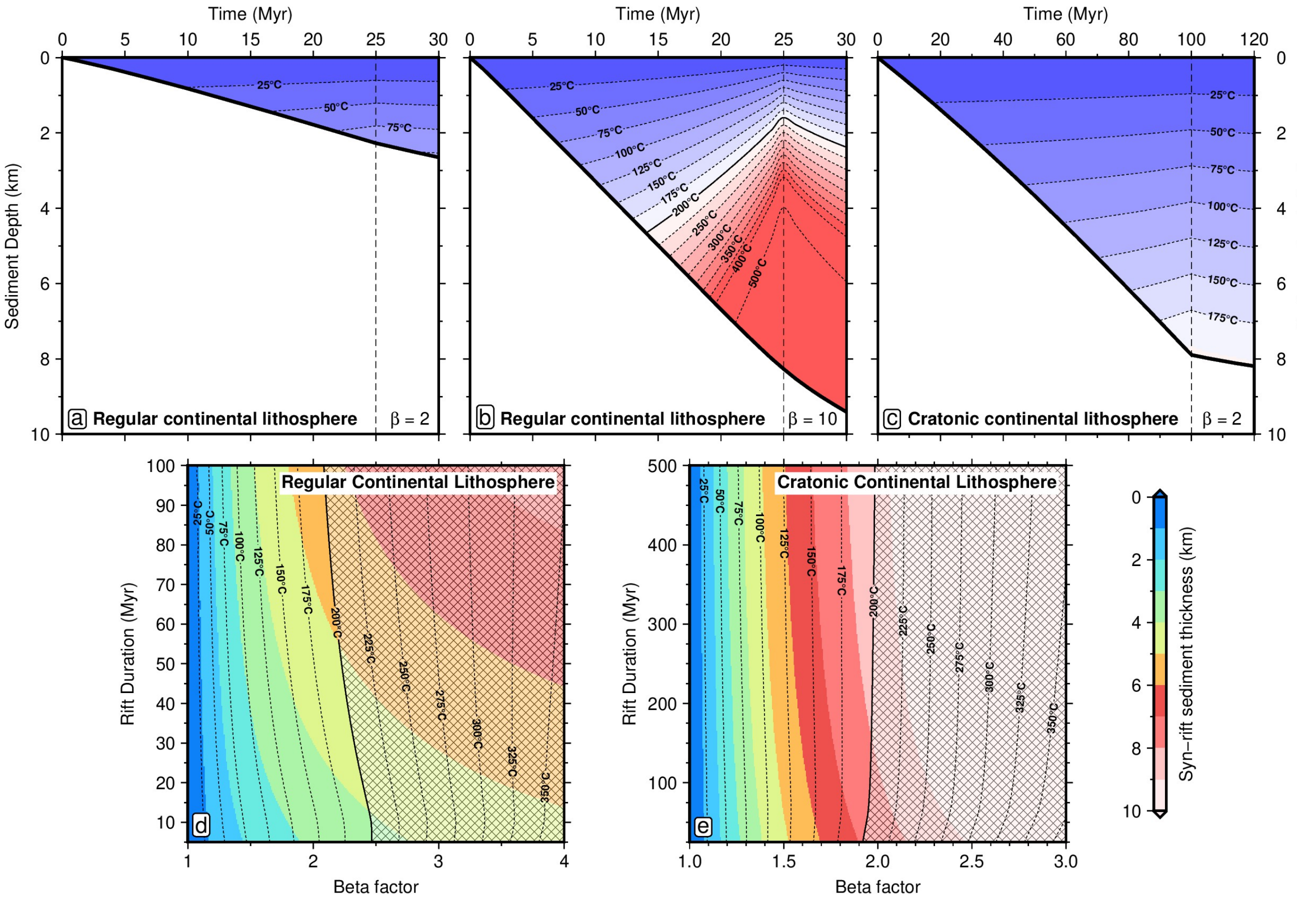

Figure 4: **Thermal modelling of basin subsidence histories.** (a) Syn-rift sedimentation for $\beta = 2$ rift of regular continental lithosphere; dashed line = rift duration; colours = temperature structure of the sediment pile. (b) Same for $\beta = 10$ rift of regular continental lithosphere. (c) Same for $\beta = 2$ rift of cratonic continental lithosphere. (d) Minerals system operating window for rifting of regular continental lithosphere; colours = syn-rift sediment thickness; contours = basal temperature of the sediment pile; hatched region = location where hydrothermal fluids become too hot for metal precipitation. (e) Same for cratonic continental lithosphere.

Methods

Deposit compilation. Our global inventory of 2141 major base metal deposits are categorised into six classes. Three are sediment hosted: sedimentary copper (Cu-sed; contains ∼20% of all known copper); clastic-dominated lead-zinc (PbZn-CD; ∼43% of all lead and ∼33% of zinc); and Mississippi Valley-type lead-zinc (PbZn-MVT; ∼25% lead, ∼22% zinc). The other three are associated with magmatic systems: copper porphyry (Cu-por; contains ∼65% of all known copper); magmatic nickel-copper-platinum group elements (Ni-Cu-PGE; ∼45% nickel, ∼3% copper); and volcanogenic massive sulfides (VMS; ∼6% copper, ∼23% lead, ∼39% zinc). For each deposit, we include the type (based on established classification schemes), location, age (direct measurement or inferred based on geological relationships) and total resource size by combining historical production with estimated resources. Our Cu-sed deposit dataset follows the classification scheme and compilation of Hitzman et al. (2005), cross-checked against Cox et al. (2007).[45,46] Where these two compilations disagree on deposit size, the larger value has been used. Our PbZn-CD and PbZn-MVT deposit compilations extensively revise and build on the work of Taylor et al. (2009).[47] References for each deposit type were manually checked and additional references have been included. We exploit the compilation of Sillitoe (2010) for Cu-por deposits.[48] Our magmatic Ni-Cu-PGE compilation follows Hoatson et al. (2006), with deposit location populated from disparate sources.[49] Our catalogue of VMS deposits is an extensive revision of the compilation by Franklin et al. (2005).[50] Australian information for all the above deposit types, with the addition of 25 iron-oxide-copper-gold deposits, was updated using the authors' own knowledge building on from the Geoscience Australia OZMin database.[51] We have endeavoured to assemble the most complete deposit dataset possible by revising and extending pre-existing compilations. Our database can be found in the online Supplementary Datasets. Importantly, patchy or absent reporting of mineral deposit information from some countries inevitably means our global database is incomplete, but we do not believe that this will impact the veracity of our main conclusions.

Choice of seismic tomography model. Our LAB maps are based on recent, high-resolution shear wave tomography models. For the global map, we use SL2013sv[24] which is an upper mantle-only model built from a combination of body and surface waves, including fundamental and higher modes. Periods considered are 11–450 s, $\sim 750,000$ seismograms are included, and misfits are calculated between synthetics and the full waveform up to the 9^{th} overtone. Crucially, simultaneous inversion for the crustal model results in reduced smearing of slow crustal velocities down into the upper mantle in comparison to other models, thereby allowing us to use more depth slices in our V_S to temperature calibration. Checkerboard resolution tests indicate that features ~ 600 km in diameter at lithospheric depths are generally well resolved. Finer features should be resolvable in regions with dense ray path coverage, such as North America, Europe and southeast Asia. The SL2013sv model contains only 6 seismometers in Australia, so has limited resolution within this continent. Therefore, we also investigate the FR12 regional seismic tomography model[23] to generate a high resolution map for the Australian continent. FR12 is a radially isotropic V_S model derived from Rayleigh wave travel times.[52] Periods considered are 50–120 s and the fundamental and first four higher modes have been used where possible, leading to good sensitivity down to ~ 250 km depths. It contains a greater number of source–receiver paths ($> 13,000$) compared to other Australian models. However, it uses an *a priori* crustal model that remains fixed throughout the inversion, resulting in noticeable smearing of crustal velocities into the upper mantle. Checkerboard tests indicate that features $\sim$ 300 km in diameter at lithospheric depths are well resolved, and where higher mode information is included, nominal vertical resolution is on the order of 25–50 km.[53] Additional seismic tomography datasets considered in the Supplementary Materials include the 3D2015-07Sv model[54] and the CAM2016 model[55,56] which have global coverage, and the Australian regional models AuSREM[57] and Y14.[58]

Parameterising shear-wave anelasticity. Seismic tomography models provide high resolution images of the upper mantle and have been extensively used to constrain its thermomechanical structure, composition, and the depth of the lithosphere-asthenosphere boundary.[59,60,61,62,63,64,65] For accurate mapping from shear-wave velocity (V_S) into temperature, it is essential to include the effect of anelasticity on this conversion.[66,67] When a viscoelastic material such as the mantle is cold, deformation associated with passage of acoustic energy is predominately elastic, yielding a linear dependence of V_S on temperature referred to as the *anharmonic velocity.* As temperature increases, a special case of viscoelastic deformation known as *anelasticity* becomes increasingly important and gives rise to a strongly non-linear relationship between V_S and temperature. This behaviour has been extensively studied in laboratory experiments on silicates and organic analogues of mantle rocks, revealing that the strength of the anelastic regime varies with both the frequency of seismic waves and as a function of material properties, such as melting temperature and grain size.[68,69,70,71,72] Several studies have attempted to parameterise these complex dependencies, and have been regularly updated as forced oscillation and creep experiments in the laboratory have been pushed towards increasingly realistic frequencies, pressures, temperatures, grain sizes and strain rates.[73,74,75] In this study, we adopt the parameterisation of Yamauchi & Takei (2016),[22] which includes effects of anelasticity in pre-melt conditions (temperatures above $\sim$ 90% of melting temperature). V_S is defined as

$$V_S = \frac{1}{\sqrt{\rho J_1}} \left(\frac{1 + \sqrt{1 + (J_2/J_1)^2}}{2} \right)^{-\frac{1}{2}} \simeq \frac{1}{\sqrt{\rho J_1}} \tag{1}$$

where ρ is the density and J_1 and J_2 represent real and imaginary components of the complex compliance, J^*, which is a quantity describing the sinusoidal strain resulting from the application of a unit sinusoidal stress. J_1 represents the strain amplitude in phase with the driving stress, whilst the J_2 component is $\frac{\pi}{2}$ out of phase, resulting in dissipation. These terms contain a high temperature background absorption band and and an additional low temperature absorption peak, expressed as

$$J_1(\tau'_S) = J_U \left[1 + \frac{A_B [\tau'_S]^{\alpha_B}}{\alpha_B} + \frac{\sqrt{2\pi}}{2} A_P \ \sigma_P \left\{ 1 - \mathrm{erf} \left(\frac{\ln[\tau'_P/\tau'_S]}{\sqrt{2}\sigma_P} \right) \right\} \right] \tag{2}$$

$$J_2(\tau'_S) = J_U \frac{\pi}{2} \left[A_B [\tau'_S]^{\alpha_B} + A_P \ \exp \left(-\frac{\ln^2[\tau'_P/\tau'_S]}{2\sigma_P^2} \right) \right] + J_U \tau'_S \tag{3}$$

where J_U is the unrelaxed compliance and the third term on the right of Equation (3) represents a viscous component. $A_B = 0.664$ and $\alpha_B = 0.38$ represent the amplitude and slope of the background stress relaxation, whilst A_P and σ_P represent the amplitude and width of the relaxation peak superimposed on this background trend and are given by

$$A_P(T') = \begin{cases} 0.01 & \text{for } T' < 0.91 \\ 0.01 + 0.4(T' - 0.91) & \text{for } 0.91 \leq T' < 0.96 \\ 0.03 & \text{for } 0.96 \leq T' < 1 \\ 0.03 + \beta(\phi_m) & \text{for } T' \geq 1 \end{cases} \tag{4}$$

and

$$\sigma_P(T') = \begin{cases} 4 & \text{for } T' < 0.92 \\ 4 + 37.5(T' - 0.92) & \text{for } 0.92 \leq T' < 1 \\ 7 & \text{for } T' \geq 1 \end{cases} \tag{5}$$

where $T' = \frac{T}{T_s}$ is homologous temperature, with T the temperature and T_s the solidus temperature, both in Kelvin. ϕ_m is the melt fraction and $\beta(\phi_m)$ describes the direct poroelastic effect of melt (assumed to be negligible here under upper mantle conditions). For this case, J_U is the inverse of the unrelaxed shear modulus, $\mu_U(P, T)$, such that

$$J_U(P, T)^{-1} = \mu_U(P, T) = \mu_U^0 + \frac{\partial \mu_U}{\partial T}(T - T_0) + \frac{\partial \mu_U}{\partial P}(P - P_0) \tag{6}$$

where μ_U^0 is the unrelaxed shear modulus at surface pressure-temperature conditions, the differential terms are assumed to be constant and the pressure, P, in GPa is linearly related to the depth, z, in km by $P = \frac{z}{30}$. The normalised shear wave period, τ'_S, in Equations (2) and (3) is equal to $\frac{\tau_S}{2\pi\tau_M}$, where $\tau_S = \frac{z}{1.4}$ is the Rayleigh wave period most sensitive to ambient velocity structure at that depth[76] and $\tau_M = \frac{\eta}{\mu_U}$ is the normalised Maxwell relaxation timescale. τ'_P represents the normalised shear-wave period associated with the centre of the high frequency relaxation peak, assumed to be 6×10^{-5}. The shear viscosity, η, is

$$\eta = \eta_r \left(\frac{d}{d_r}\right)^m \exp\left[\frac{E_a}{R}\left(\frac{1}{T} - \frac{1}{T_r}\right)\right] \exp\left[\frac{V_a}{R}\left(\frac{P}{T} - \frac{P_r}{T_r}\right)\right] A_\eta \tag{7}$$

where d is the grain size, m the grain size exponent (assumed to be 3 for this diffusion creep deformation mechanism), R the gas constant, E_a the activation energy and V_a the activation volume. Subscripts $[X]_r$ refer to reference values, assumed to be $d_r = 1$ mm, $P_r = 1.5$ GPa and $T_r = 1200$°C for the upper mantle. In this study, we make the simplifying assumption that $d = d_r$, which indicates an endmember scenario whereby lateral changes in V_S within the upper mantle arise purely from variations in temperature rather than grain size. It is also possible that grain size may vary significantly within the shallow mantle, but remains poorly constrained.[77,78] A_η represents the extra reduction of viscosity due to an increase in E_a near the solidus, expressed as

$$A_\eta(T') = \begin{cases} 1 & \text{for } T' < T'_\eta \\ \exp\left[-\frac{(T' - T'_\eta)}{T'(1 - T'_\eta)} \ln(\gamma)\right] & \text{for } T'_\eta \leq T' < 1 \\ \gamma^{-1} \exp(\lambda\phi) & \text{for } T' \geq 1 \end{cases} \tag{8}$$

where $T'_\eta = 0.94$ is the homologous temperature above which the effective activation energy increases beyond its original value and $\gamma = 5$ is the factor of additional viscosity reduction. $\lambda\phi$ describes the direct effect of melt on viscosity, assumed to be negligible here. The solidus temperature, T_s, is fixed to a value of 1326°C at 50 km equivalent to a dry peridotite solidus[79] and linearly increases below this depth according to

$$T_s(z) = 1599 + \frac{\partial T_s}{\partial z}(z - 50 \text{ km}) \tag{9}$$

where $\frac{\partial T_s}{\partial z}$ is the solidus gradient. We use a temperature-dependent, compressible density, $\rho(P, T)$, following the approach of Grose & Afonso (2013).[80] First, we define a linear temperature-dependence on thermal expansivity, $\alpha(T)$, such that

$$\alpha(T) = \alpha_0 + \alpha_1 T \tag{10}$$

where $\alpha_0 = 2.832 \times 10^{-5}$ °C^{-1} and $\alpha_1 = 0.758 \times 10^{-8}$ °C^{-2} are constants calibrated from mineral physics experiments.[81] To include pressure-dependence, the isothermal volume change, $(V_0/V)_T$ is calculated at each pressure using a Brent minimisation algorithm and the third-order Birch-Murnaghan equation of state

$$P = \frac{3}{2}K_0 \left[\left(\frac{V_0}{V}\right)_T^{\frac{7}{3}} - \left(\frac{V_0}{V}\right)_T^{\frac{5}{3}}\right] \left\{1 + \frac{3}{4}(K'_T - 4)\left[\left(\frac{V_0}{V}\right)_T^{\frac{2}{3}} - 1\right]\right\} \tag{11}$$

where $K_0 = 130$ GPa is the bulk modulus at zero pressure and $K'_T = 4.8$ is the pressure-derivative of the isothermal bulk modulus. The associated isothermal density change with pressure, $\rho(P)$, is given by

$$\rho(P) = \rho_0 \left(\frac{V_0}{V}\right)_T \tag{12}$$

where $\rho_0 = 3.33$ Mg m^{-3} is the density of mantle at surface pressure and temperature. The effect of pressure on thermal expansivity is included according to

$$\frac{\alpha(P,T)}{\alpha(T)} = \left(\frac{V_0}{V}\right)_T \exp\left\{(\delta_T + 1)\left[\left(\frac{V_0}{V}\right)_T^{-1} - 1\right]\right\} \tag{13}$$

where $\delta_T = 6$ is the Anderson-Grüneisen parameter. Thus, the final density, $\rho(P, T)$, can be calculated using

$$\rho(P,T) = \rho_0 \left(\frac{V_0}{V}\right)_T \left\{1 - \left[\frac{\alpha(P,T)}{\alpha(T)}\right]\left[\alpha_0(T - T_0) + \frac{\alpha_1}{2}(T^2 - T_0^2)\right]\right\} \tag{14}$$

where $T_0 = 273$ K is temperature at the surface. In a similar manner to Equation (1), the shear-wave attenuation, Q_S^{-1}, can be defined as

$$Q_S^{-1} = \frac{J_2}{J_1}\left(\frac{1 + \sqrt{1 + (J_2/J_1)^2}}{2}\right)^{-1} \simeq \frac{J_2}{J_1} \tag{15}$$

Xenolith and xenocryst thermobarometry. Temperature estimates across a range of depths are required to generate a series of V_S–T–P tie points in order to calibrate the regional seismic tomography models. We therefore assemble a suite of fifteen Australian paleogeotherms derived from thermobarometric analysis of mantle xenoliths and xenocrysts (Supplementary Information). These come from a range of settings between thick and thin lithosphere. Localities with thin lithosphere tend to have data obtained from whole xenolith samples, typically hosted in basaltic volcanic products. For these cases, the compositions of multiple phases (garnet, clinopyroxene, orthopyroxene and olivine) can be obtained that all equilibrated under the same pressure-temperature (P-T) conditions. In these samples, we use a thermometer[82] that exploits exchange of calcium and magnesium between orthopyroxene and clinopyroxene and a barometer[83] based upon aluminium exchange between orthopyroxene and garnet, given by equation (5) of Nickel & Green (1985). This approach therefore requires compositions of garnet, diopside (clinopyroxene) and enstatite (orthopyroxene) for each xenolith, and we only use samples with all three of these minerals present. This barometer and thermometer pair both also depend upon the temperature and pressure, respectively. These two equations are therefore solved simultaneously by iteration to obtain equilibration P-T conditions. Samples are discarded if they fail more than one of the eight oxide, cation and equilibration checks.[84]

Despite all samples containing garnet, a small number return depths as shallow as ~ 25 km (see Bullenmerri, Monaro, Mt St Martin, and Sapphire Hill). The presence of garnet in xenoliths from shallow depths is well documented. The garnet-spinel transition can occur at pressures as low as 1 GPa (~ 30 km depth) in pyroxenite and 1.5 GPa (~ 45 km depth) in lherzolite, with the exact pressure of the transition depending on relative abundance of Cr and Al in each assemblage.[85,86,84] Our shallow samples are dominantly pyroxenites and mostly give pressures larger than the 1 GPa lower limit. Of these four sites with shallower samples, we select only Bullenmerri and Monaro for the anelasticity calibration, as these geotherms also contain samples at greater depths. In both cases, the deeper samples are consistent with the shallow results.

Analyses from locations on thicker lithosphere are predominantly obtained from heavy mineral concentrates generated during diamond exploration (plus rare diamond inclusions and occasional whole peridotite xenoliths), where the association of one mineral grain with any other has been lost. Thus, the approach outlined above using multiple phases is unavailable, and we instead turn to single grain combined thermobarometers for deriving equilibration P-T conditions. For these samples, we use the chrome-in-diopside barometer that exploits the exchange of chromium between clinopyroxene and garnet (Equation (9) of Nimis & Taylor, 2000).[87] It uses only diopside compositions, but requires that garnet was also present in the source region. The associated thermometer exploits enstatite-in-diopside, again using only diopside compositions but requiring that orthopyroxene was present within the source. The temperature is given by Equation (17) of Nimis & Taylor (2000).[87] Again, these two equations must be solved by iteration to obtain P-T conditions for each diopside grain. Calibration on laboratory experiments has shown that this thermobarometer may become innacurate at low pressures and at temperatures <700°C.[84] We therefore only use P-T estimates derived from this thermobarometer that yield depths >60 km and pass both of the clinopyroxene cation and oxide checks.

There are two sources of error to consider for each suite of P-T estimates. The first is uncertainty in the microprobe analyses of elemental oxide concentrations in each of the mineral samples. For the three-mineral thermobarometer, this introduces uncertainty of ±30°C and ±10 km at low temperatures (~ 700°C), reducing to ±10°C and ±3 km by ~ 1200°C.[88] For the diopside-only thermobarometer, uncertainties are larger at ±70°C and

±12 km for low temperatures (∼ 600°C) and ±15°C and ±3 km for higher temperatures (∼ 1200°C).[88] However, these uncertainties in pressure and temperature are positively correlated, such that samples broadly move up and down the geothermal gradient, with limited effect on the best fitting geotherm. The second and more significant source of uncertainty arises from error in the thermobarometers themselves, which are calibrated on laboratory samples over a range of pressure-temperature conditions and do not necessarily trade-off in the same manner. Quoted uncertainties are ±50°C and ±15 km for the three-mineral, and ±100°C and ±15 km for the diopside-only thermobarometer.[87,84,88]

Fitting a geotherm to P-T estimates. For each locality, P-T estimates derived from thermobarometry are entered into FITPLOT[89,88] to constrain the best-fitting paleogeotherm (Supplementary Information). Within the crust, we adopt a constant conductivity of 2.5 W m^{-1} $°C^{-1}$, whilst a pressure- and temperature-dependent parameterisation is used within the mantle.[90] Bulk crustal radiogenic heat production is assumed to be 0.7 μW m^{-3}, with a standard deviation of 0.2 μW m^{-3}.[91] Crustal thickness at each location is obtained from the AusMoho model[92] with standard deviation assigned as 10% of the total thickness. We assume a potential temperature of 1330 ± 50°C, which is consistent with both seismological observations and the thickness and geochemistry of mid-ocean ridge basalts, assuming a dry lherzolite source using a corner-flow melting parameterisation.[93,94,95] Kinematic viscosity of the mantle is set to 2×10^{16} m^2 s^{-1}, with a standard deviation of 0.7 orders of magnitude, which is consistent with constraints from glacial isostatic adjustment.[96] Self-consistent parameters are used to calculate the adiabatic gradient, including a reference density of $\rho_0 = 3.3$ Mg m^{-3}, thermal expansivity of $\alpha = 3 \times 10^{-5}$ $°C^{-1}$ and specific heat capacity of $C_P = 1187$ J kg^{-1} $°C^{-1}$. Uncertainty in the crustal thickness, radiogenic heat production, mantle potential temperature, and kinematic viscosity are propagated through FITPLOT using a Monte Carlo approach. 1000 combinations of these four parameters are randomly drawn assuming Gaussian distributions of the uncertainties. Geotherms are strongly consistent in the vicinity of P-T constraints, but can vary by ±50°C when greater than ∼ 30 km from a xenolith sample (Supplementary Information).

Calibrating V_S to temperature conversion. Anelasticity parameters A_B, α_B, τ'_P, $\beta(\phi_m)$, γ, T'_η and $\lambda\phi$ have been directly constrained by forced oscillation experiments on borneol.[22] However, μ^0_U, $\frac{\partial \mu_U}{\partial T}$, $\frac{\partial \mu_U}{\partial P}$, η_r, E_a, V_a and $T_S(z)$ are material properties that must be independently determined. A widely adopted approach is to fix these parameters for a given mineral assemblage, often calculated using mineral physics tables and a thermodynamic Gibbs energy minimisation algorithm.[97,98,99,100,101] In this manner, an anelastic conversion can be used in a forward sense to map between V_S and temperature.[60,102,61,78,63] However, inferred temperature structures are variable as a result of uncertainty in the mantle's chemical composition and grain size, and differences in absolute V_S between tomography models arising from different reference models and regularisation schemes.

An alternative approach to constraining these material properties is to invert real-Earth observations of the relationship between temperature, shear-wave velocity, attenuation and viscosity in the upper mantle.[59,103,104,22] In this study, we adopt the general approach of Priestley & McKenzie (2006)[59] and Priestley & McKenzie (2013)[21] with some minor developments. The SL2013sv global V_S model[24] is stacked in oceanic regions to calculate average V_S as a function of depth and lithospheric age. The age grid and optimal thermal model for a cooling oceanic plate are taken from Richards et al. (2018).[25] At each depth slice of the tomography model, a suite of V_S versus temperature tie-points are extracted. Misfit, H_1, between predicted and observed V_S is

$$H_1 = \sqrt{\frac{1}{N}\sum_{i=1}^{N}\frac{1}{M}\sum_{j=1}^{M}\left(\frac{V_{ij}^o - V_{ij}^c}{\sigma_{ij}}\right)^2} \tag{16}$$

where V_{ij}^o are observed shear-wave velocities with associated standard deviation σ_{ij}, V_{ij}^c is the prediction from Equation (1), M is the number of age bins at a given depth and N is the number of depth slices. A second suite of tie-points is created by assuming that temperatures are isentropic at depths well below the upper thermal boundary layer. We calculate average V_S as a function of depth over oceanic regions in the global model, and over the whole spatial domain in regional models. Over the depth range 250–400 km, beyond which the resolving power of surface waves drops significantly, these values are combined with an isentrope calculated for pyrolite with a potential temperature of 1334 °C using Perple_X.[98] Misfit for the isentrope, H_2, is

$$H_2 = \sqrt{\frac{1}{N}\sum_{i=1}^{N}\left(\frac{V_i^o - V_i^c}{\sigma_i}\right)^2} \tag{17}$$

It has been observed that over the depth range 150–400 km, both V_S and Q_S^{-1} are relatively consistent for oceanic ages ≥ 100 Ma. Over this age range, we stack the QRFSI12 attenuation model,[105] generating a suite of Q_S^{-1} to V_S tie-points as a function of depth. Equations (1) and (15) are coupled such that average temperature is obtained from the average V_S, rather than assuming isentropic temperatures extend up to 150 km. Misfit, H_3, between observed and predicted attenuation is

$$H_3 = \sqrt{\frac{1}{N}\sum_{i=1}^{N}\left(\frac{Q_i^{-1\ o} - Q_i^{-1\ c}}{\sigma_i}\right)^2} \tag{18}$$

We also adopt a bulk viscosity of $\eta_{ref} = 3 \times 10^{20}$ Pa s for the upper mantle ($\sim$ 100–670 km) obtained from glacial isostatic adjustment studies,[96] and compare it to the average predicted value for 225–400 km depths obtained from Equation (7). Misfit, H_4, is calculated using

$$H_4 = \sqrt{\frac{1}{\log_{10}[\sigma_i]^2}\left(\left\{\frac{1}{N}\sum_{i=1}^{N}\log_{10}[\eta_i^c]\right\} - \log_{10}[\eta_{ref}]\right)^2} \tag{19}$$

where η_i^c is predicted viscosity and the viscosity uncertainty σ_i is assumed to be one order of magnitude. Finally, for calibration of regional tomography models where these global oceanic observations are unavailable, we take the better constrained paleogeotherms derived from thermobarometry on mantle xenoliths (Supplementary Material). Argyle, Boowinda Creek, Bullenmerri, Ellendale, Merlin, Monaro, Monk Hill, Orroroo and Wandagee are used to directly constrain each anelasticity model. None of these paleogeotherms show evidence of having been perturbed by heating events immediately prior to xenolith entrainment, and we therefore take the calculated P-T conditions to represent ambient mantle conditions immediately prior to entrainment. Paleogeotherms derived from three-mineral thermobarometer P-T estimates that are either very shallow (Mt St Martin) or pass only seven of the eight oxide and cation checks (Bow Hill, Cone 32, Sapphire Hill) are considered less robust and only used to visually check results of the conversion, as are diopside-only estimates that have a very narrow depth range (Jugiong) or exhibit large spread (Cleve). For each paleogeotherm, we extract temperatures every 5 km from the base of the thermal boundary layer up to either 125 km in regions with thick lithosphere, or 50 km for those with thin (<100 km) lithosphere. These variable top depths minimise the impact of potential crustal bleeding artefacts. Extracting $\mathrm{V}_S(z)$ values at each paleogeotherm location yields a suite of V_S to temperature tie-points. Misfit, H_5, is calculated from

$$H_5 = \sqrt{\frac{1}{N}\sum_{i=1}^{N}\frac{1}{M}\sum_{j=1}^{M}\left(\frac{V_{ij}^{o} - V_{ij}^{c}}{\sigma_{ij}}\right)^2} \tag{20}$$

where M is the number of paleogeotherms, N is the number of tie-points associated with each geotherm and σ_{ij} reflects uncertainty in the V_S measurement, assumed to be a constant 0.1 km s^{-1} which captures typical variations between different tomography models at a given location. Combined misfit, H, is given by

$$H = \frac{w_1 H_1 + w_2 H_2 + w_3 H_3 + w_4 H_4 + w_5 H_5}{w_1 + w_2 + w_3 + w_4 + w_5} \tag{21}$$

where w represents weighting applied to each misfit constraint. H is minimised in two steps. Initially, a parameter sweep is performed to identify the approximate location of the global minimum. μ_U^0 is varied between 69–82 GPa (in increments of 1 GPa), $\frac{\partial \mu}{\partial T}$ between -20 and -8 MPa °C^{-1} (2 MPa °C^{-1} increments), $\frac{\partial \mu}{\partial T}$ between 1.5–2.9 (0.2 increments), η_r between 10^{17}–10^{23} Pa s ($10^{0.5}$ Pa s increments), E_a between 100–1000 kJ mol^{-1} (100 kJ mol^{-1} increments), V_a between 0–30 cm^3 mol^{-1} (2 cm^3 mol^{-1} increments) and $\frac{\partial T_s}{\partial z}$ between 0–4.5 °C km^{-1} (0.25 °C km^{-1} increments), in line with ranges of previous estimates obtained from laboratory experiments and other studies.[21,22,106] Secondly, Powell's conjugate gradient algorithm is used to further minimise H using best-fitting parameters from the initial sweep as the starting point.[107] For calibration of the global model SL2013sv, we set $w_1 = 10$, $w_2 = 1$, $w_3 = 2$, $w_4 = 2$ and $w_5 = 0$, which yields a minimum misfit $H = 0.682$ when $\mu_U^0 = 76.3$ GPa, $\frac{\partial \mu_U}{\partial T} = -17.7$ MPa °C^{-1}, $\frac{\partial \mu_U}{\partial P} = 2.53$, $\eta_r = 1.23 \times 10^{21}$ Pa s, $E_a = 202$ kJ mol^{-1}, $V_a = 1.92$ cm^3 mol^{-1} and $\frac{\partial T_s}{\partial z} = 0.955$ °C km^{-1}. These parameters are used to convert the full three-dimensional V_S model to temperature.

For the FR12 regional model, we constrain the calibration using the nine paleogeotherms. All weights are set to zero except for $w_2 = 1$ and $w_5 = 10$, yielding minimum misfit $H = 0.578$ when $\mu_U^0 = 69.3$ GPa, $\frac{\partial \mu_U}{\partial T} = -12.3$ MPa °C^{-1}, $\frac{\partial \mu_U}{\partial P} = 2.89$, $\eta_r = 1.93 \times 10^{22}$ Pa s, $E_a = 1000$ kJ mol^{-1}, $V_a = 0$ cm^3 mol^{-1} and $\frac{\partial T_s}{\partial z} = 4.50$ °C km^{-1}. Two of the nine calibration geotherms are each constrained by only a single P-T estimate (Boowinda Creek and Orroroo). Removing these two and repeating the calibration has no impact on the inferred temperature structure (Supplementary Material). Given the relatively sparse xenolith/xenocryst coverage of Australia, our robust quality control on samples utilised in this study, and the negligible impact of excluding these geotherms, we have chosen to continue using all valid data sets to calibrate our regional tomography models.

Away from three close together sites in South Australia in the vicinity of the Gawler Craton, it is also notable that the global SL2013sv model provides a surprisingly good fit to the Australian geotherms, despite being calibrated independently (Supplementary Material). This observation is unexpected for two reasons. First, the nominal resolution of the global model is lower than the local models. There are only six seismometers in Australia (located in the far west, north and east of the continent, with none in South Australia), and the density of crossing ray paths is much lower than in Europe, Asia, North, and South America.[24] Secondly, the Australian geotherms occur in continental lithosphere that is thought to be chemically depleted by melt extraction, reducing the quantity of garnet and clinopyroxene with respect to more fertile oceanic mantle. Nevertheless, the global model calibrated on fertile mantle constraints provides a good match to independent V_S–T–P observations in depleted continental lithosphere. This result implies that temperature plays the dominant role in controlling variations in seismic wave speed in the shallow mantle, whilst the effects of compositional variation are substantially smaller.[108,59,109]

Mapping the lithosphere-asthenosphere boundary. A recent study on the thermal structure of oceanic lithosphere found that the $1175 \pm 50°$C isotherm provides a good match to seismological observations of the lithosphere-asthenosphere boundary (LAB), such as peak variation in the orientation of azimuthal anisotropy.[25] In this study, we therefore adopt this isotherm as a proxy for lithospheric thickness beneath the continents. $T(z)$ is extracted from the V_S model and $\frac{\partial T}{\partial z}$ calculated over 25 km increments. Starting from the surface and progressing downwards, when temperature passes the 1175°C threshold, LAB depth is calculated using linear interpolation, with one important exception. In locations of thick crust, low V_S values at shallow depths arising from crustal bleeding are erroneously interpreted as hot lithospheric mantle. In the regional seismic tomography models, this crustal bleeding can be observed down to $\sim$ 125 km in some locations (Figure S7). Therefore, when an inverted temperature gradient is found at shallow depths, we move on to deeper levels until temperature starts to increase with depth. This crustal bleeding is only considered down to 200 km. Maximum LAB depth is limited to 350 km or the deepest slice in the seismic tomography model. Our 1175°C isotherm LAB proxy is shallower than used in some other studies[88,21] that define the LAB using the intersection of conductive and adiabatic temperature gradients in the thermal boundary layer (typically occurring at temperatures 1350–1450°C). However, in addition to matching oceanic observations, the 1175°C isotherm corresponds to lower homologous temperatures, where uncertainty in anelasticity parameters has a smaller impact on the recovered LAB.

As in previous studies using seismic tomography,[21,110,56,65] our LAB map exhibits regions of thick lithosphere in some subductions zones (e.g. west coast of South America, south Alaska and Japan). Many of these features are likely to represent subducting slabs rather than cratonic lithosphere. None of the giant ($>$ 10 Mt of contained metal) sediment-hosted deposits is found in these settings, although some minor sedimentary copper deposits do occur, particularly in the Andes. These deposits may well represent distal components of porphyry coppers, but we have left them in our sedimentary copper dataset in line with pre-existing classification schemes. It is possible to manually exclude potential slab-related features from the analysis (Supplementary Materials). Doing so actually improves the results of statistical tests, with the chances of the relationship between sediment-hosted deposits and the edge of cratonic lithosphere being random reducing by a factor of three. This occurs because the continental area within 200 km of the 170 km LAB contour decreases from 34.3% to 31.0%, while only marginally increasing the proportion of small outlier deposits. Nevertheless, we have deliberately retained these regions in the main manuscript in order to avoid introducing subjectivity and bias into our LAB maps, as opinions are likely to differ on which features to exclude. Furthermore, some studies argue that over long periods of time, thick lithosphere may actually be generated at subduction zones by thrust stacking.[111] Thus, exclusion of these features is potentially unwarranted.

Test suites of random continental locations. In order to test the statistical significance of real deposit locations, a test suite of random points on a sphere have been generated by randomly selecting two variables, a and b, in the range 0–1 and converting into longitude, θ, and latitude, ϕ, using area-normalised relationships

$$\theta = 360 \times a \tag{22}$$

$$\phi = \frac{180}{\pi} \times \arcsin(2b - 1) \tag{23}$$

These are subsequently filtered to select only those points that lie onshore (Supplementary Information). For each location, the closest approach of the 170 km lithospheric thickness contour is calculated and the resulting distances are plotted in a cumulative distribution function (CDF).

Kolmogorov-Smirnov statistical tests. We use the *two-sample Kolmogorov-Smirnov test* to examine whether the difference between two cumulative distribution functions is significant, given their respective population sizes. The D-value is the maximum magnitude of the difference between two CDFs at any point.[31] The test calculates the probability that a D-value of this magnitude might accidentally occur, had the two CDFs been randomly selected from the same underlying population. The probability, P, is approximated using

$$P \approx \exp\left(\frac{-2pqD^2}{p+q}\right) \tag{24}$$

where p and q are the number of samples in each CDF and D is the D-value expressed as a fraction between 0 and 1. For each Kolmogorov-Smirnov test, a number of random points are generated that is equivalent to the number of real deposits of that type (109 for PbZn-CD, 147 for PbZn-MVT and 139 for sedimentary copper). Given the low sample size for some of the deposit classes, the distribution of this random set can vary somewhat from the true average distribution of random continental locations. We therefore draw a test set in this manner 100 times and report the Kolmogorov-Smirnov statistics associated with each separate test within a histogram. For PbZn-CD deposits, the D-value between the real non-weighted, regionally enhanced CDF and each random CDF is individually calculated, yielding a mean and standard deviation of $D = 0.36 \pm 0.04$, with extremes of 0.27–0.45. The equivalent values are $D = 0.27 \pm 0.02$ with extremes of 0.23–0.32 for the combined sediment-hosted deposits in Figure 2c. A D-value of 0.27 for the 395 combined sedimentary-hosted deposits suggests that the probability this CDF is drawn from randomly distributed continental points is less than 1 in 10^{12} (Supplementary Information).

Thermal modelling of lithospheric rifting. Rifting of continental lithosphere causes subsidence of the surface to form a basin that progressively infills with sediments. An initial syn-rift subsidence phase occurs during lateral extension and vertical thinning of the crust and lithospheric mantle, which is contemporaneous with normal faulting. Following cessation of extension, faulting stops and post-rift thermal subsidence occurs as hot, upwelled asthenospheric mantle conductively cools back to an equilibrium lithospheric thickness.[112] To predict the subsidence and basal heat flow of the basin, we model the thermal evolution of the lithosphere during rifting.

Following McKenzie (1978),[112] we assume thinning occurs by pure shear and that vertical heat transfer dominates. We start with the one-dimensional heat flow equation

$$\rho(T,X)C_P(T,X)\frac{\partial T}{\partial t} = \frac{\partial}{\partial z}\left[k(T,P,X)\frac{\partial T}{\partial z}\right] + H(X) \tag{25}$$

where t is time, z is depth, T is temperature, P is pressure, X is composition, ρ is density, C_P is the isobaric specific heat capacity, k is the thermal conductivity, and H is the internal radiogenic heat production.

We solve Equation (25) numerically using an unconditionally stable time- and space-centered Crank-Nicholson finite-difference scheme with a predictor-corrector step.[107] Equation (25) is recast as

$$\begin{aligned}
&-k^{n+1}_{j-\frac{1}{2}}T^{n+1}_{j-1} + \left[k^{n+1}_{j-\frac{1}{2}} + k^{n+1}_{j+\frac{1}{2}} + \frac{\left(\Delta z^{n+1}\right)^2}{\Delta t}\left(\rho^n_j C^n_{Pj} + \rho^m_j C^m_{Pj}\right)\right]T^{n+1}_j - k^{n+1}_{j+\frac{1}{2}}T^{n+1}_{j+1} = \\
&\frac{\left(\Delta z^{n+1}\right)^2}{\left(\Delta z^n\right)^2}\left\{k^n_{j-\frac{1}{2}}T^n_{j-1} - \left[k^n_{j-\frac{1}{2}} + k^n_{j+\frac{1}{2}} - \frac{\left(\Delta z^n\right)^2}{\Delta t}\left(\rho^n_j C^n_{Pj} + \rho^m_j C^m_{Pj}\right)\right]T^n_j + k^n_{j+\frac{1}{2}}T^n_{j+1} + 2(\Delta z^n)^2 H_j\right\}
\end{aligned} \tag{26}$$

where Δt is the time step, Δz is the depth spacing between nodes, and n and j are the time and depth indices, respectively. Equation (26) is solved by tridiagonal elimination.[107] For the initial predictor phase of each time step, $m = n$, whilst in the subsequent corrector phases, $m = n + 1$. We use a Lagrangian reference frame, whereby Δz is initially set to 1 km and updates using the strain rate for each timestep. Timesteps are calculated using a Courant-Friedrichs-Lewy condition with the Courant number set equal to five, such that

$$\Delta t = \min_j\left[\frac{5\Delta z^2 \rho_j C_{Pj}}{k_j}\right] \tag{27}$$

and T^{n+1} typically convergences to within a tolerance of 0.001°C after two corrector phases. The strain rate is assumed to be constant during rifting and is set by rift duration and a stretching factor, β, which gives the ratio of initial to final crustal thickness.

For the crustal layer, we adopt constant thermal parameters of $C_P = 750$ J kg^{-1} K^{-1}, $k = 2.5$ W m^{-1} K^{-1} and $\rho = 2900$ kg m^{-3}. For the mantle, conductivity is taken as the pressure- and temperature-dependent values for olivine from Grose & Afonso (2013),[80] which includes lattice and radiative contributions. For specific heat capacity in the mantle, we use the temperature-dependent parameterisation of Korenaga & Korenaga (2016).[113] Density is assumed to be purely temperature-dependent according to

$$\rho(T) = \rho_\circ \exp\left(-\alpha_0[T - T_0] + \frac{\alpha_1}{2}[T^2 - T_0^2]\right) \tag{28}$$

where $T_0 = 273$ K is the temperature at the surface and $\alpha_0 = 2.832 \times 10^{-5}$ °C^{-1} and $\alpha_1 = 0.758 \times 10^{-8}$ °C^{-2} are thermal expansivity constants calibrated from mineral physics experiments.[81] $\rho_\circ$ is the reference density at surface conditions, which is set to 3330 kg m^{-3} in regular lithospheric mantle, and 3280 kg m^{-3} in cratonic lithosphere, which has been chemically depleted by melt extraction.

For the boundary conditions, we fix the surface node to have $T^n_0 = T_0$, whilst the initial basal node has an adiabatic value of $(1606 + 0.44z)$ K, equivalent to a potential temperature of 1333°C. In cratonic areas, the lithospheric mantle is thicker than standard continental lithosphere and has been chemically depleted. During the rift phase, this basal node shallows through time and non-depleted asthenospheric mantle rises adiabatically beneath. If this basal node becomes shallower than the initial thickness of standard continental lithosphere, we update the index at which this lower boundary condition is applied to the node closest to this standard depth. Heat flow, $H(t)$, through the top of the crust is calculated according to

$$H^n = \frac{(k_0^n + k_1^n)(T_1^n - T_0^n)}{2\Delta z} \tag{29}$$

and subsidence, $S(t)$, is calculated from

$$S^n = \frac{\sum_j \rho_j^n \Delta z^n - \sum_j^{\mathrm{J}} \rho_j^0 \Delta z^0}{\rho_{\mathrm{J}} - \rho_{infill}} \tag{30}$$

where J is the index of the node at the depth of the original lithospheric thickness, ρ_{J} is the adiabatic density of undepleted mantle at this depth, and $\rho_{infill} = 2200$ kg m^{-3} is the density of material that infills the basin, which we assume to be sediments.

For each rift scenario, we select an initial lithospheric template. For regular continental lithosphere, the crustal thickness is set to 30 km and the total lithospheric thickness to 140 km, which matches results from plate cooling models of oceanic lithosphere[25] and places the 1175°C isotherm at $\sim$ 120 km. Radiogenic heat production in the mantle is set to zero, whilst the crustal value is tuned to 1.0 μW m^{-3} such that the steady state geotherm yields a surface heat flow of $\sim$ 63 mW m^{-2}, which is the average for Phanerozoic continental lithosphere.[114] For cratonic lithosphere, we assume an initial crustal thickness of 50 km, lithospheric thickness of 280 km (1175°C isotherm at $\sim$ 240 km), and crustal radiogenic heat production of 0.57 μW m^{-3}, which yields an initial surface heat flux consistent with the average of $\sim$ 48 mW m^{-2} for Archean and cratonic areas.[114] We subsequently predict the temperature of the sediment pile using the basal heat flux and a constant sediment conductivity of 2.3 W m^{-1} K^{-1}, assuming a steady state conductive geotherm and negligible internal heat generation. Further metrics for the three runs shown in Figure 4a–4c are shown in the Supplementary Materials.

References

[1] Ali, S. H. *et al.* Mineral supply for sustainable development requires resource governance. *Nature* **543**, 367–372 (2017).

[2] Schodde, R. Long term trends in global exploration – are we finding enough metal? In *11th Fennoscandian Exploration and Mining Conference, 31st October 2017* (Levi, Finland, 2017). URL `minexconsulting.com/publications/oct2017b`.

[3] Nassar, N. T., Graedel, T. E. & Harper, E. M. By-product metals are technologically essential but have problematic supply. *Science Advances* **1**, 1–11 (2015).

[4] McCuaig, T. C., Beresford, S. & Hronsky, J. Translating the mineral systems approach into an effective exploration targeting system. *Ore Geology Reviews* **38**, 128–138 (2010).

[5] Wyborn, L. A. I., Heinrich, C. A. & Jaques, A. L. Australian Proterozoic mineral systems: essential ingredients and mappable criteria. *Australian Institute of Mining and Metallurgy Annual Conference* 109–115 (1994).

[6] Bierlein, F. P., Groves, D. I., Goldfarb, R. J. & Dubé, B. Lithospheric controls on the formation of provinces hosting giant orogenic gold deposits. *Mineralium Deposita* **40**, 874–886 (2006).

[7] McCuaig, T. C. & Hronsky, J. M. A. The mineral system concept: The key to exploration targeting. In *Society of Economic Geologists Special Publication 18*, 153–175 (Society of Economic Geologists, 2014).

[8] Dentith, M., Yuan, H., Johnson, S., Murdie, R. & Piña-Varas, P. Application of deep-penetrating geophysical methods to mineral exploration: Examples from Western Australia. *Geophysics* **83**, WC29–WC41 (2018).

[9] Skirrow, R. G. *et al.* Mapping iron oxide Cu-Au (IOCG) mineral potential in Australia using a knowledge-driven mineral systems-based approach. *Ore Geology Reviews* **113** (2019).

[10] Begg, G. C. *et al.* Lithospheric, cratonic, and geodynamic setting of Ni-Cu-PGE sulfide deposits. *Economic Geology* **105**, 1057–1070 (2010).

[11] Griffin, W. L., Begg, G. C. & O'Reilly, S. Y. Continental-root control on the genesis of magmatic ore deposits. *Nature Geoscience* **6**, 905–910 (2013).

[12] Rosenbaum, G. *et al.* Subduction of the Nazca Ridge and the Inca Plateau: Insights into the formation of ore deposits in Peru. *Earth and Planetary Science Letters* **239**, 18–32 (2005).

[13] Butterworth, N. *et al.* Tectonic environments of South American porphyry copper magmatism through time revealed by spatiotemporal data mining. *Tectonics* **35**, 2847–2862 (2016).

[14] O'Reilly, S. Y., Griffin, W. L. & Pearson, N. J. Geodynamic and geophysical consequences of stealth(y) mantle metasomatism: Craton evolution and metallogeny. In *11th International Kimberlite Conference*, 4537 (2017).

[15] McCuaig, T. C., Scarselli, S., Connor, T. O., Busuttil, S. & Mccormack, N. The power of a systems approach to mineral and petroleum exploration in sedimentary basins. In *SEG Special Publication 21*, chap. 3, 39–62 (Society of Economic Geologists, 2018).

[16] Leach, D. L. *et al.* Sediment-hosted lead-zinc deposits in Earth history. *Economic Geology* **105**, 593–625 (2010).

[17] Hitzman, M. W., Selley, D. & Bull, S. Formation of sedimentary rock-hosted stratiform copper deposits through Earth history. *Economic Geology* **105**, 627–639 (2010).

[18] Manning, A. H. & Emsbo, P. Testing the potential role of brine reflux in the formation of sedimentary exhalative (sedex) ore deposits. *Ore Geology Reviews* **102**, 862–874 (2018).

[19] Huston, D. L. *et al.* Tectono-metallogenic systems – The place of mineral systems within tectonic evolution, with an emphasis on Australian examples. *Ore Geology Reviews* **76**, 168–210 (2016).

[20] Geophysical Archive Data Delivery System (GADDS) (2018). URL `geoscience.gov.au/gadds`.

[21] Priestley, K. & McKenzie, D. P. The relationship between shear wave velocity, temperature, attenuation and viscosity in the shallow part of the mantle. *Earth and Planetary Science Letters* **381**, 78–91 (2013).

[22] Yamauchi, H. & Takei, Y. Polycrystal anelasticity at near-solidus temperatures. *Journal of Geophysical Research: Solid Earth* **121**, 7790–7820 (2016).

[23] Fishwick, S. & Rawlinson, N. 3-D structure of the Australian lithosphere from evolving seismic datasets. *Australian Journal of Earth Sciences* **59**, 809–826 (2012).

[24] Schaeffer, A. J. & Lebedev, S. Global shear speed structure of the upper mantle and transition zone. *Geophysical Journal International* **194**, 417–449 (2013).

[25] Richards, F. D., Hoggard, M. J., Cowton, L. R. & White, N. J. Reassessing the thermal structure of oceanic lithosphere with revised global inventories of basement depths and heat flow measurements. *Journal of Geophysical Research: Solid Earth* **123**, 9136–9161 (2018).

[26] Huston, D. L. *et al.* Preliminary national-scale lead isotope maps of Australia. *Geoscience Australia Record* **01** (2019).

[27] Hobbs, B. E. *et al.* Geodynamic modelling as an exploration tool. In *Australasian Institute of Mining and Metallurgy Publication Series*, 34–49 (Sydney, 2000).

[28] Heinson, G., Didana, Y., Soeffky, P., Thiel, S. & Wise, T. The crustal geophysical signature of a world-class magmatic mineral system. *nature Scientific Reports* **8** (2018).

[29] Skirrow, R. G., van der Wielen, S. E., Champion, D. C., Czarnota, K. & Thiel, S. Lithospheric architecture and mantle metasomatism linked to Iron Oxide Cu-Au ore formation: Multidisciplinary evidence from the Olympic Dam region, South Australia. *Geochemistry, Geophysics, Geosystems* **19**, 2673–2705 (2018).

[30] Curtis, S. & Thiel, S. Identifying lithospheric boundaries using magnetotellurics and Nd isotope geochemistry: An example from the Gawler Craton, Australia. *Precambrian Research* **320**, 403–423 (2019).

[31] Kolmogorov, A. N. Sulla determinazione empirica di una legge di distribuzione. *Giornale dell'Istituto Italiano degli Attuari* **4**, 83–91 (1933).

[32] Menzies, M., Xu, Y., Zhang, H. & Fan, W. Integration of geology, geophysics and geochemistry: A key to understanding the North China Craton. *Lithos* **96**, 1–21 (2007).

[33] Currie, C. A. & van Wijk, J. How craton margins are preserved: Insights from geodynamic models. *Journal of Geodynamics* **100**, 144–158 (2016).

[34] Davies, D. R. & Rawlinson, N. On the origin of recent intraplate volcanism in Australia. *Geology* **42**, 1031–1034 (2014).

[35] Sloan, R. A., Jackson, J. A., McKenzie, D. P. & Priestley, K. Earthquake depth distributions in central Asia, and their relations with lithosphere thickness, shortening and extension. *Geophysical Journal International* **185**, 1–29 (2011).

[36] Gibson, G. M. *et al.* Basin architecture and evolution in the Mount Isa mineral province, northern Australia: Constraints from deep seismic reflection profiling and implications for ore genesis. *Ore Geology Reviews* **76**, 414–441 (2016).

[37] Biggs, J., Nissen, E., Craig, T., Jackson, J. & Robinson, D. P. Breaking up the hanging wall of a rift-border fault: The 2009 Karonga earthquakes, Malawi. *Geophysical Research Letters* **37** (2010). URL `Biggs_etal_2010`.

[38] Allen, P. A. & Armitage, J. J. Cratonic basins. In Busby, C. & Azor, A. (eds.) *Tectonics of Sedimentary Basins: Recent Advances*, chap. 30, 602–620 (Blackwell Publishing Ltd, 2012), 1 edn.

[39] Jordan, T. H. Composition and development of the continental tectosphere. *Nature* **274**, 544–548 (1978). `arXiv:1011.1669v3`.

[40] Huston, D. L., Pehrsson, S., Eglington, B. M. & Zaw, K. The geology and metallogeny of volcanic-hosted massive sulfide deposits: Variations through geologic time and with tectonic setting. *Economic Geology* **105**, 571–591 (2010).

[41] Regis, D. *et al.* Evidence for Neoarchean Ni-Cu-bearing mafic intrusions along a major lithospheric structure: A case study from the south Rae craton (Canada). *Precambrian Research* **302**, 312–339 (2017).

[42] Alghamdi, A. H., Aitken, A. R. & Dentith, M. C. The deep crustal structure of the Warakurna LIP, and insights on Proterozoic LIP processes and mineralisation. *Gondwana Research* **56**, 1–11 (2018).

[43] Arndt, N. T., Lesher, C. M. & Czamanske, G. K. Mantle-derived magmas and magmatic Ni-Cu-(PGE) deposits. *Economic Geology 100th Anniversary Volume* 5–24 (2005).

[44] Raymond, O. Australian Geological Provinces 2018.01 edition. *Geoscience Australia Dataset* **eCat Id: 1** (2018). URL `ecat.ga.gov.au/geonetwork`.

[45] Hitzman, M. W., Kirkham, R., Broughton, D., Thorson, J. & Selley, D. The sediment-hosted stratiform Copper ore system. *Economic Geology 100th Anniversary Volume* (2005).

[46] Cox, D. P., Lindsey, D. A., Singer, D. A., Moring, B. C. & Diggles, M. F. Sediment-hosted copper deposits of the world: Deposit models and database. *U.S. Geological Survey Open-File Report* (2007).

[47] Taylor, R. D., Leach, D. L., Bradley, D. C. & Pisarevsky, S. A. Compilation of mineral resource data for Mississippi Valley-type and clastic-dominated sediment-hosted lead-zinc deposits. *U.S. Geological Survey Open-File Report* **1297** (2009).

[48] Sillitoe, R. H. Porphyry copper systems. *Economic Geology* **105**, 3–41 (2010).

[49] Hoatson, D. M., Jaireth, S. & Jaques, A. L. Nickel sulfide deposits in Australia: Characteristics, resources, and potential. *Ore Geology Reviews* **29**, 177–241 (2006).

[50] Franklin, J. M., Gibson, H. L., Jonasson, I. R. & Galley, A. G. Volcanogenic massive sulfide deposits. *Economic Geology 100th Anniversary Volume* (2005).

[51] Sexton, J. Australian mineral occurrences collection. *Geoscience Australia Dataset* **eCat Id 73** (2011). URL `ecat.ga.gov.au/geonetwork`.

[52] Fishwick, S., Heintz, M., Kennett, B. L. N., Reading, A. M. & Yoshizawa, K. Steps in lithospheric thickness within eastern Australia, evidence from surface wave tomography. *Tectonics* **27** (2008).

[53] Priestley, K., Jackson, J. & McKenzie, D. P. Lithospheric structure and deep earthquakes beneath India, the Himalaya and southern Tibet. *Geophysical Journal International* **172**, 345–362 (2008).

[54] Debayle, E., Dubuffet, F. & Durand, S. An automatically updated S-wave model of the upper mantle and the depth extent of azimuthal anisotropy. *Geophysical Research Letters* **43**, 674–682 (2016).

[55] Ho, T., Priestley, K. & Debayle, E. A global horizontal shear velocity model of the upper mantle from multimode love wave measurements. *Geophysical Journal International* **207**, 542–561 (2016).

[56] Priestley, K., McKenzie, D. & Ho, T. A lithosphere-asthenosphere boundary - A global model derived from multimode surface-wave tomography and petrology. In Yuan, H. & Romanowicz, B. (eds.) *Geophysical Monograph 239, Lithospheric Discontinuities*, chap. 6, 111–123 (John Wiley and Sons, Washington D.C., 2018).

[57] Kennett, B. L. N., Fichtner, A., Fishwick, S. & Yoshizawa, K. Australian seismological reference model (AuSREM): Mantle component. *Geophysical Journal International* **192**, 871–887 (2013).

[58] Yoshizawa, K. Radially anisotropic 3-D shear wave structure of the Australian lithosphere and asthenosphere from multi-mode surface waves. *Physics of the Earth and Planetary Interiors* **235**, 33–48 (2014).

[59] Priestley, K. & McKenzie, D. P. The thermal structure of the lithosphere from shear wave velocities. *Earth and Planetary Science Letters* **244**, 285–301 (2006).

[60] An, M. & Shi, Y. Lithospheric thickness of the Chinese continent. *Physics of the Earth and Planetary Interiors* **159**, 257–266 (2006).

[61] Goes, S., Armitage, J., Harmon, N., Smith, H. & Huismans, R. Low seismic velocities below mid-ocean ridges: Attenuation versus melt retention. *Journal of Geophysical Research* **117** (2012).

[62] Afonso, J. C. *et al.* 3-D multiobservable probabilistic inversion for the compositional and thermal structure of the lithosphere and upper mantle: III. Thermochemical tomography in the Western-Central U.S. *Journal of Geophysical Research: Solid Earth* **121**, 7337–7370 (2016).

[63] Cammarano, F. & Guerri, M. Global thermal models of the lithosphere. *Geophysical Journal International* **210**, 56–72 (2017).

[64] Klöcking, M., White, N. J., Maclennan, J., McKenzie, D. & Fitton, J. G. Quantitative relationships between basalt geochemistry, shear wave velocity, and asthenospheric temperature beneath western North America. *Geochemistry, Geophysics, Geosystems* **19**, 3376–3404 (2018).

[65] Afonso, J. C., Salajegheh, F., Szwillus, W., Ebbing, J. & Gaina, C. A global reference model of the lithosphere and upper mantle from joint inversion and analysis of multiple data sets. *Geophysical Journal International* **217**, 1602–1628 (2019).

[66] Karato, S. Importance of anelasticity in the interpretation of seismic tomography. *Geophysical Research Letters* **20**, 1623–1626 (1993).

[67] Cammarano, F., Goes, S., Vacher, P. & Giardini, D. Inferring upper-mantle temperatures from seismic velocities. *Physics of the Earth and Planetary Interiors* **138**, 197–222 (2003).

[68] Jackson, I., Fitz Gerald, J. D., Faul, U. H. & Tan, B. H. Grain-size-sensitive seismic wave attenuation in polycrystalline olivine. *Journal of Geophysical Research* **107**, 2360 (2002).

[69] Sundberg, M. & Cooper, R. F. A composite viscoelastic model for incorporating grain boundary sliding and transient diffusion creep; Correlating creep and attenuation responses for materials with a fine grain size. *Philosophical Magazine* **90**, 2817–2840 (2010).

[70] McCarthy, C., Takei, Y. & Hiraga, T. Experimental study of attenuation and dispersion over a broad frequency range: 2. The universal scaling of polycrystalline materials. *Journal of Geophysical Research* **116** (2011).

[71] Takei, Y., Karasawa, F. & Yamauchi, H. Temperature, grain size, and chemical controls on polycrystal anelasticity over a broad frequency range extending into the seismic range. *Journal of Geophysical Research: Solid Earth* **119**, 5414–5443 (2014).

[72] Faul, U. & Jackson, I. Transient Creep and Strain Energy Dissipation: An Experimental Perspective. *Annual Review of Earth and Planetary Sciences* **43**, 541–569 (2015).

[73] Faul, U. H. & Jackson, I. The seismological signature of temperature and grain size variations in the upper mantle. *Earth and Planetary Science Letters* **234**, 119–134 (2005).

[74] Jackson, I. & Faul, U. H. Grainsize-sensitive viscoelastic relaxation in olivine: Towards a robust laboratory-based model for seismological application. *Physics of the Earth and Planetary Interiors* **183**, 151–163 (2010).

[75] Takei, Y. Effects of partial melting on seismic velocity and attenuation: A new insight from experiments. *Annual Review of Earth and Planetary Sciences* **45**, 447–470 (2017).

[76] Forsyth, D. W. Geophysical constraints on mantle flow and melt generation beneath mid-ocean ridges. *Geophysical Monograph* **71**, 1–65 (1992).

[77] Behn, M. D., Hirth, G. & Elsenbeck, J. R. Implications of grain size evolution on the seismic structure of the oceanic upper mantle. *Earth and Planetary Science Letters* **282**, 178–189 (2009).

[78] Dannberg, J. *et al.* The importance of grain size to mantle dynamics and seismological observations. *Geochemistry, Geophysics, Geosystems* **18**, 3034–3061 (2017). `arXiv:1011.1669v3`.

[79] Hirschmann, M. M. Mantle solidus: Experimental constraints and the effects of peridotite composition. *Geochemistry Geophysics Geosystems* **1** (2000).

[80] Grose, C. J. & Afonso, J. C. Comprehensive plate models for the thermal evolution of oceanic lithosphere. *Geochemistry, Geophysics, Geosystems* **14** (2013).

[81] Bouhifd, M. A., Andrault, D., Fiquet, G. & Richet, P. Thermal expansion of forsterite up to the melting point. *Geophysical Research Letters* **23**, 1143–1146 (1996).

[82] Taylor, W. R. An experimental test of some geothermometer and geobarometer formulations for upper mantle peridotites with application to the thermobarometry of fertile lherzolite and garnet websterite. *Neues Jahrbuch für Mineralogie - Abhandlungen* **172**, 381–408 (1998).

[83] Nickel, K. G. & Green, D. H. Empirical geothermobarometry for garnet peridotites and implications for the nature of the lithosphere, kimberlites and diamonds. *Earth and Planetary Science Letters* **73**, 158–170 (1985).

[84] Nimis, P. & Grütter, H. Internally consistent geothermometers for garnet peridotites and pyroxenites. *Contributions to Mineralogy and Petrology* **159**, 411–427 (2010).

[85] Gasparik, T. Two-pyroxene thermobarometry with new experimental data in the system CaO–MgO–Al203–SiO2. *Contributions to Mineralogy and Petrology* **87**, 87–97 (1984).

[86] Klemme, S. The influence of Cr on the garnet-spinel transition in the Earth's mantle: Experiments in the system MgO-Cr2O3-SiO2 and thermodynamic modelling. *Lithos* **77**, 639–646 (2004).

[87] Nimis, P. & Taylor, W. R. Single clinopyroxene thermobarometry for garnet peridotites. Part I. Calibration and testing of a Cr-in-Cpx barometer and an enstatite-in-Cpx thermometer. *Contributions to Mineralogy and Petrology* **139**, 541–554 (2000).

[88] Mather, K. A., Pearson, D. G., McKenzie, D. P., Kjarsgaard, B. A. & Priestley, K. Constraints on the depth and thermal history of cratonic lithosphere from peridotite xenoliths, xenocrysts and seismology. *Lithos* **125**, 729–742 (2011).

[89] McKenzie, D. P., Jackson, J. & Priestley, K. Thermal structure of oceanic and continental lithosphere. *Earth and Planetary Science Letters* **233**, 337–349 (2005).

[90] Osako, M., Ito, E. & Yoneda, A. Simultaneous measurements of thermal conductivity and thermal diffusivity for garnet and olivine under high pressure. *Physics of the Earth and Planetary Interiors* **143-144**, 311–320 (2004).

[91] Jaupart, C., Labrosse, S. & Mareschal, J. C. Temperatures, Heat and Energy in the Mantle of the Earth. *Treatise on Geophysics* **7**, 253–303 (2007).

[92] Kennett, B. L. N., Salmon, M., Saygin, E. & Group, A. W. AusMoho: The variation of Moho depth in Australia. *Geophysical Journal International* **187**, 946–958 (2011).

[93] Dalton, C. A., Langmuir, C. H. & Gale, A. Geophysical and Geochemical Evidence for Deep Temperature Variations Beneath Mid-Ocean Ridges. *Science* **344**, 80–83 (2014).

[94] Katz, R. F., Spiegelman, M. & Langmuir, C. H. A new parameterization of hydrous mantle melting. *Geochemistry, Geophysics, Geosystems* **4** (2003).

[95] Shorttle, O., Maclennan, J. & Lambart, S. Quantifying lithological variability in the mantle. *Earth and Planetary Science Letters* **395**, 24–40 (2014).

[96] Lau, H. C. *et al.* Inferences of mantle viscosity based on ice age data sets: Radial structure. *Journal of Geophysical Research: Solid Earth* **121**, 6991–7012 (2016).

[97] Stixrude, L. & Lithgow-Bertelloni, C. Thermodynamics of mantle minerals - I. Physical properties. *Geophysical Journal International* **162**, 610–632 (2005).

[98] Connolly, J. A. The geodynamic equation of state: What and how. *Geochemistry, Geophysics, Geosystems* **10** (2009).

[99] Stixrude, L. & Lithgow-Bertelloni, C. Thermodynamics of mantle minerals - II. Phase equilibria. *Geophysical Journal International* **184**, 1180–1213 (2011).

[100] Holland, T. J. & Powell, R. An improved and extended internally consistent thermodynamic dataset for phases of petrological interest, involving a new equation of state for solids. *Journal of Metamorphic Geology* **29**, 333–383 (2011).

[101] Cottaar, S., Heister, T., Rose, I. & Unterborn, C. BurnMan: A lower mantle mineral physics toolkit. *Geochemistry, Geophysics, Geosystems* **15**, 1164–1179 (2014).

[102] Cammarano, F., Romanowicz, B., Stixrude, L., Lithgow-bertelloni, C. & Xu, W. Inferring the thermochemical structure of the upper mantle from seismic data. *Geophysical Journal International* **179**, 1169–1185 (2009).

[103] Afonso, J. C. *et al.* 3-D multiobservable probabilistic inversion for the compositional andthermal structure of the lithosphere and upper mantle. I: a priori petrological information and geophysical observables. *Journal of Geophysical Research: Solid Earth* **118**, 2586–2617 (2013).

[104] Afonso, J. C., Fullea, J., Yang, Y., Connolly, J. A. & Jones, A. G. 3-D multi-observable probabilistic inversion for the compositional and thermal structure of the lithosphere and upper mantle. II: General methodology and resolution analysis. *Journal of Geophysical Research: Solid Earth* **118**, 1650–1676 (2013).

[105] Dalton, C. A., Ekström, G. & Dziewonski, A. M. Global seismological shear velocity and attenuation: A comparison with experimental observations. *Earth and Planetary Science Letters* **284**, 65–75 (2009).

[106] Jain, C., Korenaga, J. & Karato, S. I. On the grain size sensitivity of olivine rheology. *Journal of Geophysical Research: Solid Earth* **123**, 674–688 (2018).

[107] Press, W. H., Teukolsky, S. A., Vetterling, W. T. & Flannery, B. P. *Numerical recipes in Fortran* (Cambridge University Press, 1992), 2 edn.

[108] Goes, S., Govers, R. & Vacher, P. Shallow mantle temperatures under Europe from P and S wave tomography. *Journal of Geophysical Research* **105**, 11153–11169 (2000).

[109] Schutt, D. L. & Lesher, C. E. Effects of melt depletion on the density and seismic velocity of garnet and spinel lherzolite. *Journal of Geophysical Research* **111** (2006).

[110] Steinberger, B. & Becker, T. W. A comparison of lithospheric thickness models. *Tectonophysics* 1–14 (2016).

[111] Cook, F. A., Van Der Velden, A. J., Hall, K. W. & Roberts, B. J. Frozen subduction in Canada's Northwest Territories: Lithoprobe deep lithospheric reflection profiling of the western Canadian Shield. *Tectonics* **18**, 1–24 (1999).

[112] McKenzie, D. P. Some remarks on the development of sedimentary basins. *Earth and Planetary Science Letters* **40**, 25–32 (1978).

[113] Korenaga, T. & Korenaga, J. Evolution of young oceanic lithosphere and the meaning of seafloor subsidence rate. *Journal of Geophysical Research: Solid Earth* **121**, 6315–6332 (2016).

[114] Lucazeau, F. Analysis and mapping of an updated terrestrial heat flow data set. *Geochemistry, Geophysics, Geosystems* **20**, 4001–4024 (2019).

[115] Yoshizawa, K. & Kennett, B. L. N. Multimode surface wave tomography for the Australian region using a three-stage approach incorporating finite frequency effects. *Journal of Geophysical Research: Solid Earth* **109**, 1–19 (2004).

[116] Fichtner, A., Kennett, B. L. N., Igel, H. & Bunge, H.-P. Full waveform tomography for radially anisotropic structure: New insights into present and past states of the Australasian upper mantle. *Earth and Planetary Science Letters* **290**, 270–280 (2010).

[117] Fichtner, A., Igel, H., Bunge, H.-P. & Kennett, B. L. N. Simulation and inversion of seismic wave propagation on continental scales based on a spectral-element method. *Journal of Numerical Analysis, Industrial and Applied Mathematics* **4**, 11–22 (2009).

[118] Fichtner, A., Kennett, B. L. N., Igel, H. & Bunge, H.-P. Full seismic waveform tomography for upper-mantle structure in the Australasian region using adjoint methods. *Geophysical Journal International* **179**, 1703–1725 (2009).

[119] Davies, D. R., Rawlinson, N., Iaffaldano, G. & Campbell, I. H. Lithospheric controls on magma composition along Earth's longest continental hotspot track. *Nature* **525**, 511–514 (2015).

[120] Czarnota, K., Roberts, G. G., White, N. J. & Fishwick, S. Spatial and temporal patterns of Australian dynamic topography from river profile modeling. *Journal of Geophysical Research: Solid Earth* **119**, 1384–1424 (2014).

[121] Artemieva, I. M. Global 1 1 thermal model TC1 for the continental lithosphere: Implications for lithosphere secular evolution. *Tectonophysics* **416**, 245–277 (2006).

[122] Bird, P., Liu, Z. & Rucker, W. K. Stresses that drive the plates from below: Definitions, computational path, model optimization, and error analysis. *Journal of Geophysical Research: Solid Earth* **113** (2008).

[123] Pasyanos, M. E., Masters, T. G., Laske, G. & Ma, Z. LITHO1.0: An updated crust and lithospheric model of the Earth. *Journal of Geophysical Research: Solid Earth* **119**, 2153–2173 (2014).

[124] Hayes, G. P. *et al.* Slab2, a comprehensive subduction zone geometry model. *Science* **362**, 58–61 (2018).

Acknowledgments: This work is a contribution to the Australian Government's Exploring for the Future program. We are grateful to B. Steinberger, N. Rawlinson, K. Yoshizawa and B. Kennett for sharing lithospheric thickness maps. We thank J.C. Afonso, J. Austermann, G. Begg, R. Blewett, A. Bufe, D. Champion, R. Davies, B. Delbridge, M. Doublier, R. Fu, S. Goes, A. Gorbatov, B. Hodgin, B. Holtzman, J. Kingslake, T. Mackey, P. McFadden, D. McKenzie, J. Mitrovica, D. Müller, P. Nimis, E. Powell, K. Priestley, D. Schutt, O. Shorttle, R. Skirrow, S. Stephenson, Y. Takei & J. Winterbourne for their assistance and discussions. Two anonymous reviewers provided helpful feedback. MH acknowledges support from the National Aeronautics and Space Administration grant NNX17AE17G and the Donors of American Chemical Society Petroleum Research Fund (59062-DNI8). FR acknowledges support from the Schmidt Science Fellows program, in partnership with the Rhodes Trust. KC and DH publish with the permission of the CEO of Geoscience Australia. Geoscience Australia eCat ID 132624.

Author contributions: This relationship was discovered by KC, and the study was conceived and designed by KC and MH. KC and DH compiled deposit databases. LJ collated Australian xenolith data. Thermobarometry and paleogeotherm modelling was done by LJ, FR and MH. FR and MH developed shear-wave to temperature conversion scheme. FR calibrated anelasticity parameterisations. MH generated LAB maps, performed statistical tests, made figures and compiled supplementary materials. SG and MH performed thermal modelling of rifting. The paper was written by KC and MH, with guidance from all authors.

Competing interests: The authors declare no competing financial interests.

Data availability: All data is available in the manuscript or the supplementary materials. Correspondence should be addressed to M. Hoggard (mark_hoggard@fas.harvard.edu) and K. Czarnota (karol.czarnota@ga.gov.au).

Supplementary Information:

- Additional Materials
- Figures S1–S33
- References (115–124)

Supplementary Information for "Gigayear stability of cratonic edges controls global distribution of sediment-hosted metals"

Mark J. Hoggard*[,1,2], Karol Czarnota*[,3,4], Fred D. Richards[1], David L. Huston[3], A. Lynton Jaques[4] & Sia Ghelichkhan[4]

1. Department of Earth & Planetary Sciences, Harvard University, 20 Oxford Street, Cambridge, MA 02138, USA.
2. Lamont-Doherty Earth Observatory, Columbia University, 61 Rte 9W, Palisades, NY 10964, USA.
3. Geoscience Australia, GPO Box 378, Canberra ACT 2601, Australia.
4. Research School of Earth Sciences, Australian National University, Canberra, ACT 0200, Australia

*mark_hoggard@fas.harvard.edu; karol.czarnota@ga.gov.au

Contents

Additional Supporting Information (Files uploaded separately)

1. Global and Australian lithospheric thickness maps in ASCII format.
2. Database of six major classes of base metal deposit.
3. Location and diopside compositions for xenocryst thermobarometry.
4. Fifteen Australian FITPLOT geotherms in ASCII format.

Australian seismic tomography model comparison

Our LAB maps are based on the most recent, high-resolution shear wave tomography models. For the global map, we use SL2013sv[24] which is an upper mantle-only model built from a combination of body and surface waves, including fundamental and higher modes. Periods considered are 11–450 s, $\sim 750,000$ seismograms are included, and misfits are calculated between synthetics and the full waveform up to the 9^{th} overtone. Crucially, simultaneous inversion for the crustal model results in minimal smearing of slow crustal velocities down into the upper mantle, thereby allowing us to use more depth slices in our V_S to temperature calibration. Checkerboard resolution tests indicate that features ~ 600 km in diameter at lithospheric depths are generally well resolved. Finer features should be resolvable in regions with dense ray path coverage, such as North America, Europe and southeast Asia.

The SL2013sv model contains only 6 seismometers in Australia, so has limited resolution within this continent. Therefore, we also investigate three regional seismic tomography models to generate high resolution maps for the Australian continent. The main model used throughout this paper is the radially isotropic V_S model FR12[23], which is derived from Rayleigh wave travel times.[52] Periods considered are 50–120 s and the fundamental and first four higher modes have been used where possible, leading to good sensitivity down to ~ 250 km depths. It contains a greater number of source–receiver paths ($> 13,000$) compared to other Australian models. However, it uses an *a priori* crustal model that remains fixed throughout the inversion, resulting in noticeable smearing of crustal velocities into the upper mantle. Checkerboard tests indicate that features ~ 300 km in diameter at lithospheric depths are well resolved.

The second regional model is AuSREM[57] and is a hybrid model constructed by linear combination of several previous studies. It combines FR12 with YK04[115] and AMSAN.19.[116] YK04 is a radially anisotropic Rayleigh wave model using > 8000 ray paths for the fundamental mode and ~ 2000 for the first three higher modes, yielding a maximum period range of 40–150 s. It includes off-great circle and finite frequency effects, but also uses a fixed crustal model. AMSAN.19 is a radially anisotropic, 3D waveform, spectral element model that uses an inversion scheme based on the adjoint approach.[117,118] Periods considered are 30–200 s and a fixed crustal model is used. Due to the computationally intensive methodology, $\sim 3,000$ waveforms are used in this inversion.

The third and final regional model considered in this study is the radially anisotropic Y14.[58] It combines Rayleigh waves (8000 fundamental, ~ 2500 higher mode) and Love waves (approximately two-thirds as many) with periods $\sim$ 25–200s, corrected for local crustal structure using a fixed crustal model. It adopts the same three-step inversion procedure as YK04.[115] All three models are plotted alongside the global SL2013sv model in Figures S1, S2 and S3. At any given location within the continent, V_S varies between models by ~ 0.1 km s^{-1}.

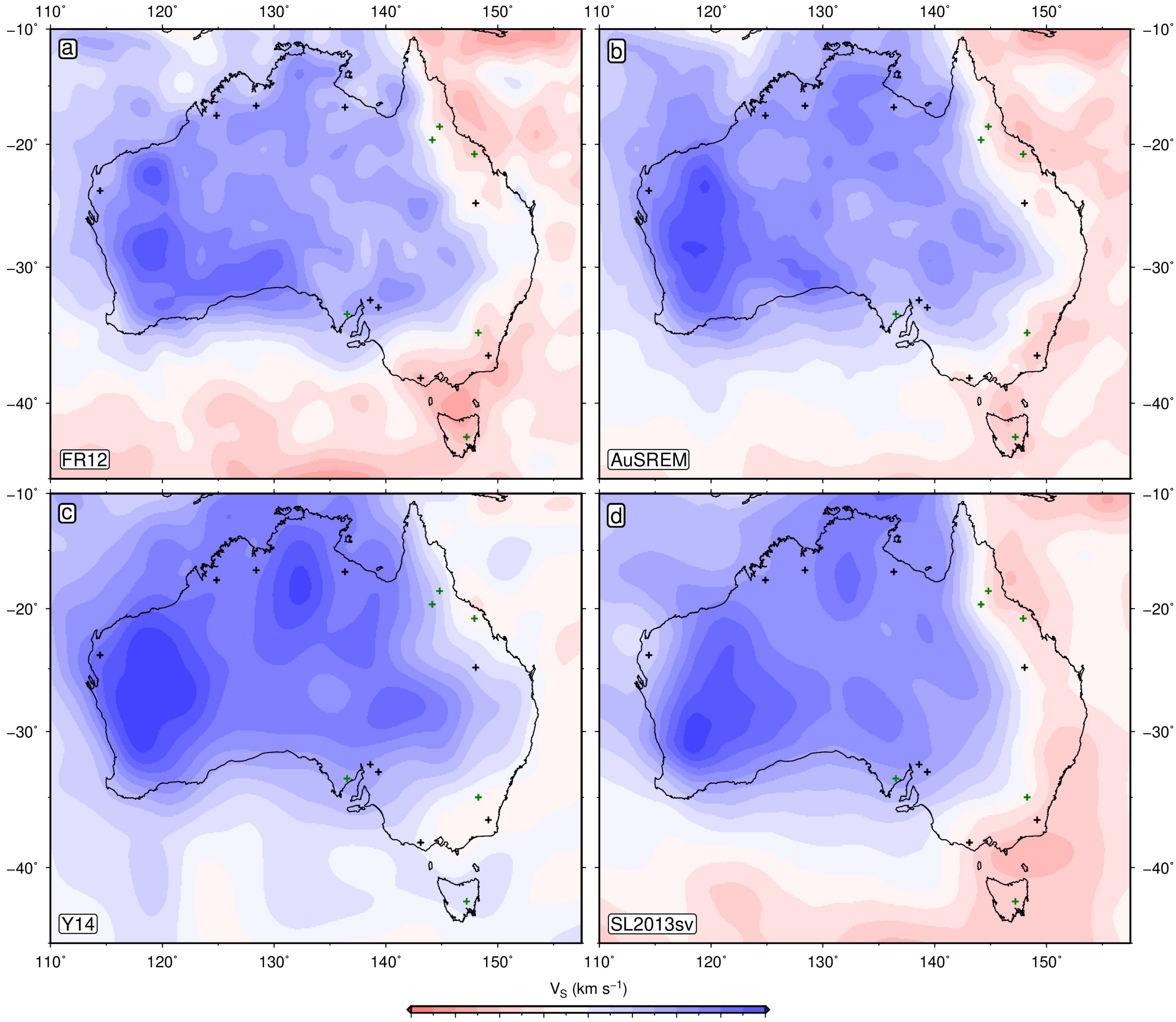

Figure S1: **100 km depth slice through Australian seismic tomography models.** Black/green crosses = paleogeotherms used as constraints/tests in anelasticity calibration. (a) FR12 = regional isotropic V_S [23]. (b) AuSREM = regional V_{SV} [57]. (c) Y14 = regional V_{SV} [58]. (d) SL2013sv = global V_{SV} [24].

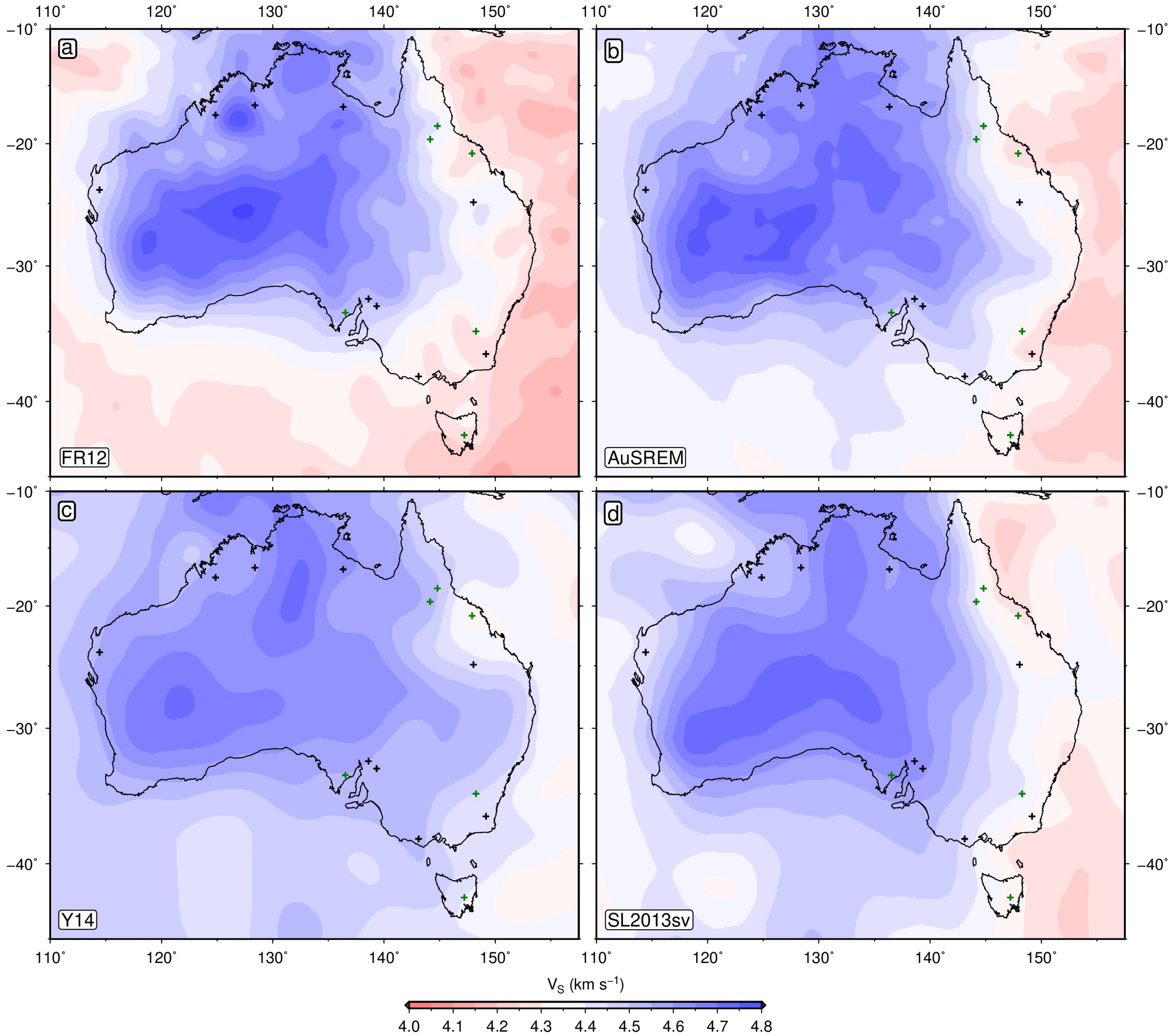

Figure S2: **175 km depth slice through Australian seismic tomography models.** Black/green crosses = paleogeotherms used as constraints/tests in anelasticity calibration. (a) FR12 = regional isotropic V_S [23]. (b) AuSREM = regional V_{SV} [57]. (c) Y14 = regional V_{SV} [58]. (d) SL2013sv = global V_{SV} [24].

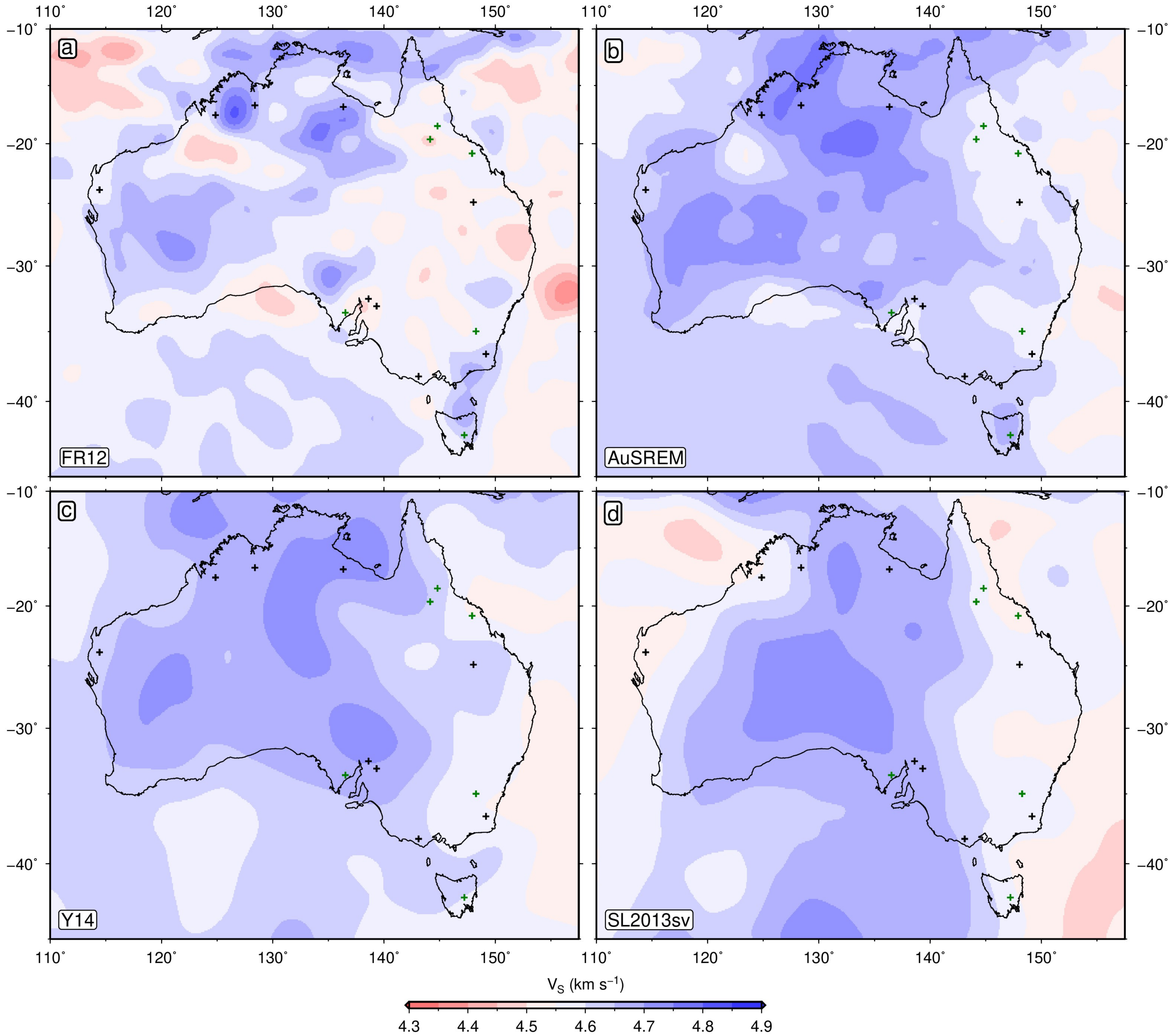

Figure S3: **250 km depth slice through Australian seismic tomography models.** Black/green crosses = paleogeotherms used as constraints/tests in anelasticity calibration. (a) FR12 = regional isotropic V_S [23]. (b) AuSREM = regional V_{SV} [57]. (c) Y14 = regional V_{SV} [58]. (d) SL2013sv = global V_{SV} [24].

Thermobarometry and Regional Calibration of Tomography Models

Temperature estimates across a range of depths are required to generate a series of V_S-T-P tie points in order to calibrate the regional seismic tomography models. We therefore assemble a suite of Australian paleogeotherms derived from thermobarometric analysis of mantle xenoliths and xenocrysts from fifteen locations in thick and thin lithosphere (Figure S4). The resulting P-T estimates are entered into FITPLOT to generate the palaeogeotherms shown in Figure S5 (Methods).

The results of regional calibration using the paleogeotherms are shown in Figures S6 and S7. Note that the global model SL2013sv yields good fits to paleogeotherms away from south Australia (Monk Hill, Orroroo and Cleve), despite being lower resolution than the local models and being calibrated completely independently of this information (red lines in Figure S7). Conversely, regional models often provide a poorer fit to the full range of the paleogeotherms and can exhibit substantial crustal bleeding artefacts at depths shallower than $\sim$ 125 km. Generally amongst the regional models, FR12 performs the best, followed by AuSREM and then Y14.

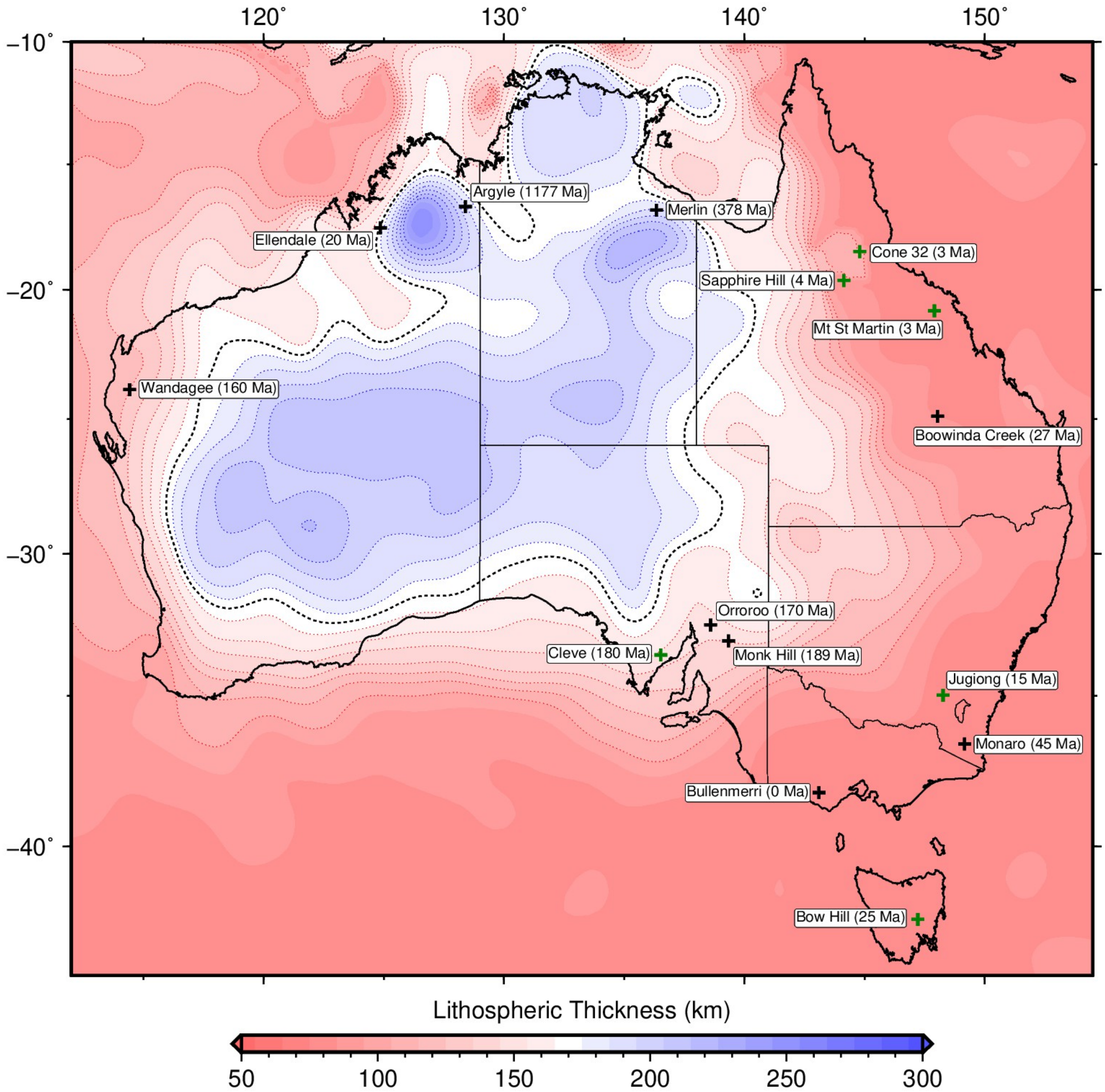

Figure S4: **Location of Australian xenolith and xenocryst suites.** Labels give site name and age (in million years); black crosses = locations used to constrain anelasticity calibration, green crosses = locations used to visually test validity of results; red/blue colours = lithospheric thickness (from Figure 1b), derived from FR12 seismic tomography model.[23]

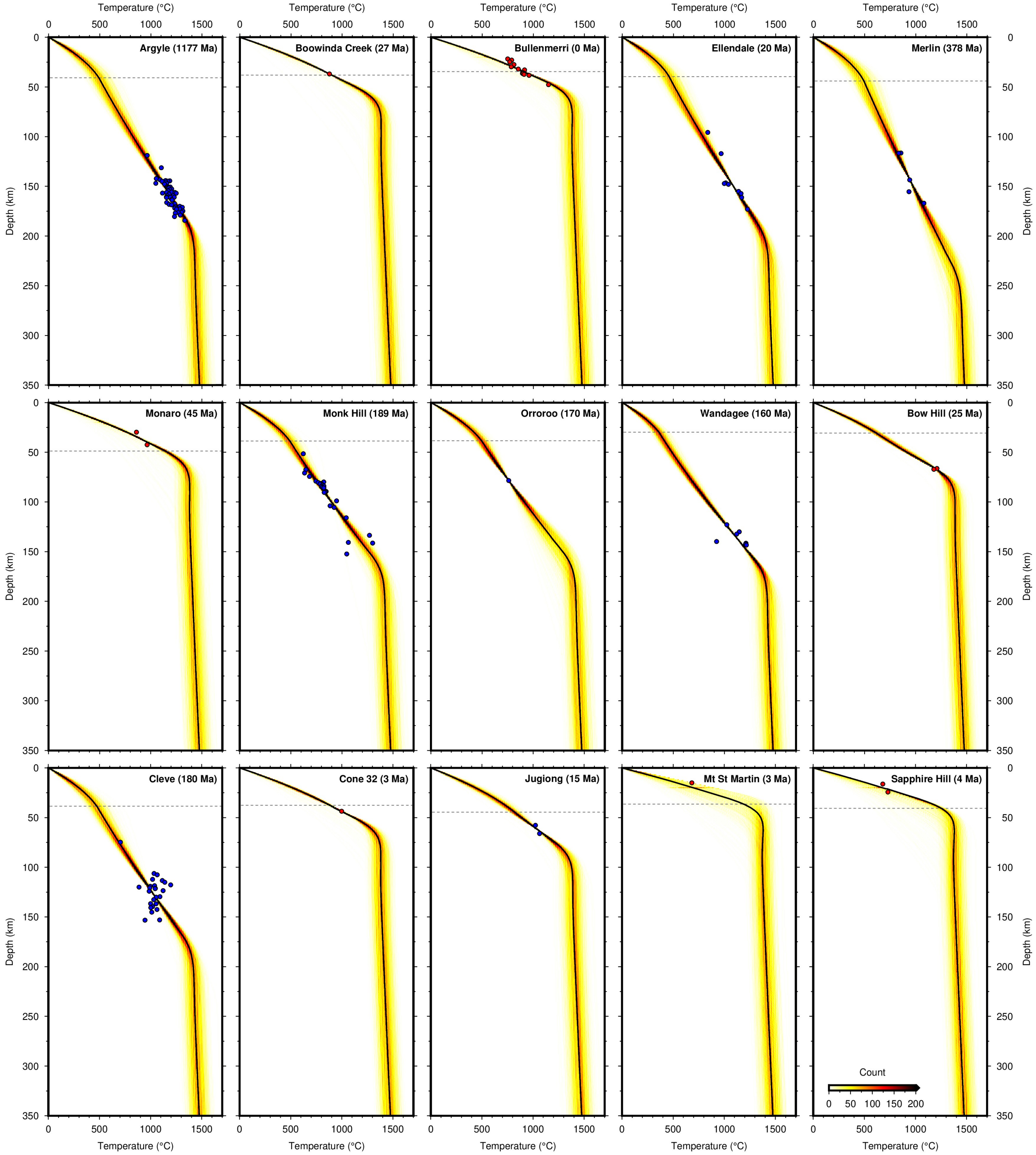

Figure S5: **Australian paleogeotherms derived from xenolith and xenocryst thermobarometry.** Labels give site name and age (in million years) from Figure S4; red circles = P-T estimates derived from multiphase thermobarometry[83,82]; blue circles = P-T estimates derived from single chrome diopside thermobarometry[87]; dashed line = crustal thickness from AusMoho[92]; solid line = FITPLOT optimal paleogeotherm[88]; coloured band = spread of 1000 geotherms from Monte Carlo FITPLOT analysis.

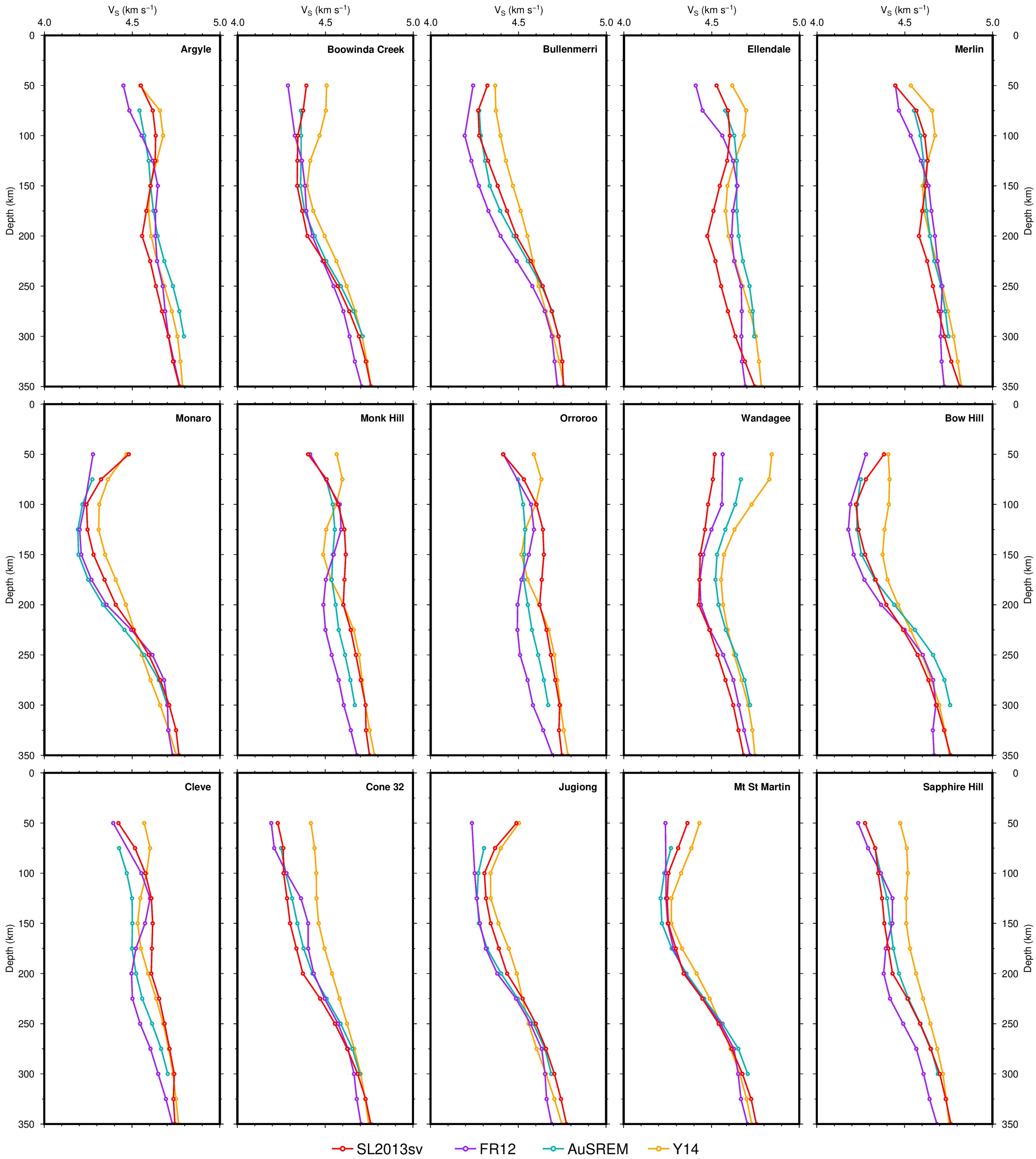

Figure S6: **$\mathbf{V}_S$ as a function of depth at sites of fifteen Australian paleogeotherms.** Labels give site name (locations in Figure S4); red = global SL2013sv model[24]; purple = regional FR12 model[23]; blue = regional AuSREM model[57]; orange = regional Y14 model[58].

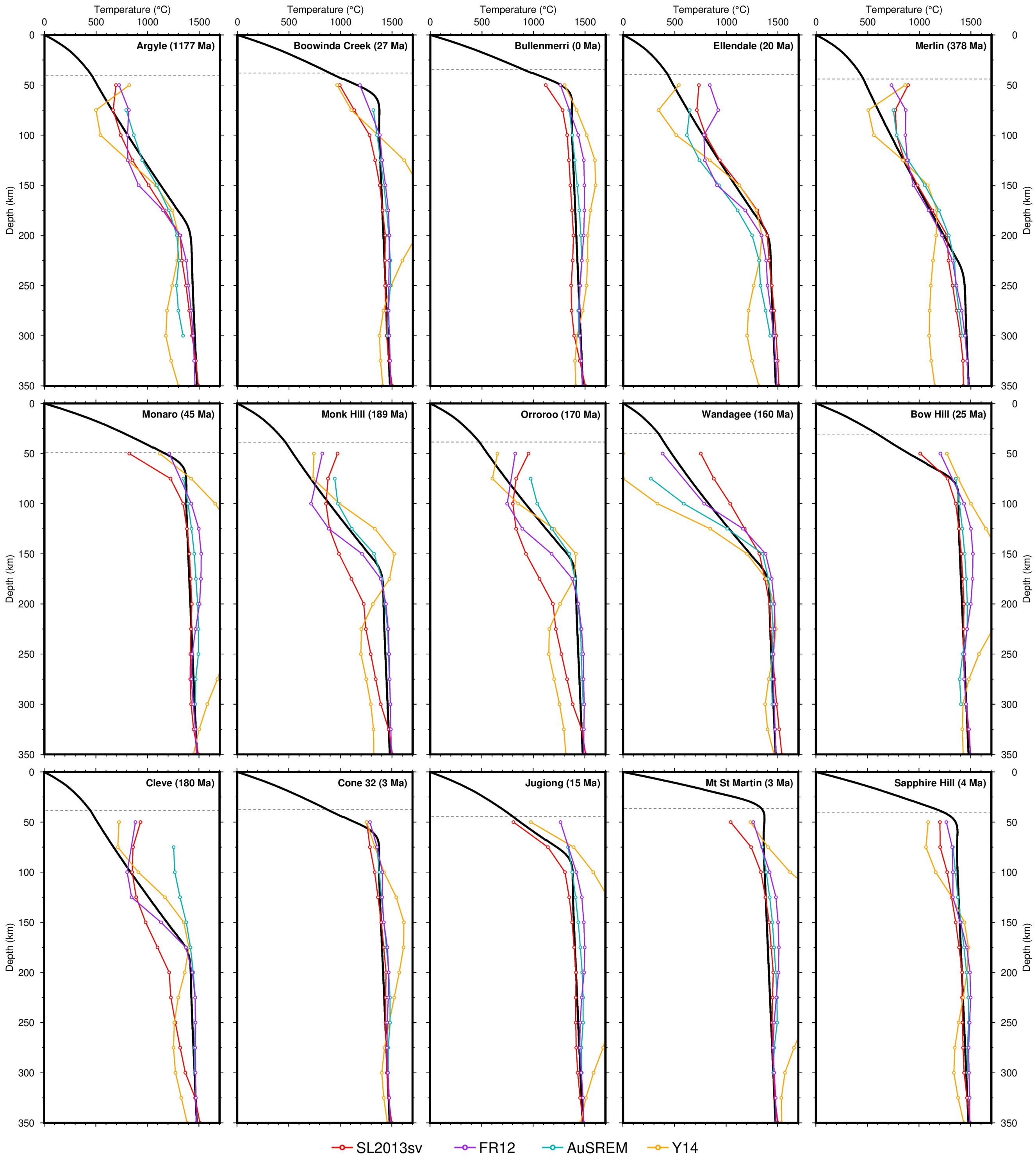

Figure S7: **Calibration of anelasticity parameterisation on Australian paleogeotherms.** Labels give site name and inferred age of paleogeotherms in million years (locations in Figure S4); sites Argyle to Wandagee are used to constrain calibration; sites Bow Hill to Sapphire Hill are used to visually check output; dashed line = crustal thickness from AusMoho[92]; solid line = optimal FITPLOT geotherm from Figure S5; purple = regional FR12 model[23]; blue = regional AuSREM model[57]; orange = regional Y14 model[58]; red = global SL2013sv model[24], for comparison, calibrated independently of palaeogeotherm constraints.

It is important to note that of the nine geotherms used to calibrate the anelasticity parameterisation for the regional FR12 model, two are only constrained by a single P-T estimate (Orroroo and Boowinda Creek). We have therefore tested the effect of removing these two sites from the calibration scheme. As Figure S8 shows, there is no discernible effect on the inferred temperature structure. Given this result and that these two samples pass all of the thermobarometry cation and oxide tests, we have chosen to keep Orroroo and Boowinda Creek within the set of nine geotherms used in calibration of local tomography models.

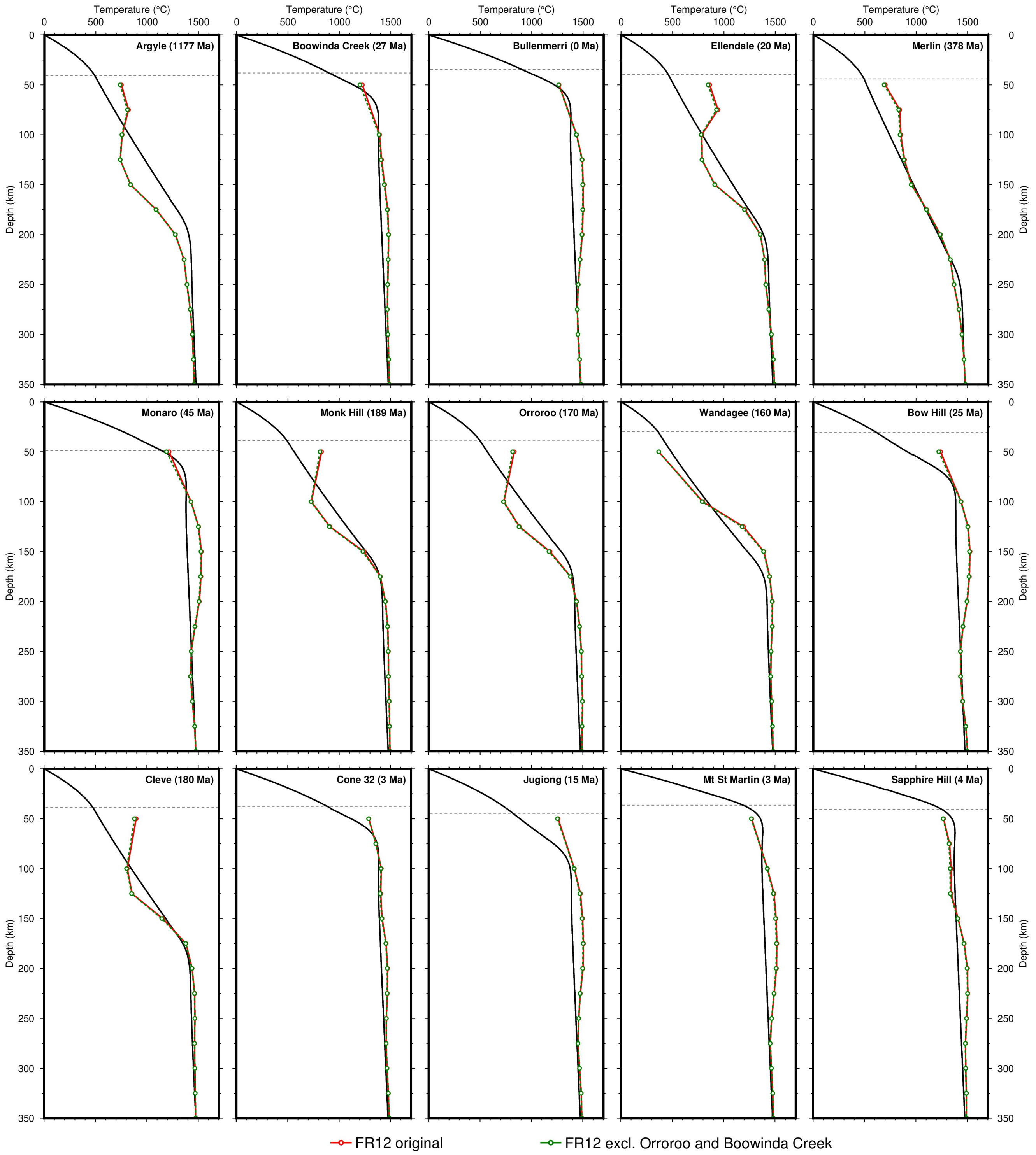

Figure S8: **Calibration of anelasticity parameterisation on Australian paleogeotherms.** Labels give site name and inferred age of paleogeotherms in million years (locations in Figure S4); red line = FR12 model calibrated using sites Argyle through Wandagee; green line = same but excluding Boowinda Creek and Orroroo from the calibrations set.

Australian Lithospheric Thickness Maps

For each of the individually calibrated seismic tomography models in this study, we have mapped out the LAB in a consistent manner. The resulting maps for Australia are shown in Figure S9, whilst in Figure S10 we compare our preferred FR12 regional model to previously published maps of LAB depth beneath Australia.

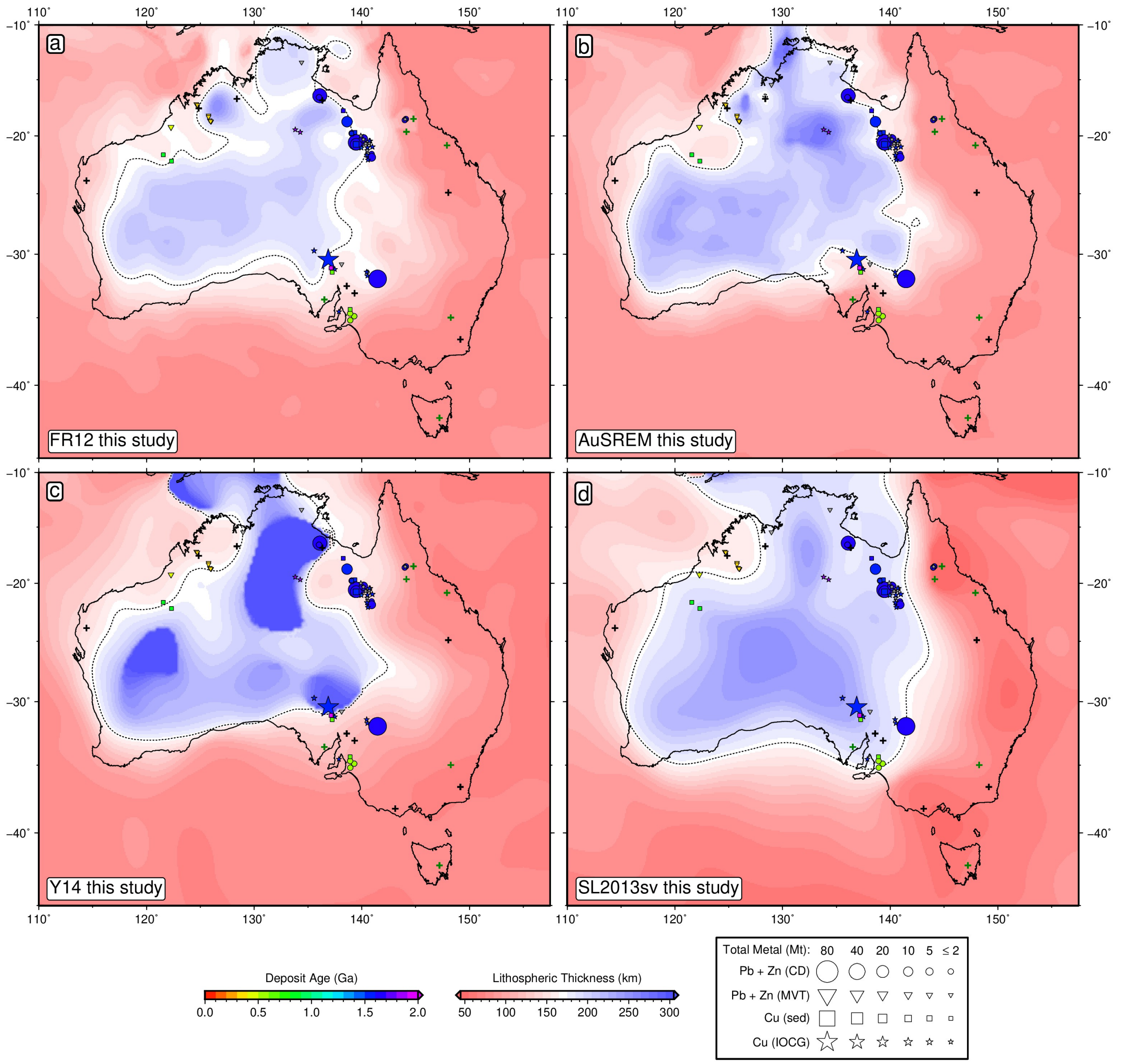

Figure S9: **Depth to lithosphere-asthenosphere boundary from individually calibrated Australian seismic tomography models.** Black contour = 170 km LAB thickness; green/black crosses = paleogeotherms used/unused in anelasticity calibration; other symbols = sediment-hosted deposit locations; area proportional to estimate of total contained mass of metal (MT = megatonnes); unknown deposit size given 2 Mt symbol; colour = ore body formation age (billion years); unknown age plotted in grey; circles = clastic-dominated lead-zinc (PbZn-CD); triangles = Mississippi Valley type lead-zinc (PbZn-MVT); squares = sedimentary copper (Cu-sed); stars = iron-oxide-copper-gold (IOCG). (a) based on FR12.[23] (b) based on AuSREM.[57] (c) based on Y14.[58] (d) based on global SL2013sv.[24]

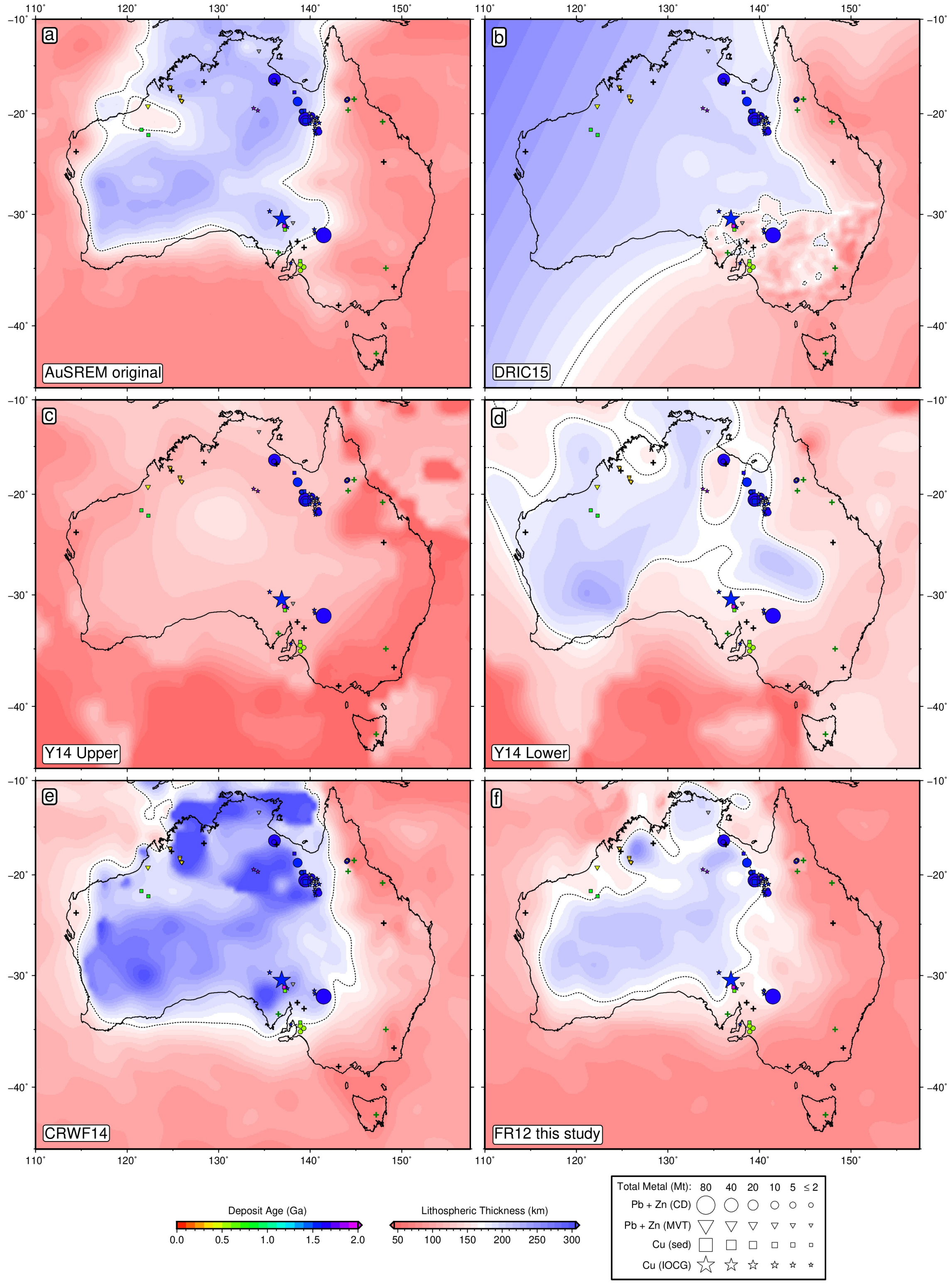

Figure S10: **Depth to lithosphere-asthenosphere boundary beneath Australia from previous studies.** Black contour = 170 km LAB thickness; green/white crosses = paleogeotherms used/unused in anelasticity calibration; other symbols = sediment-hosted deposit locations; area proportional to estimate of total contained mass of metal (MT = megatonnes); unknown deposit size given 2 Mt symbol; colour = ore body formation age (billion years); unknown age plotted in grey; circles = clastic-dominated lead-zinc (PbZn-CD); triangles = Mississippi Valley type lead-zinc (PbZn-MVT); squares = sedimentary copper (Cu-sed); stars = iron-oxide-copper-gold (IOCG). (a) Original AuSREM.[57] (b) DRIC15.[119] (c) Upper bound of Y14.[58] (d) Lower bound of Y14.[58] (e) CRWF14[120], derived using FR12 tomography.[23] (f) FR12 LAB model generated in this study.

Histogram of Global Lithospheric Thickness

Global LAB thickness derived from the SL2013sv model[24] reveals a bi-modal population with peaks at 80 km and 190 km, separated by a minimum at 150 km (Figure S11). There is also a noticeable drop-off deeper than 200 km, which we attribute to a change in the gradient of V_S with depth in the initial starting profile used to construct the tomography model.

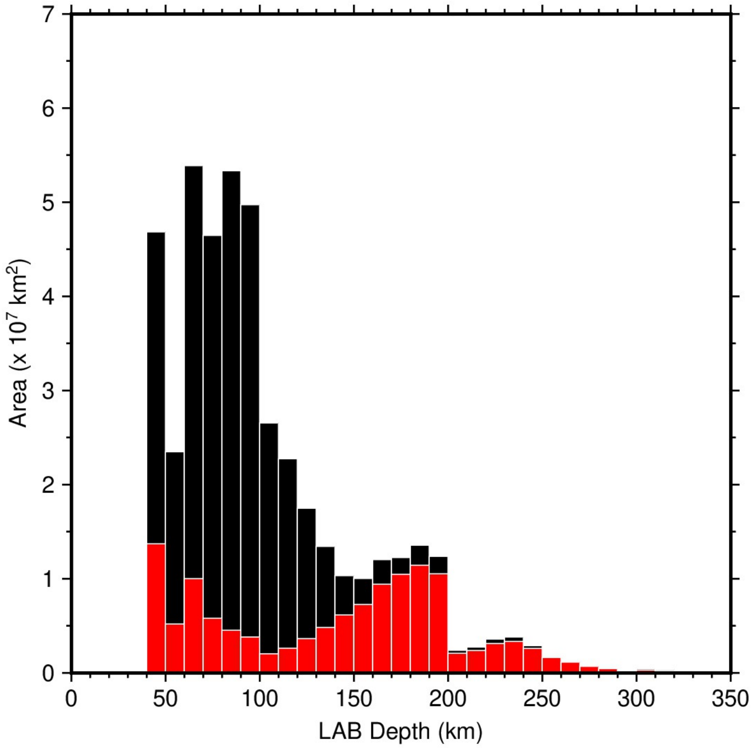

Figure S11: **Area-weighted histogram of global LAB depths.** LAB derived from the SL2013sv tomography model[24]; black bars = oceanic regions; red bars = continental regions.

Previously Published Global LAB Maps

For comparison, we provide seven previously published global lithosphere-asthenosphere boundary (LAB) maps derived from a mixture of heat flow data, seismic tomography datasets, and potential field data. Interestingly, many giant sediment hosted mineral deposits lie along LAB edges defined by these other studies, testifying to the veracity of the observed relationship.

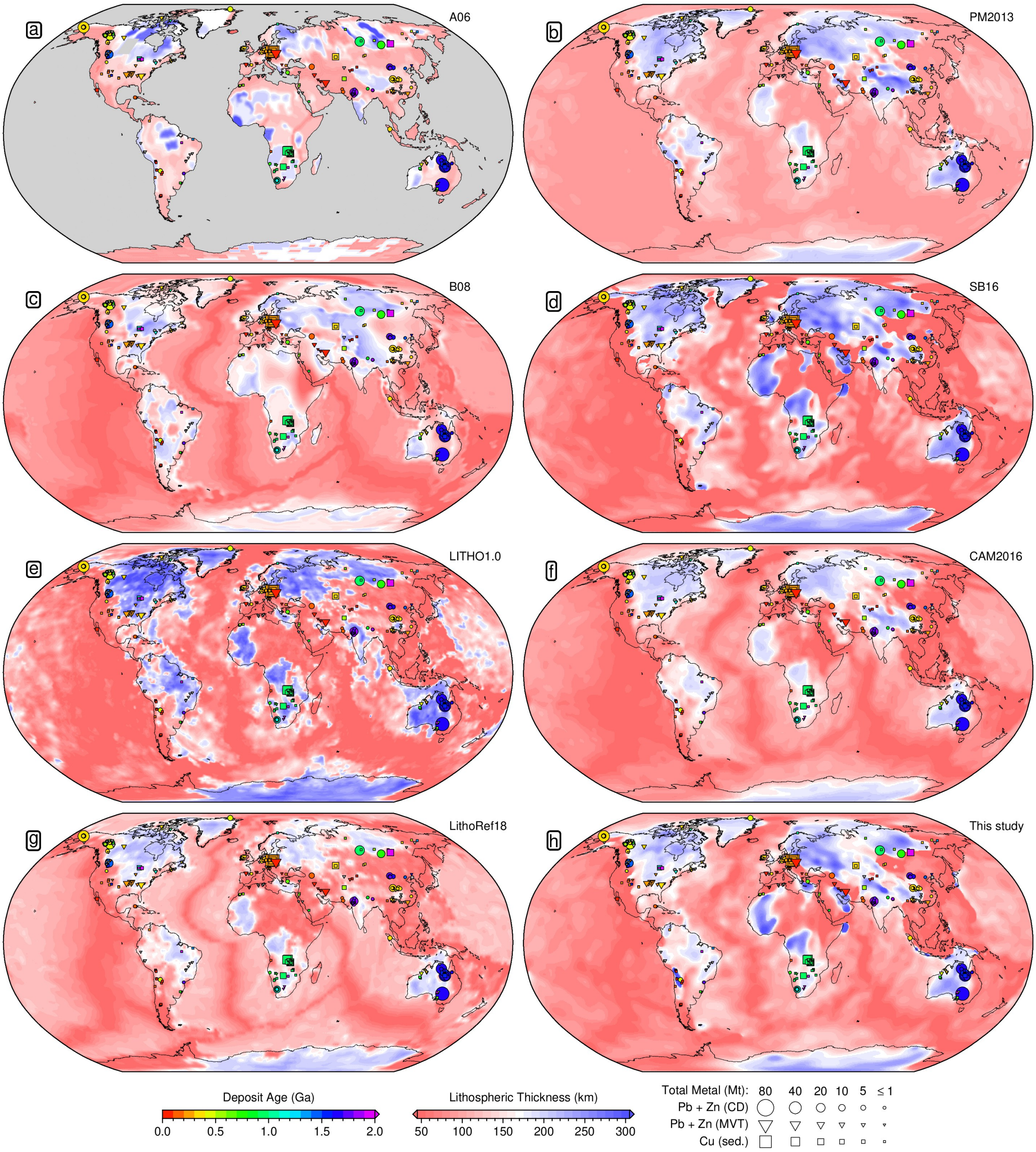

Figure S12: **Previously published global maps of depth to the lithosphere-asthenosphere boundary.** Symbols = sediment-hosted deposit locations; area proportional to estimate of total contained mass of metal (MT = megatonnes); unknown deposit size given 1 Mt symbol; colour = ore body formation age (billion years); unknown age plotted in grey; circles = clastic-dominated lead-zinc (PbZn-CD); triangles = Mississippi Valley type lead-zinc (PbZn-MVT); squares = sedimentary copper (Cu-sed). (a) LAB derived from surface heat flow measurements[121]; (b) LAB derived from surface wave tomography[21]; (c) LAB derived from vertical shear-wave travel time anomalies in the continents[122]; (d) LAB[110] derived from SL2013sv tomography model[24]; (e) LAB derived from surface wave tomography[123]; (f) LAB derived from surface wave tomography[56]; (g) LAB derived from joint inversion of seismic, potential field and geochemical data[65]; (h) LAB derived in this study using SL2013sv tomography model[24].

LAB maps derived from calibration of other global tomography models

We have obtained two additional recent surface wave tomography models that each have global coverage (3D2015-07Sv and CAM2016;[54];[56]). We have calibrated each model in the same manner as SL2013sv and generated maps of lithospheric thickness (Figure S13). All three maps are visually similar and show robust relationships with sediment-hosted deposits, although SL2013sv performs the best and is used throughout this study.

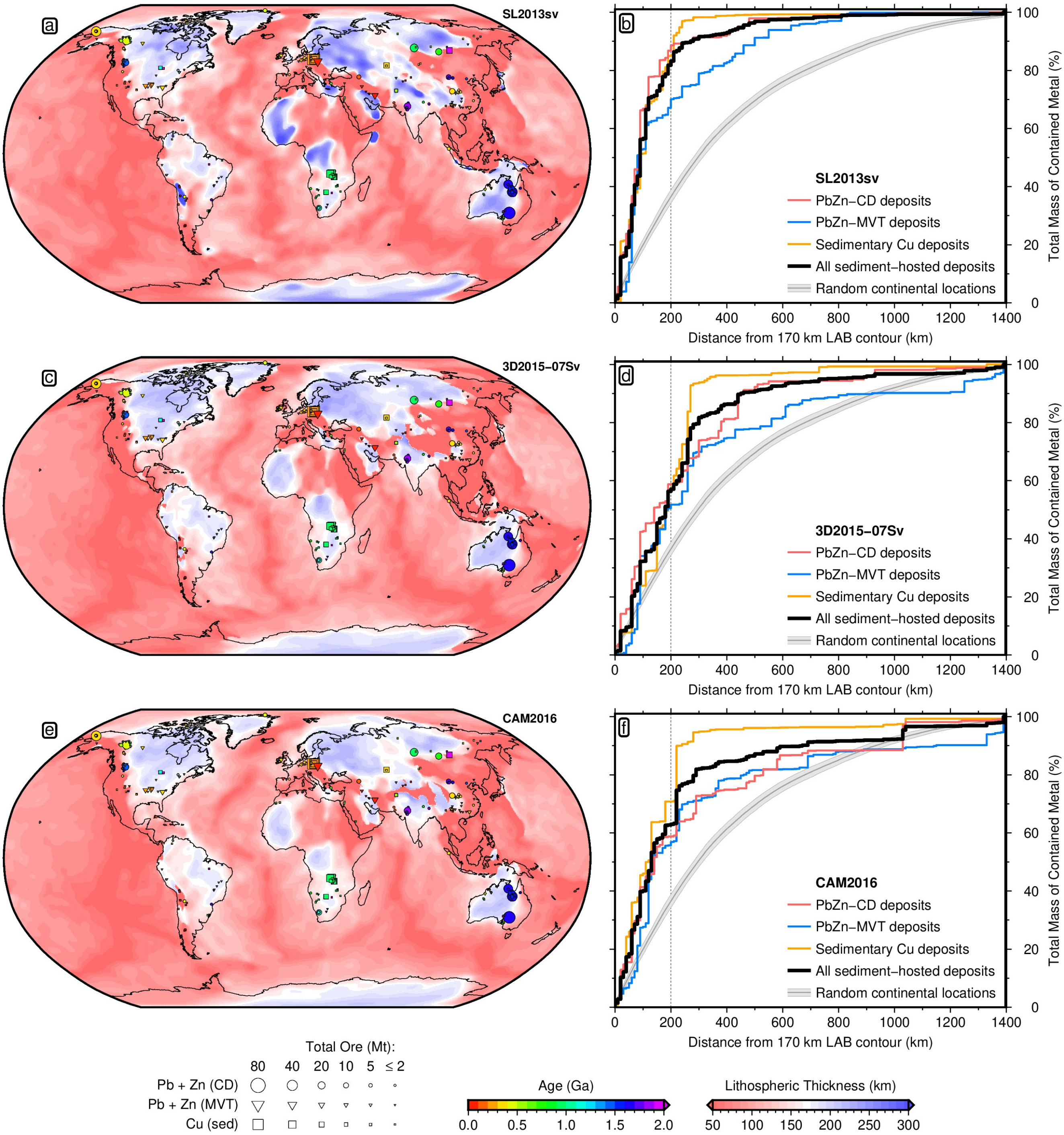

Figure S13: **Lithospheric thickness maps obtained from calibration of other global surface wave tomography models.** (a) SL2013sv LAB with deposits; symbols as in Figure S12. (b) CDFs for sediment-hosted deposits and random continental locations. (c–d) Same for the 3D2015-07Sv model[54]. (e–f) Same for the CAM2016 model[56]. Note that CDFs for all tomography models show a significant difference with the distribution of random continental locations.

Kolmogorov-Smirnov Statistical Tests

In order to test the statistical significance of real deposit locations, test suites of random points on a sphere are generated. Example test suites of 100, 1000 and 10,000 points are shown in Figure S14.

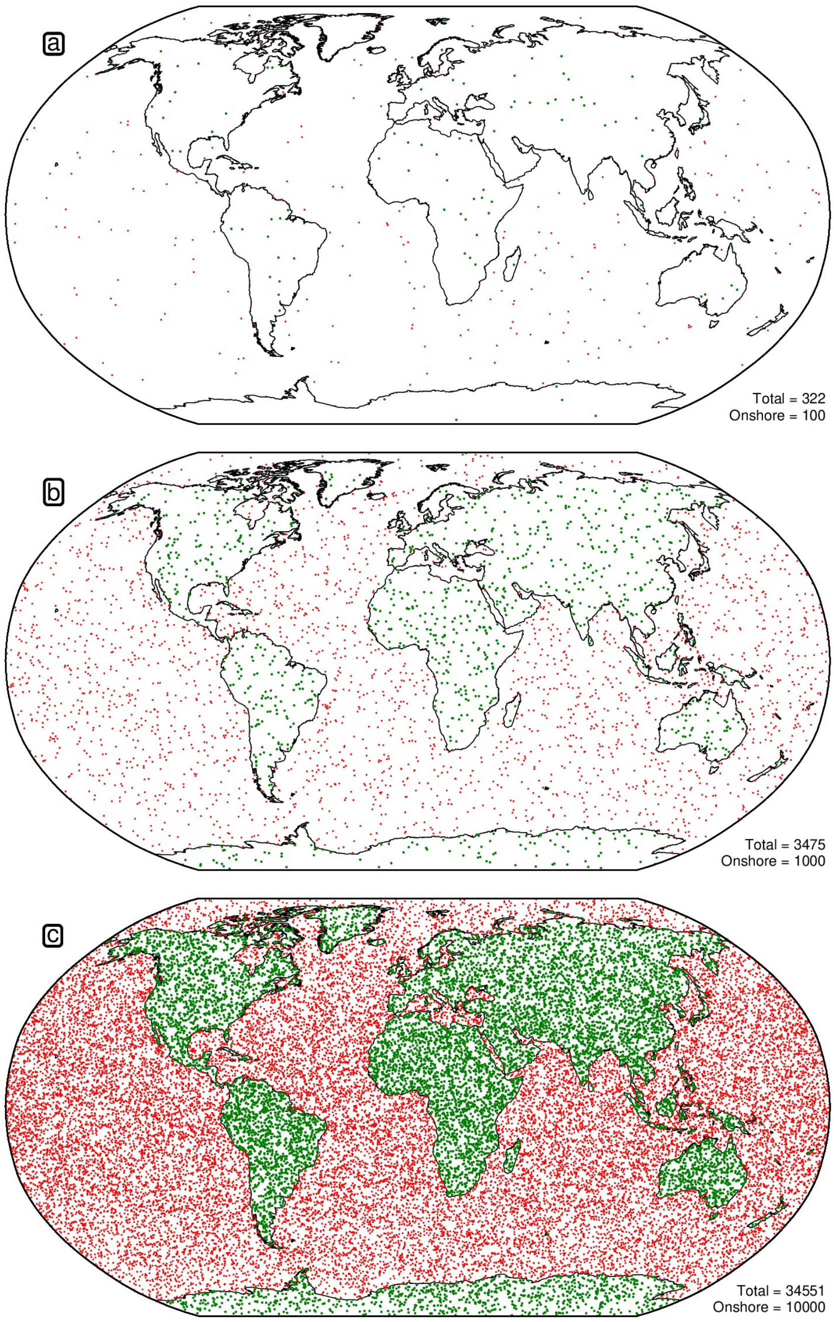

Figure S14: **Distribution of random points on the surface of a sphere.** Green circles = onshore points; red = offshore. (a) Example set of 100 onshore points. (b) Example set of 1000 onshore points. (c) Example set of 10,000 onshore points.

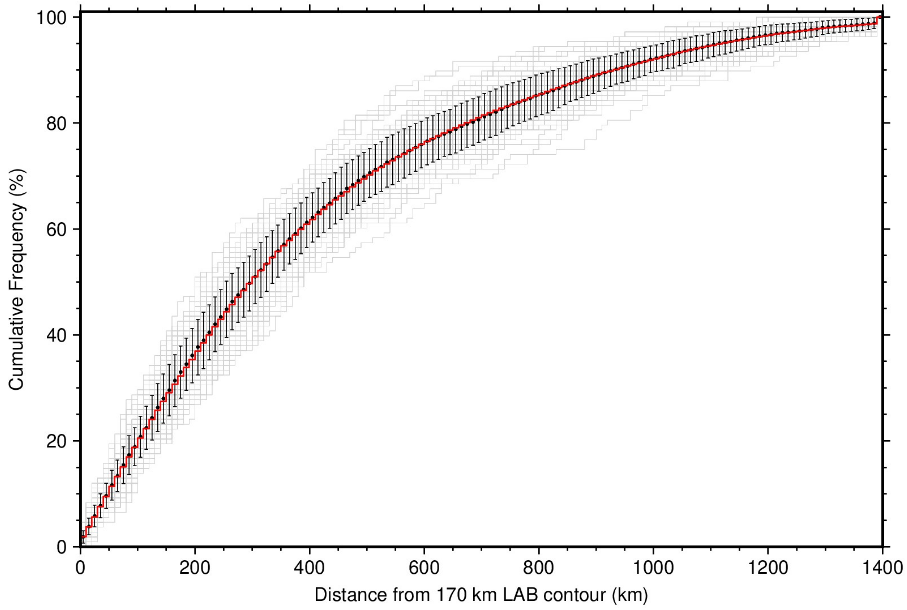

Figure S15: **Cumulative distribution functions for random continental points with distance from the 170 km LAB thickness contour.** Grey lines = 100 CDFs for a set of 109 random points in the continents; black points with error bars = mean and standard deviation of all 100 CDFs within each 10 km bin; red line = CDF for a set of 10,000 random continental points.

For each Kolmogorov-Smirnov test, a number of random points are generated that is equivalent to the number of real deposits of that type (109 for PbZn-CD, 147 for PbZn-MVT and 139 for sedimentary copper). Given the low sample size for some of the deposit classes, the distribution of this random set can vary somewhat from the true average distribution of continental locations. We therefore draw a test set in this manner 100 times (Figure S15). These random CDFs are relatively consistent but have some outliers. The D-value and Kolmogorov-Smirnov statistics between each random CDF and the real one is calculated and reported within a histogram (Figure S16).

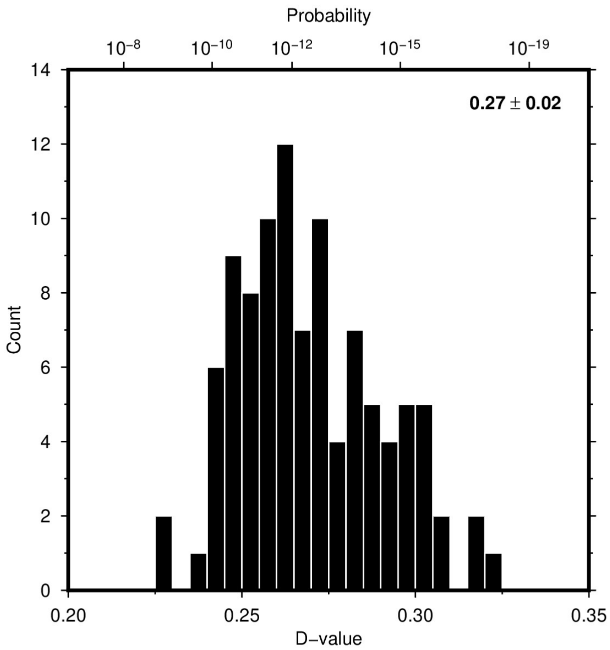

Figure S16: **D-values for all 395 sediment-hosted base metal deposits.** Histogram of D-values for ensemble of 100 random CDFs calculated for each random test set compared with the non-mass-weighted, locally enhanced CDF; inset lists mean and standard deviation of D-values; associated probabilities shown across top.

Testing effect of subducting slabs on deposit statistics

The relationship between seismic wavespeed and temperature results in a tomography model imaging cold subducting slabs in addition to thick, cold cratonic lithosphere as fast velocities at depths > 150 km. Thus it is possible that some of the features imaged in our LAB maps are not related to cratonic lithosphere. Examples include features along the Andean, Caribbean, Aleutian, Japanese, Philippines, Indonesian, and eastern Mediterranean subduction zones (Figure S17).

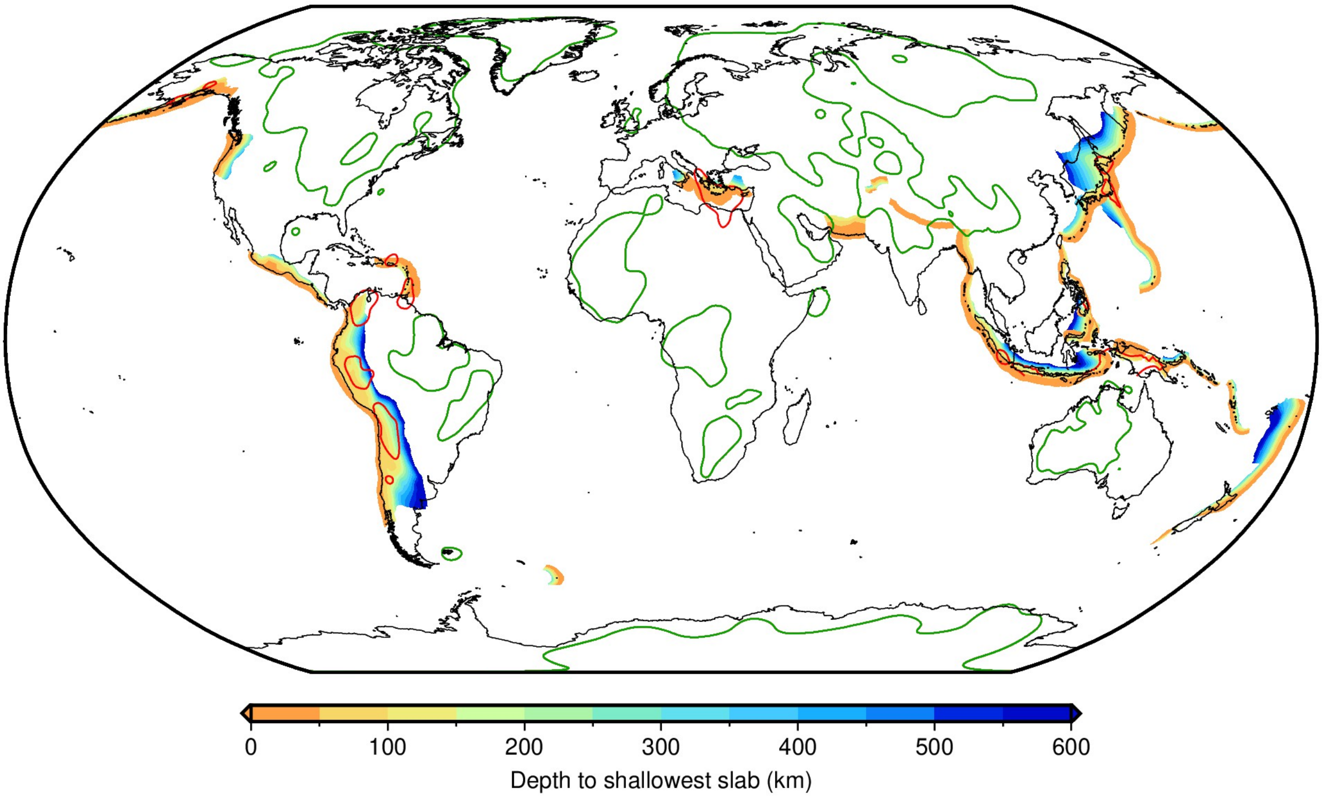

Figure S17: **Subduction zones and areas of thick lithosphere.** Depth of shallowest subducting slabs in the global Slab2[124] model; red lines = 170 km thickness contours in LAB derived from SL2013sv that are potentially related to subducting slabs; green lines = other contours of thick cratonic lithosphere.

None of the giant (> 10 Mt contained metal) sediment-hosted deposits are located at these subduction zones. Nevertheless, some of the smaller deposits can be, such as those in South America, Indonesia and Turkey. We have therefore manually excised 170 km LAB contours that may potentially be related to slabs (red polygons on Figure S17) and repeated the statistical tests.

The CDF for all sediment-hosted base metal deposits is essentially unchanged by this procedure, with $\sim 85\%$ of total metal still found within 200 km of the 170 km contour (Figure S18c). However, the deposit statistics are actually improved, with the D-value increasing from 0.270 ± 0.020 to 0.276 ± 0.022, changing the probability of the relationship occurring by random chance from 1 in 3.35 trillion to 1 in 10.6 trillion. The reason for this is that the reduction in contour extent results in fewer random continental locations falling near the line, with the percentage of total continental area within 200 km of the 170 km LAB thickness contour dropping from 34.3% to 31.0%.

Nevertheless, we have chosen to use the full, non-excised LAB in the paper. Manual identification of potential slabs is a subjective process, with results dependent upon an individual's opinion. Furthermore, it is possible that rifted cratonic fragments may be transported into subduction zone settings,[111] and thus not all of these subduction zone features are necessarily anomalous. We therefore prefer to keep our testing of the veracity of the observed relationship between LAB thickness and ore deposit locations as objective as possible.

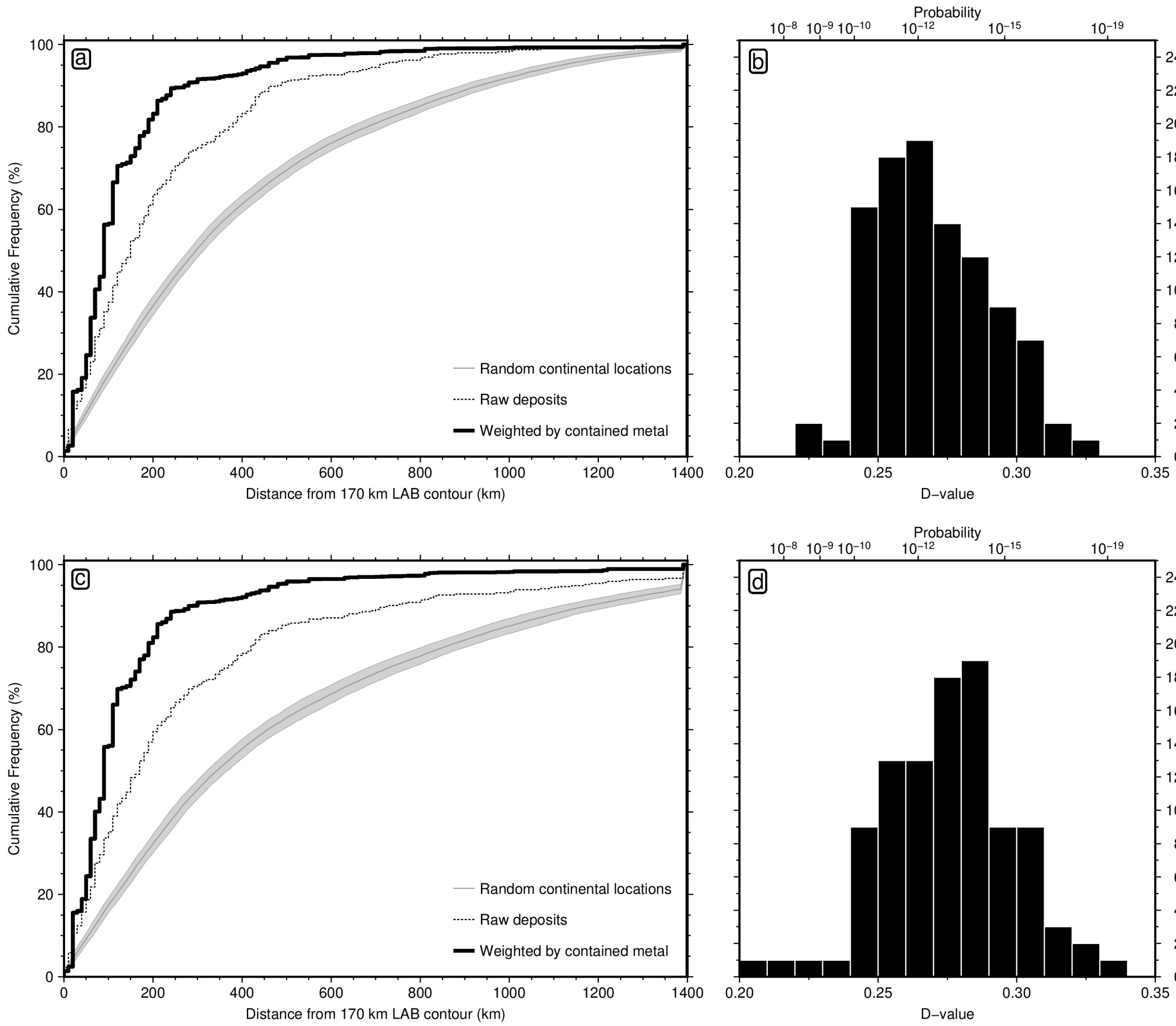

Figure S18: **Effect or removing potentially anomalous features in subduction zone settings on deposit statistics.** (a) Cumulative distribution functions for global sediment-hosted base metals with respect to all 170 km LAB thickness contours (green and red polygons in Figure S17); dotted line = simple count of number of deposits with increasing distance from the 170 km contour; solid black line = deposits weighted by mass of contained metal; grey line/bounds = mean and standard deviation of 100 sets of equivalent number of randomly drawn continental locations. (b) Histogram of D-values for ensemble of 100 random CDFs calculated for a random test set of continental points compared with the non-mass-weighted CDF. (c) and (d) same but using 170 km LAB thickness contours with potentially anomalous subduction zone features removed (only green polygons in Figure S17).

Deposit Compilation

Figures S19–S24 show deposit locations, age distributions with respect to LAB thickness, and Kolmogorov-Smirnov statistical test results for each individual deposit type.

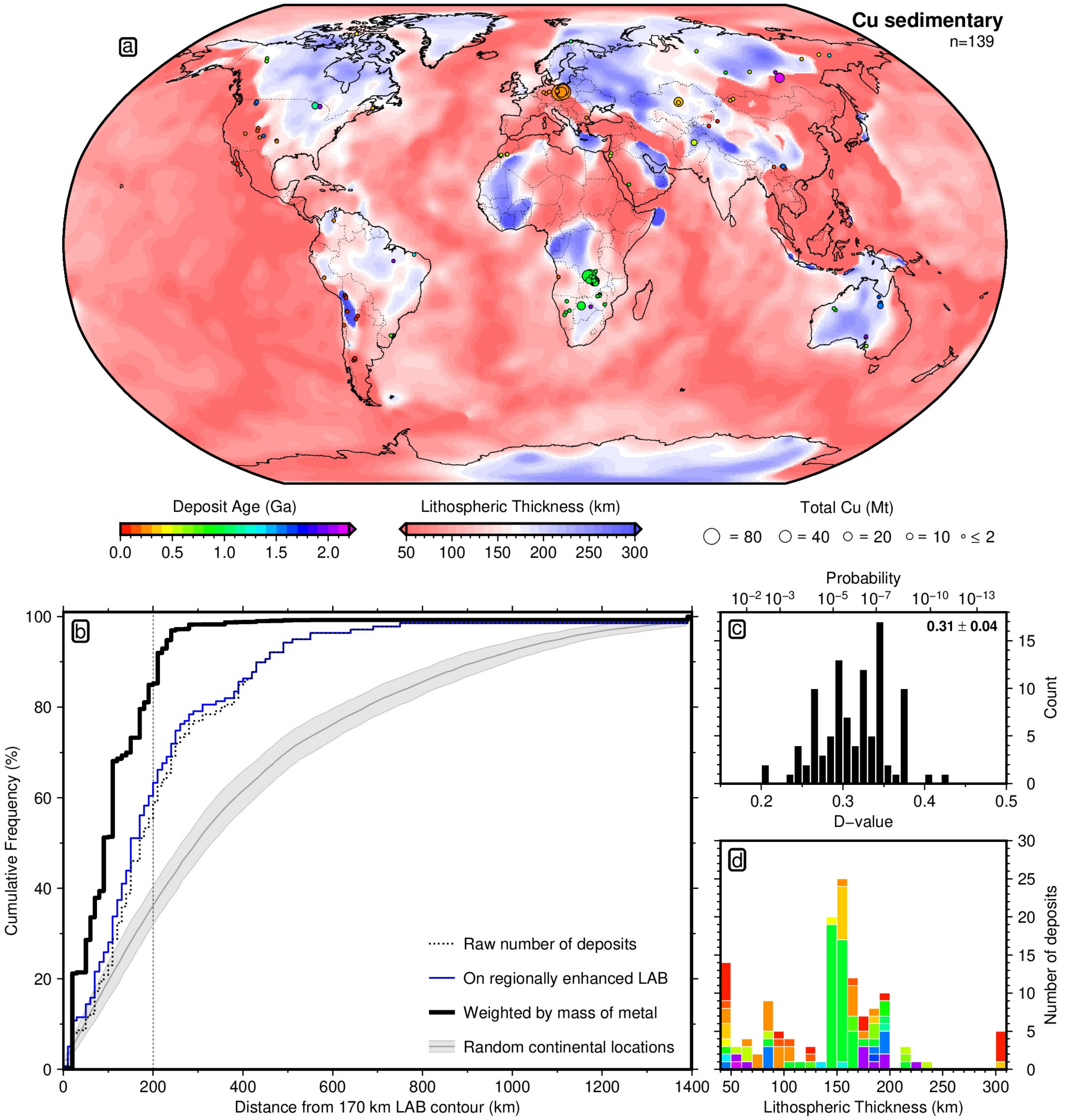

Figure S19: **139 sedimentary copper deposits.** (a) LAB derived from SL2013sv tomography model using a calibrated anelasticity parameterisation.[24,22] Circles = deposit locations; area proportional to estimate of total contained mass of metal (MT = megatonnes); unknown deposit size given 2 Mt symbol; colour = ore body formation age (billion years); unknown age plotted in grey. (b) Different approaches for generating cumulative distribution functions. Dotted line = simple count of number of deposits with increasing distance from the 170 km contour in global LAB map; blue line = simple count where Australian LAB has been replaced with regionally enhanced map (Figure S9a); solid black line = deposits weighted be mass of contained copper on regionally enhanced map; grey line/bounds = mean and standard deviation of 100 sets of equivalent number of randomly drawn continental locations, with respect to regionally enhanced LAB. (c) Histogram of 100 D-values calculated for each random test set and a non-mass-weighted, locally enhanced CDF (blue CDF); inset lists mean and standard deviation of D-values; associated probabilities shown across top. (d) Histogram of deposit occurrence as a function of lithospheric thickness, coloured by deposit age.

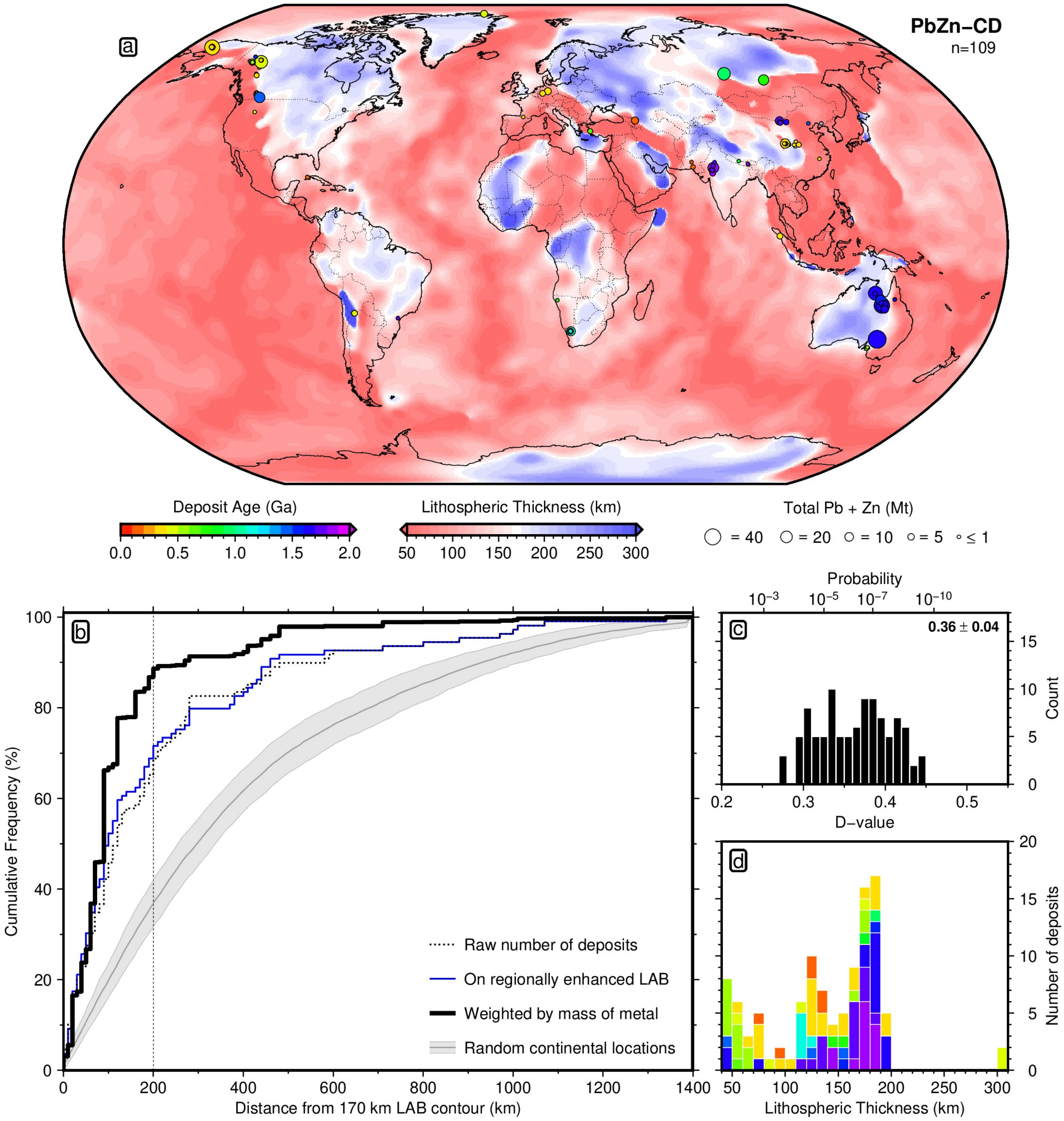

Figure S20: **109 clastic-dominated lead-zinc deposits.** (a) LAB derived from SL2013sv tomography model using a calibrated anelasticity parameterisation.[24,22] Circles = deposit locations; area proportional to estimate of total contained mass of metal (MT = megatonnes); unknown deposit size given 1 Mt symbol; colour = ore body formation age (billion years); unknown age plotted in grey. (b) Different approaches for generating cumulative distribution functions. Dotted line = simple count of number of deposits with increasing distance from the 170 km contour in global LAB map; blue line = simple count where Australian LAB has been replaced with regionally enhanced map (Figure S9a); solid black line = deposits weighted be mass of contained lead and zinc on regionally enhanced map; grey line/bounds = mean and standard deviation of 100 sets of equivalent number of randomly drawn continental locations, with respect to regionally enhanced LAB. (c) Histogram of 100 D-values calculated for each random test set and a non-mass-weighted, locally enhanced CDF (blue CDF); inset lists mean and standard deviation of D-values; associated probabilities shown across top. (d) Histogram of deposit occurrence as a function of lithospheric thickness, coloured by deposit age.

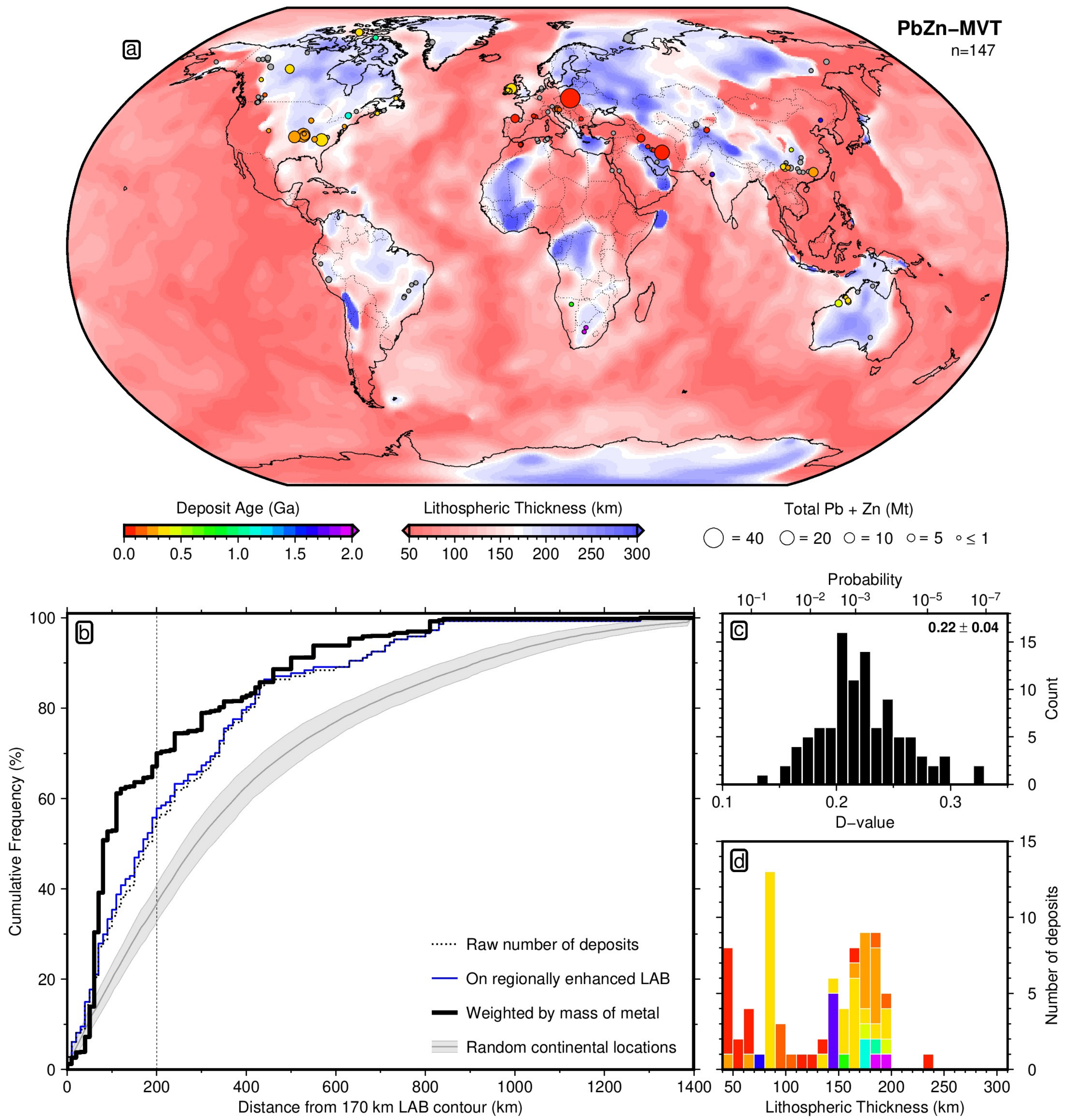

Figure S21: **147 Mississippi Valley-type lead-zinc deposits.** (a) LAB derived from SL2013sv tomography model using a calibrated anelasticity parameterisation.[24,22] Circles = deposit locations; area proportional to estimate of total contained mass of metal (MT = megatonnes); unknown deposit size given 1 Mt symbol; colour = ore body formation age (billion years); unknown age plotted in grey. (b) Different approaches for generating cumulative distribution functions. Dotted line = simple count of number of deposits with increasing distance from the 170 km contour in global LAB map; blue line = simple count where Australian LAB has been replaced with regionally enhanced map (Figure S9a); solid black line = deposits weighted be mass of contained lead and zinc on regionally enhanced map; grey line/bounds = mean and standard deviation of 100 sets of equivalent number of randomly drawn continental locations, with respect to regionally enhanced LAB. (c) Histogram of 100 D-values calculated for each random test set and a non-mass-weighted, locally enhanced CDF (blue CDF); inset lists mean and standard deviation of D-values; associated probabilities shown across top. (d) Histogram of deposit occurrence as a function of lithospheric thickness, coloured by deposit age.

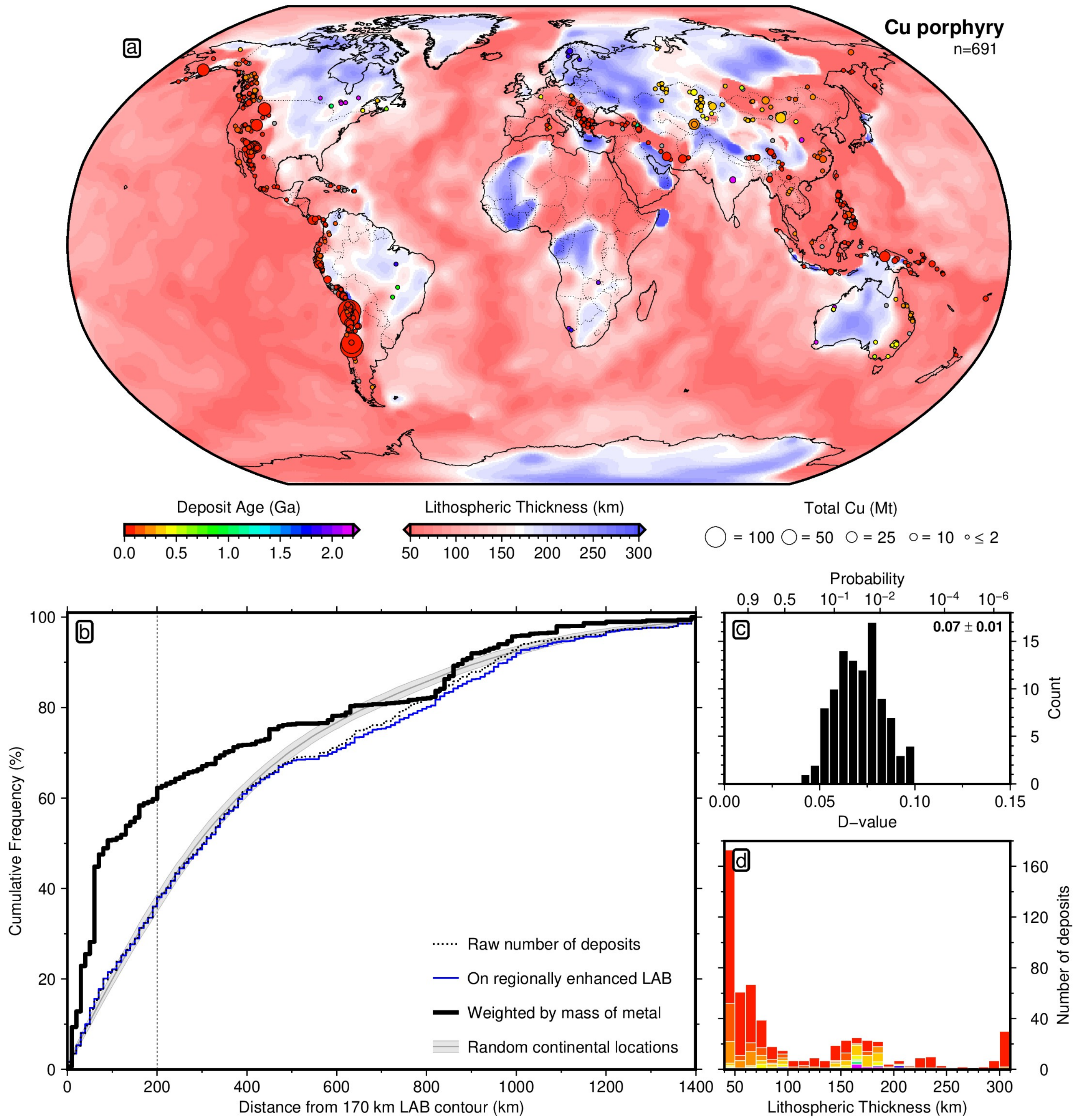

Figure S22: **691 copper porphyry deposits.** (a) LAB derived from SL2013sv tomography model using a calibrated anelasticity parameterisation.[24,22] Circles = deposit locations; area proportional to estimate of total contained mass of metal (MT = megatonnes); unknown deposit size given 2 Mt symbol; colour = ore body formation age (billion years); unknown age plotted in grey. (b) Different approaches for generating cumulative distribution functions. Dotted line = simple count of number of deposits with increasing distance from the 170 km contour in global LAB map; blue line = simple count where Australian LAB has been replaced with regionally enhanced map (Figure S9a); solid black line = deposits weighted be mass of contained copper on regionally enhanced map; grey line/bounds = mean and standard deviation of 100 sets of equivalent number of randomly drawn continental locations, with respect to regionally enhanced LAB. (c) Histogram of 100 D-values calculated for each random test set and a non-mass-weighted, locally enhanced CDF (blue CDF); inset lists mean and standard deviation of D-values; associated probabilities shown across top. (d) Histogram of deposit occurrence as a function of lithospheric thickness, coloured by deposit age.

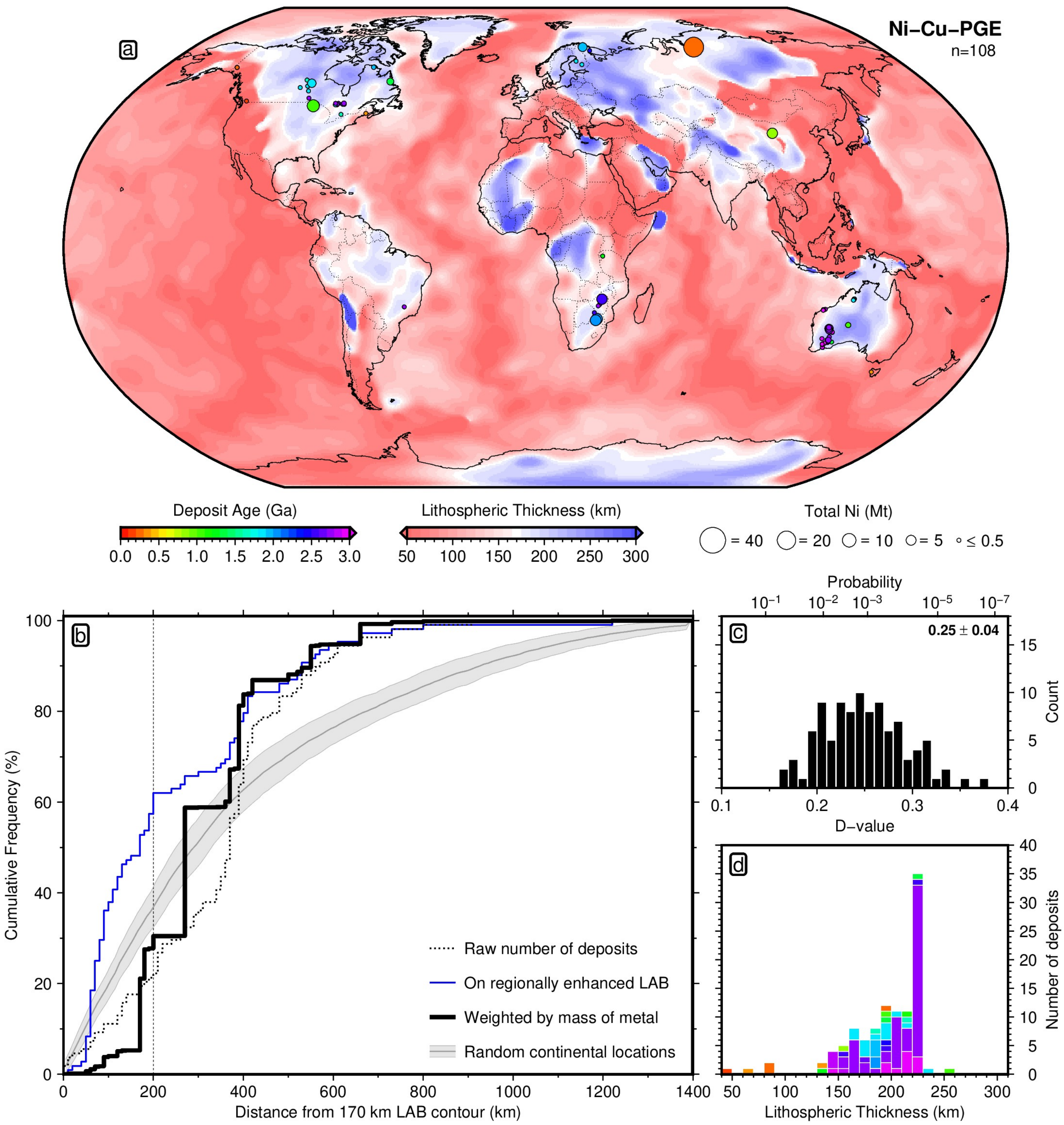

Figure S23: **108 magmatic nickel-copper-platinum group element deposits.** (a) LAB derived from SL2013sv tomography model using a calibrated anelasticity parameterisation.[24,22] Circles = deposit locations; area proportional to estimate of total contained mass of metal (MT = megatonnes); unknown deposit size given 0.5 Mt symbol; colour = ore body formation age (billion years); unknown age plotted in grey. (b) Different approaches for generating cumulative distribution functions. Dotted line = simple count of number of deposits with increasing distance from the 170 km contour in global LAB map; blue line = simple count where Australian LAB has been replaced with regionally enhanced map (Figure S9a); solid black line = deposits weighted be mass of contained nickel on regionally enhanced map; grey line/bounds = mean and standard deviation of 100 sets of equivalent number of randomly drawn continental locations, with respect to regionally enhanced LAB.. (c) Histogram of 100 D-values calculated for each random test set and a non-mass-weighted, locally enhanced CDF (blue CDF); inset lists mean and standard deviation of D-values; associated probabilities shown across top. (d) Histogram of deposit occurrence as a function of lithospheric thickness, coloured by deposit age.

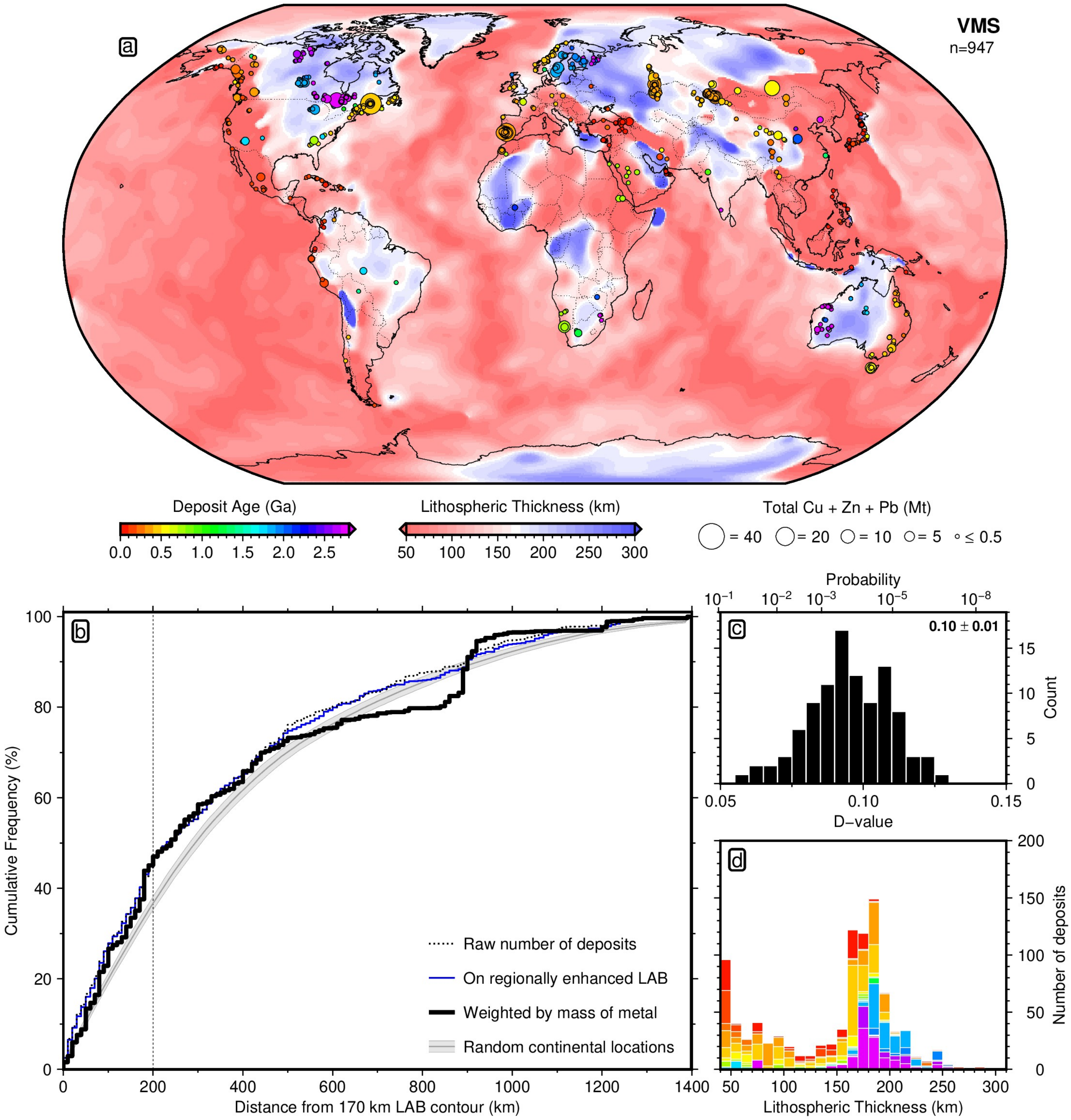

Figure S24: **947 volcanogenic massive sulphide deposits.** (a) LAB derived from SL2013sv tomography model using a calibrated anelasticity parameterisation.[24,22] Circles = deposit locations; area proportional to estimate of total contained mass of metal (MT = megatonnes); unknown deposit size given 0.5 Mt symbol; colour = ore body formation age (billion years); unknown age plotted in grey. (b) Different approaches for generating cumulative distribution functions. Dotted line = simple count of number of deposits with increasing distance from the 170 km contour in global LAB map; blue line = simple count where Australian LAB has been replaced with regionally enhanced map (Figure S9a); solid black line = deposits weighted be mass of contained copper, lead and zinc on regionally enhanced map; grey line/bounds = mean and standard deviation of 100 sets of equivalent number of randomly drawn continental locations, with respect to regionally enhanced LAB. (c) Histogram of 100 D-values calculated for each random test set and a non-mass-weighted, locally enhanced CDF (blue CDF); inset lists mean and standard deviation of D-values; associated probabilities shown across top. (d) Histogram of deposit occurrence as a function of lithospheric thickness, coloured by deposit age.

Regional Deposit Maps

Regional maps of Africa, Europe, Asia, Antarctica, North and South America are provided, showing the global LAB model with known sediment-hosted base metal deposits.

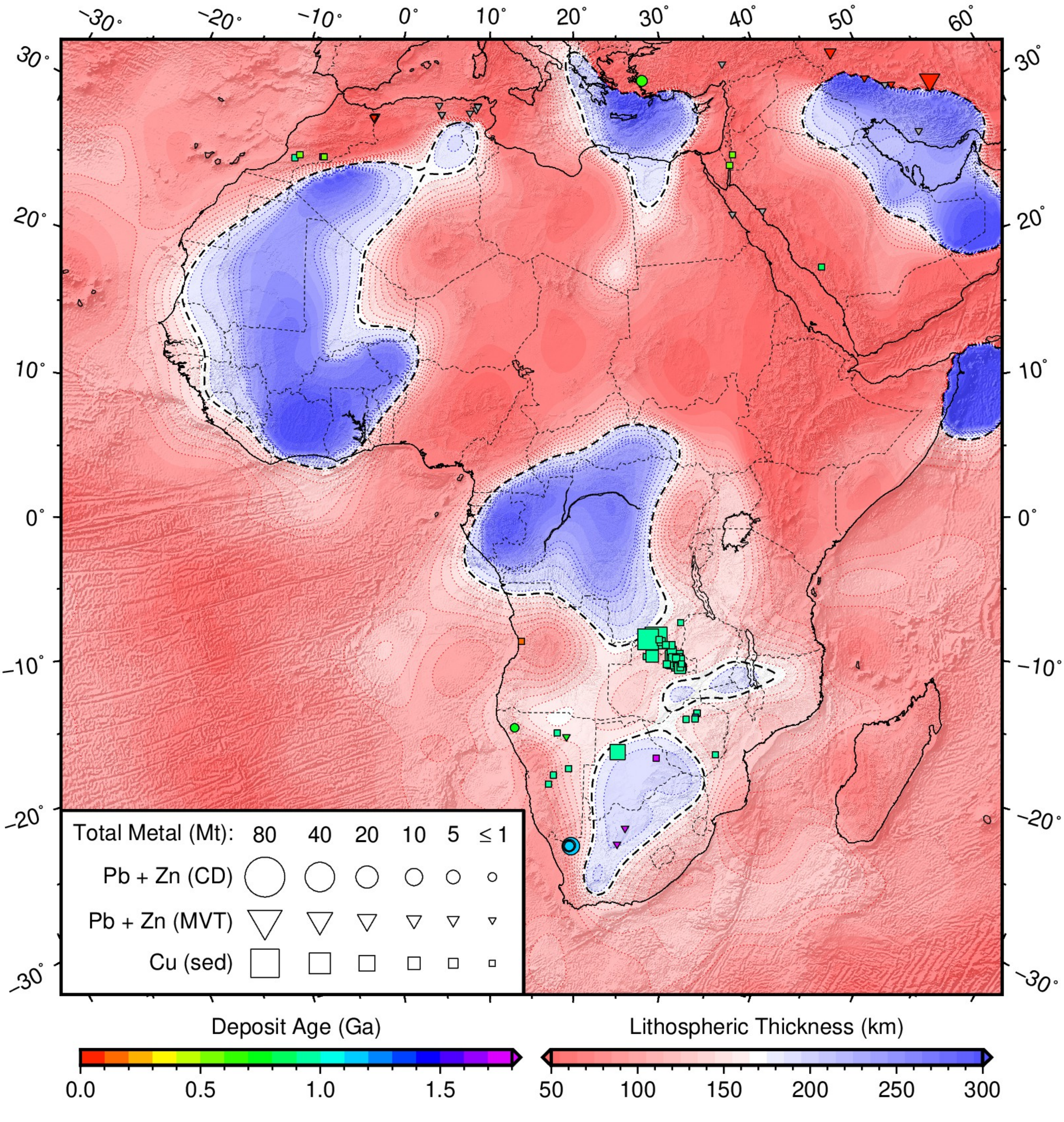

Figure S25: **Distribution of sediment-hosted base metal deposits as a function of lithospheric thickness in Africa.** Global LAB derived from SL2013sv tomography model[24] using a calibrated anelasticity parameterisation[22]; black dashed contour = 170 km LAB thickness; symbols = deposit locations; area proportional to estimate of total contained mass of metal (Mt = megatonnes); unknown deposit size given 1 Mt symbol; colour = ore body formation age (billion years); unknown age plotted in grey; circles = clastic-dominated lead-zinc (PbZn-CD); triangles = Mississippi Valley type lead-zinc (PbZn-MVT); squares = sedimentary copper (Cu-sed).

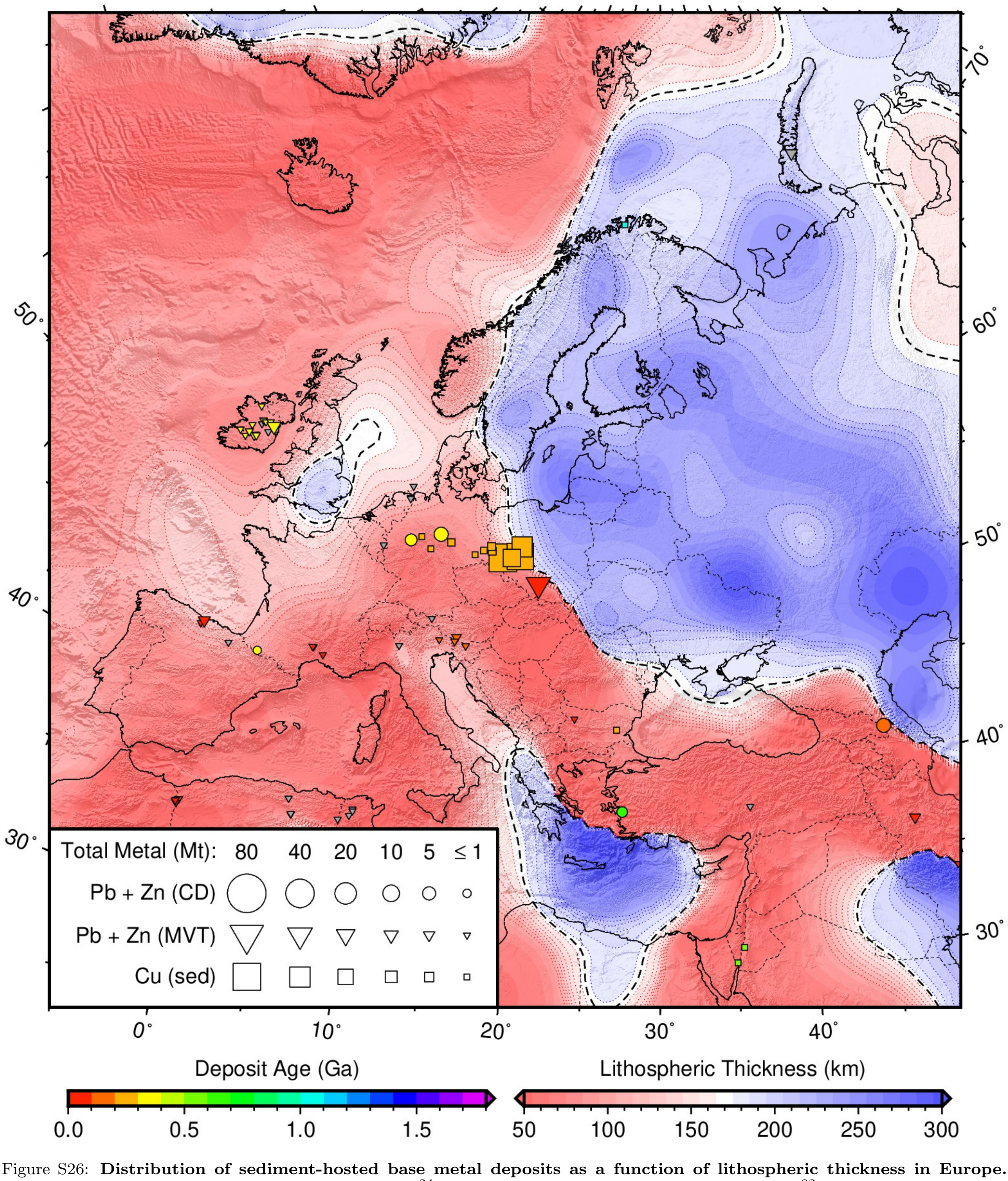

Figure S26: **Distribution of sediment-hosted base metal deposits as a function of lithospheric thickness in Europe.** Global LAB derived from SL2013sv tomography model [24] using a calibrated anelasticity parameterisation [22]; black dashed contour = 170 km LAB thickness; symbols = deposit locations; area proportional to estimate of total contained mass of metal (Mt = megatonnes); unknown deposit size given 1 Mt symbol; colour = ore body formation age (billion years); unknown age plotted in grey; circles = clastic-dominated lead-zinc (PbZn-CD); triangles = Mississippi Valley type lead-zinc (PbZn-MVT); squares = sedimentary copper (Cu-sed).

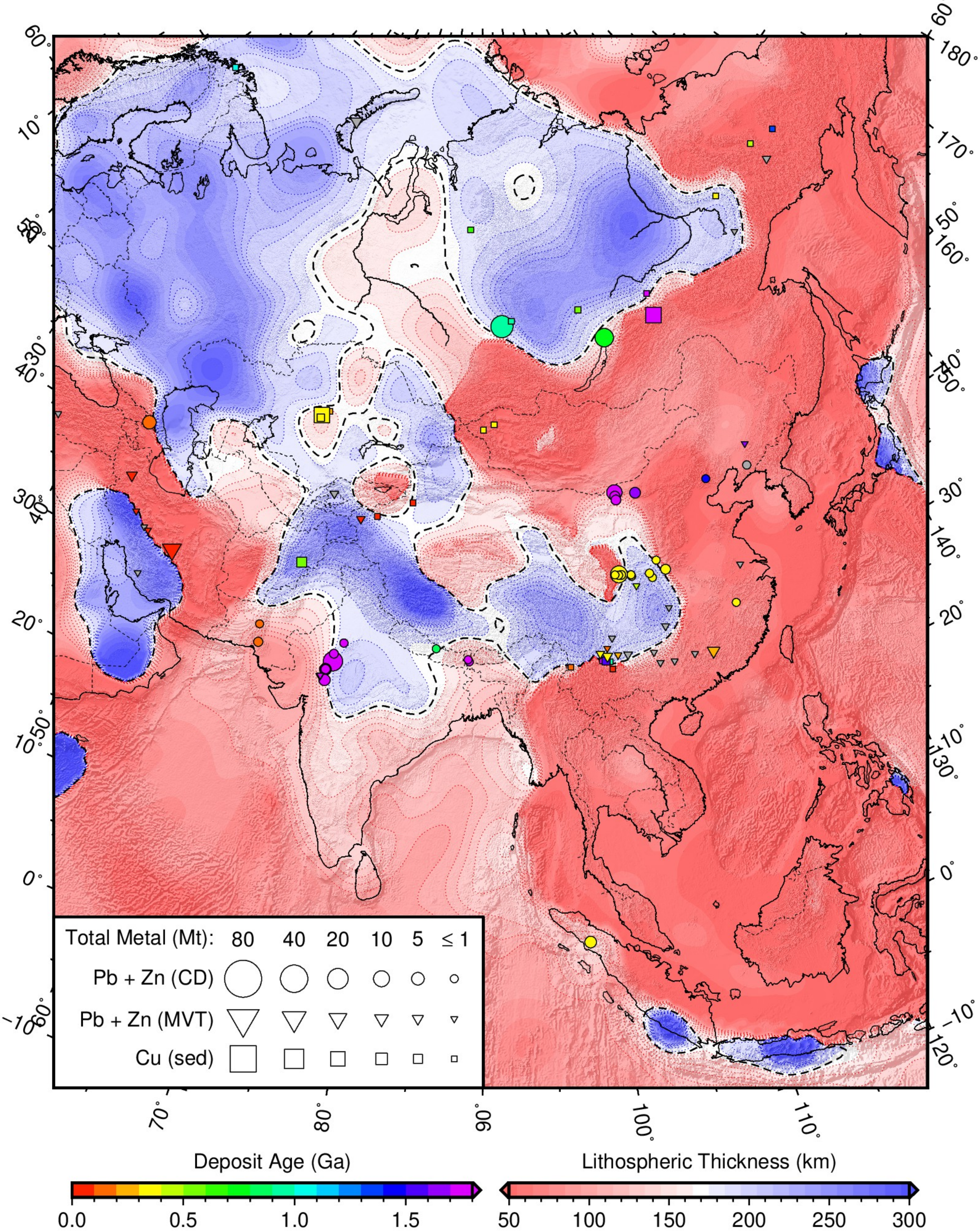

Figure S27: **Distribution of sediment-hosted base metal deposits as a function of lithospheric thickness in Asia.** Global LAB derived from SL2013sv tomography model[24] using a calibrated anelasticity parameterisation[22]; black dashed contour = 170 km LAB thickness; symbols = deposit locations; area proportional to estimate of total contained mass of metal (Mt = megatonnes); unknown deposit size given 1 Mt symbol; colour = ore body formation age (billion years); unknown age plotted in grey; circles = clastic-dominated lead-zinc (PbZn-CD); triangles = Mississippi Valley type lead-zinc (PbZn-MVT); squares = sedimentary copper (Cu-sed).

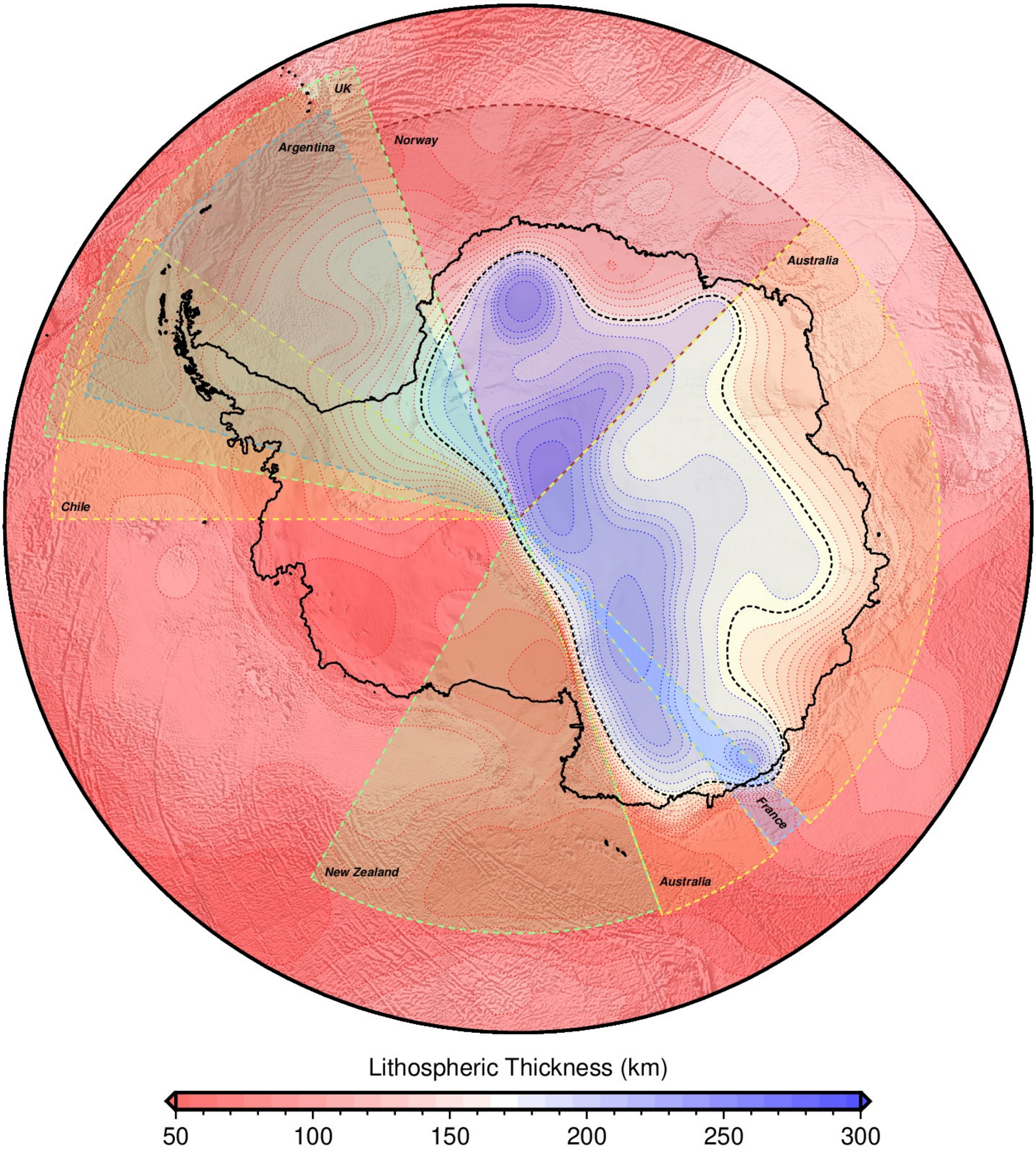

Figure S28: **Lithospheric thickness in Antarctica.** Global LAB derived from SL2013sv tomography model[24] using a calibrated anelasticity parameterisation[22]; black dashed contour = 170 km LAB thickness; coloured segments = approximate extent of principal territorial claims by sovereign states.

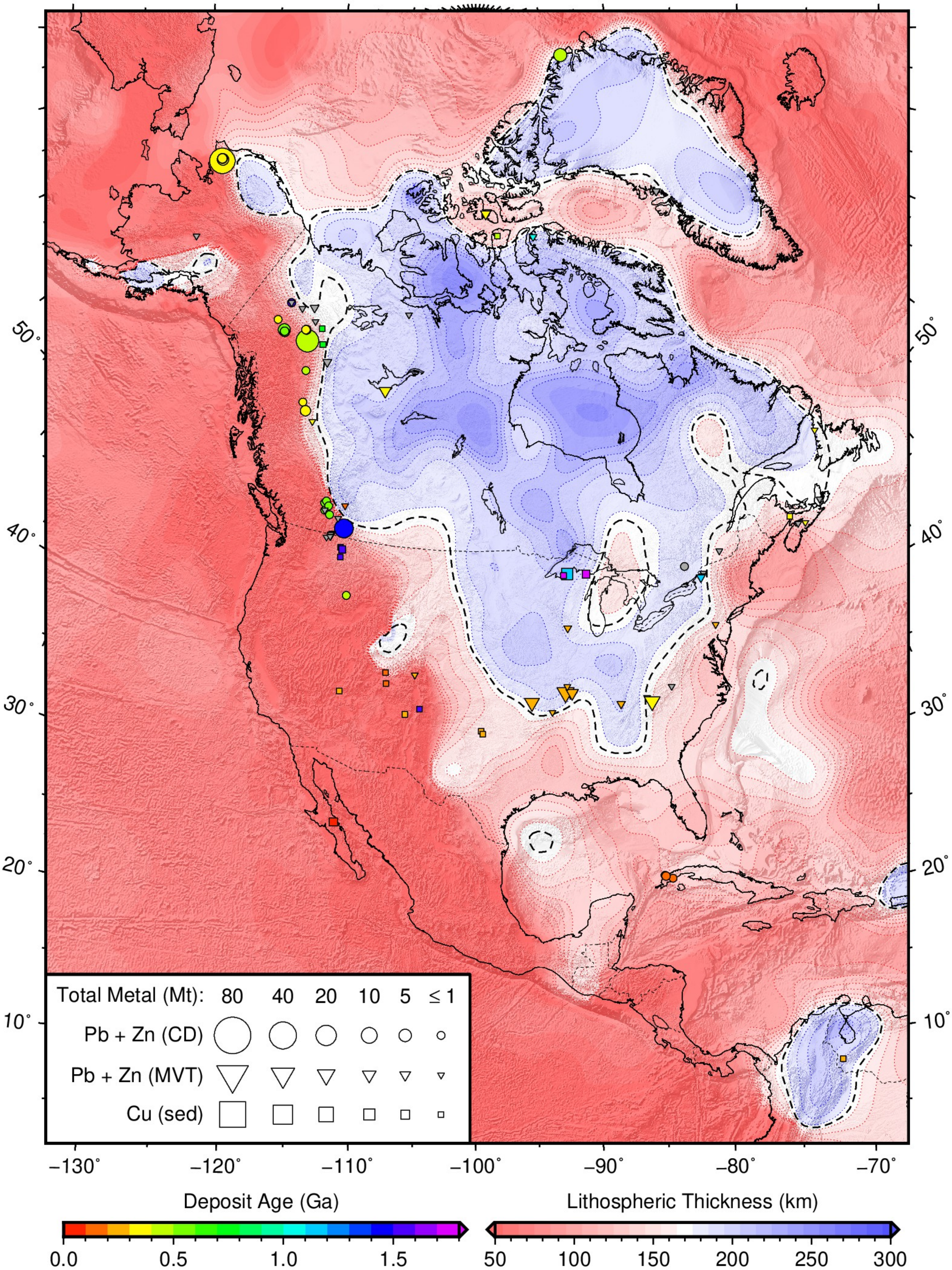

Figure S29: **Distribution of sediment-hosted base metal deposits as a function of lithospheric thickness in North America.** Global LAB derived from SL2013sv tomography model[24] using a calibrated anelasticity parameterisation[22]; black dashed contour = 170 km LAB thickness; symbols = deposit locations; area proportional to estimate of total contained mass of metal (Mt = megatonnes); unknown deposit size given 1 Mt symbol; colour = ore body formation age (billion years); unknown age plotted in grey; circles = clastic-dominated lead-zinc (PbZn-CD); triangles = Mississippi Valley type lead-zinc (PbZn-MVT); squares = sedimentary copper (Cu-sed).

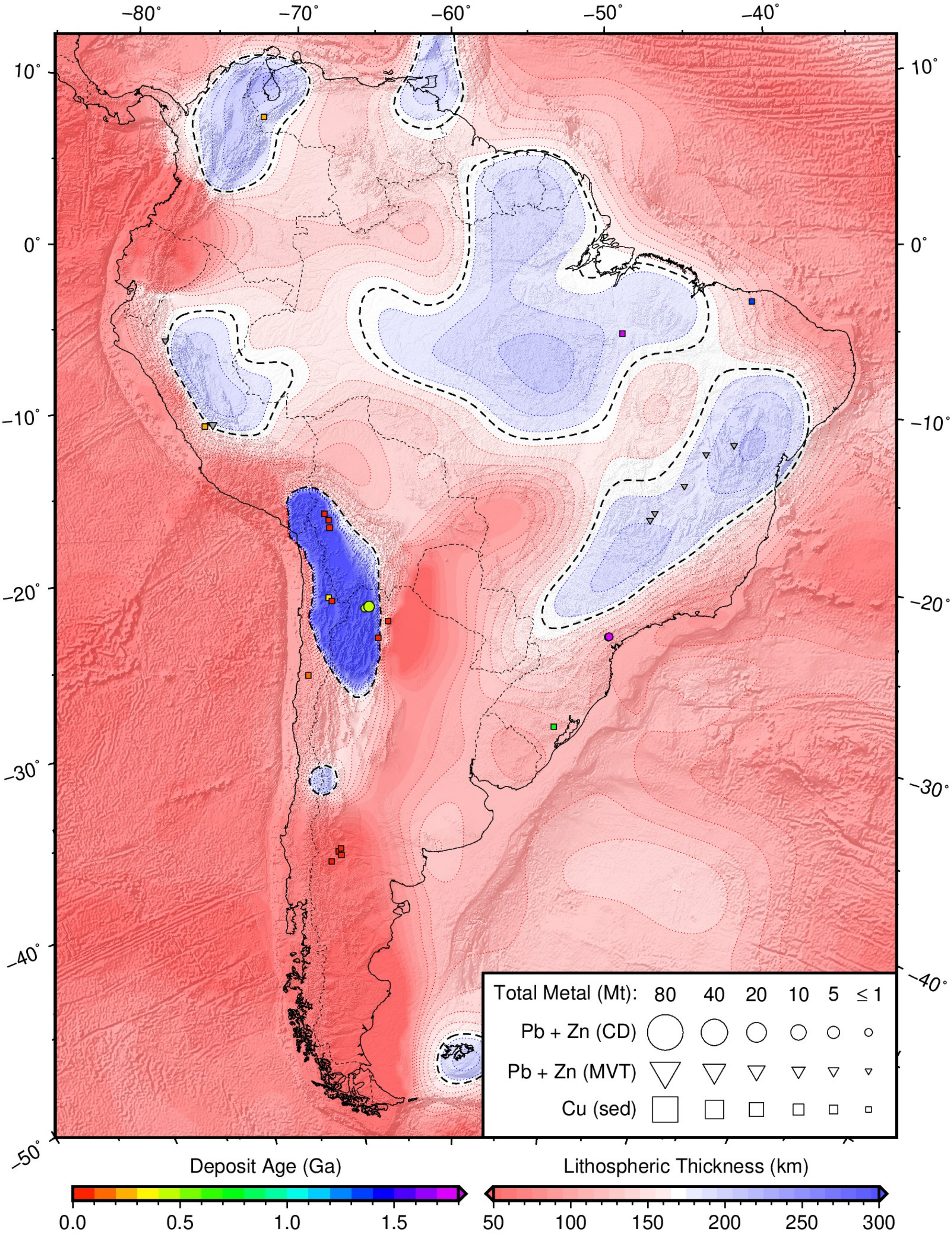

Figure S30: **Distribution of sediment-hosted base metal deposits as a function of lithospheric thickness in South America.** Global LAB derived from SL2013sv tomography model[24] using a calibrated anelasticity parameterisation[22]; black dashed contour = 170 km LAB thickness; symbols = deposit locations; area proportional to estimate of total contained mass of metal (Mt = megatonnes); unknown deposit size given 1 Mt symbol; colour = ore body formation age (billion years); unknown age plotted in grey; circles = clastic-dominated lead-zinc (PbZn-CD); triangles = Mississippi Valley type lead-zinc (PbZn-MVT); squares = sedimentary copper (Cu-sed).

Rift modelling of continental lithosphere

Figures S31–S33 show the results of thermal modelling of rifting continental lithosphere on basin subsidence and temperature of the sedimentary pile.

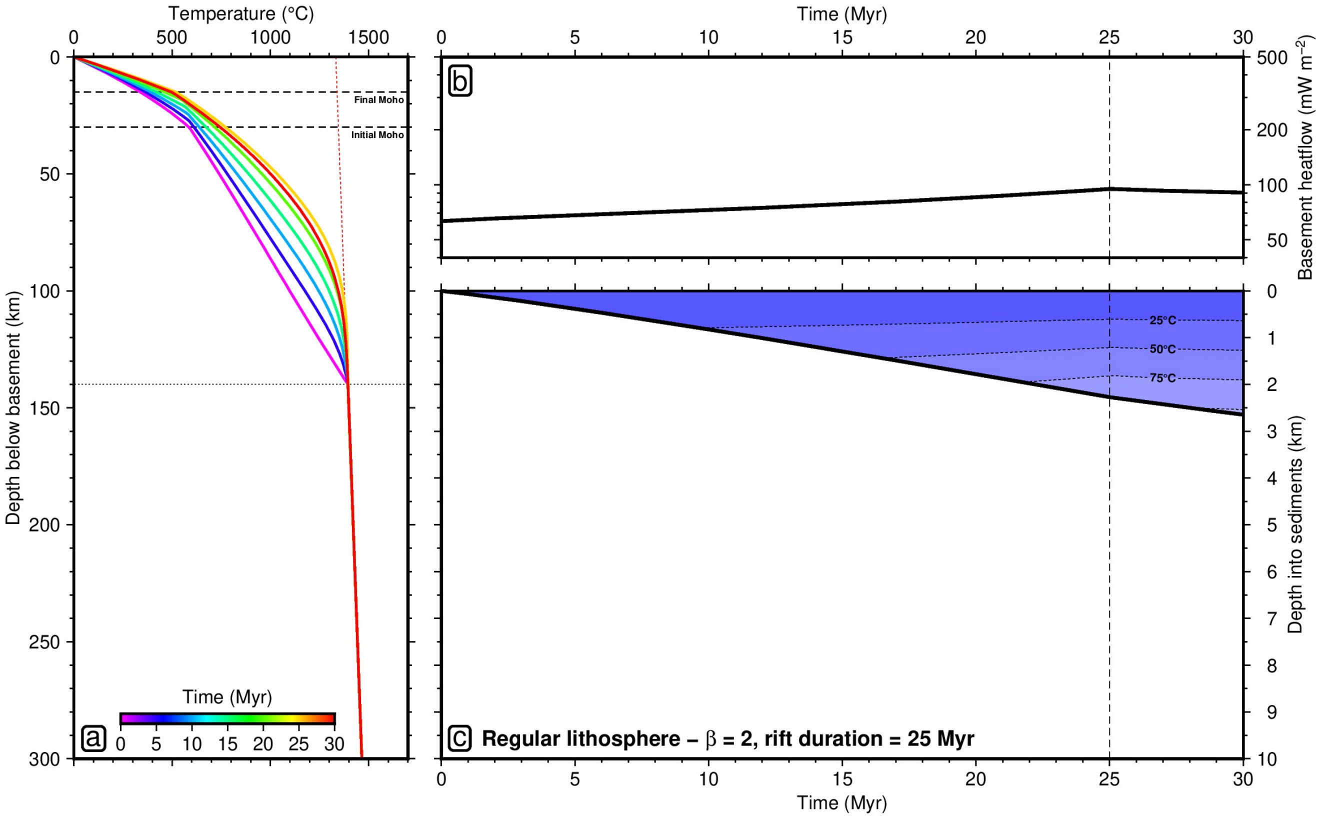

Figure S31: **Regular continental lithosphere with $\beta = 2$ and 25 Myr rift duration.** (a) Thermal evolution of the lithosphere. (b) Heat flow through the top of the crust. (c) Sediment-loaded subsidence of the basin, coloured by temperature structure of the sedimentary pile.

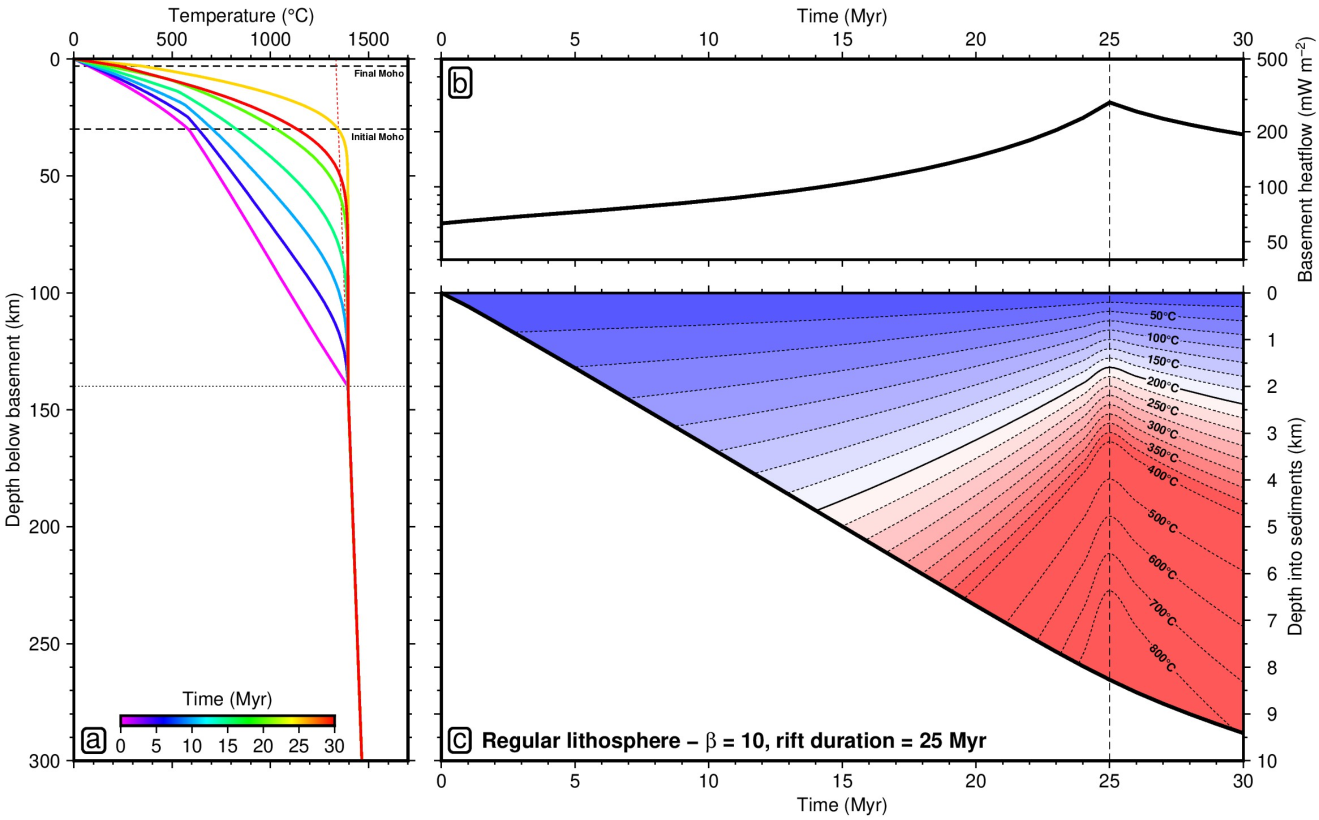

Figure S32: **Regular continental lithosphere with $\beta = 10$ and 25 Myr rift duration.** (a) Thermal evolution of the lithosphere. (b) Heat flow through the top of the crust. (c) Sediment-loaded subsidence of the basin, coloured by temperature structure of the sedimentary pile.

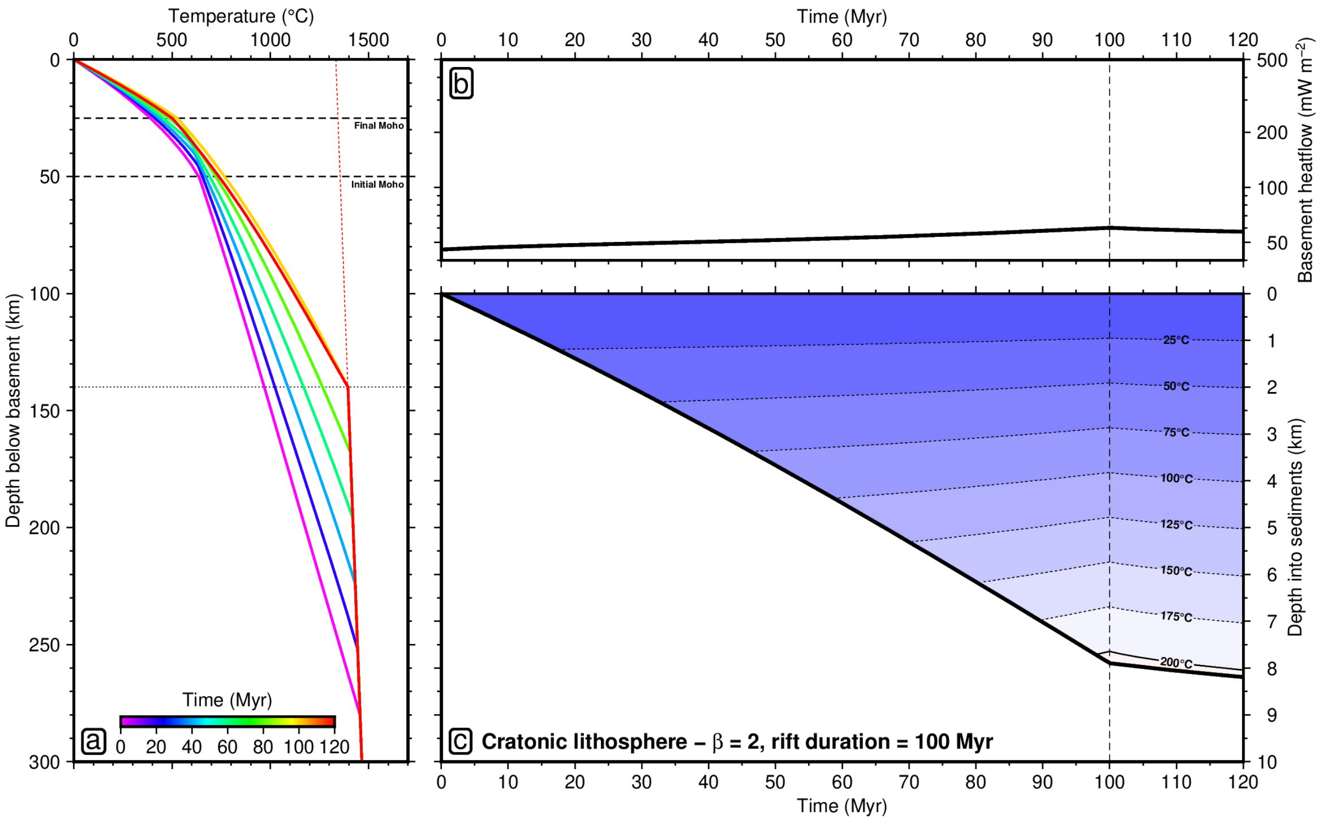

Figure S33: **Cratonic continental lithosphere with $\beta = 2$ and 100 Myr rift duration.** (a) Thermal evolution of the lithosphere. (b) Heat flow through the top of the crust. (c) Sediment-loaded subsidence of the basin, coloured by temperature structure of the sedimentary pile.